Integrated Master in Chemical Engineering

Syngas purification using MIL-125(Ti)_NH_2

Master's Dissertation

by

Maria João Barbosa Regufe

Developed for the Dissertation course unit at:

LSRE - Laboratory of Separation and Reaction Engineering

Supervisor: Doutora Ana Mafalda Ribeiro

Co-Supervisor: Doutor Alexandre Ferreira

Chemical Engineering Departments

July 2014

Acknowledgments

Reservo esta secção para agradecer a todos os que de alguma forma contribuíram para o bom desenvolvimento desta dissertação e que estiveram presentes ao longo deste ciclo académico que agora finda.

Assim, agradeço aos meus orientadores, Ana Mafalda e Alexandre, com quem tanto aprendi ao longo dos últimos meses. Obrigada por toda a dedicação e amizade. Foi ótimo poder aprender com os melhores.

Ao Professor José Miguel Loureiro agradeço todo o conhecimento partilhado, amizade e humanidade que sempre o caracterizam. Ao Professor Alírio Rodrigues pela disponibilização das instalações para realização das experiências. Ao LSRE pela oportunidade de desenvolvimento desta dissertação.

À amiga Yaidelin, agradeço os bons momentos passados no laboratório. A confiança é uma coisa…que eu nem te digo!

Agradeço aos meus papás, a quem dedico todas as minhas conquistas. O vosso suporte e amor são essenciais. A ti, mano, obrigada pela presença constante e pelo exemplo de sucesso que representas. You are the best!

À minha família (avó, padrinhos e prima, pequena M. e primos, papás Rui e Elvira e "vovô") pelo carinho. E ainda, às minhas estrelinhas, presentes diariamente no meu coração.

Como "os amigos são a família que se escolhe", a vocês, Tânia, Catarina, Luísa, Fernando e Paulinho, obrigada pelos bons momentos!

E em destaque, termino por te agradecer a ti, **meu amor**, que me preenches o coração. Pelo apoio e confiança que me transmites todos os dias. És fundamental e insubstituível na minha vida. Obrigada!

“Não sou nada.

Nunca serei nada.

Não posso querer ser nada.

À parte isso, tenho em mim todos os sonhos do mundo.”

Fernando Pessoa

Declaração

Declaro, sob compromisso de honra, que este trabalho é original e que todas as contribuições não originais foram devidamente referenciadas com identificação da fonte.

Porto, 3 de julho de 2014

Maria João Barbosa Regufe

(Maria João Barbosa Regufe)

Abstract

Nowadays, metal-organic frameworks (MOFs) are being intensively studied as promising adsorbents to be used in several adsorptive processes. Properties like large surface areas and large pore volumes are advantageous. The main goal of this work was to test a titanium based MOF, the MIL-125(Ti)_NH_2 to be used in syngas purification. The adsorbent material was supplied by KRICT (Korea Research Institute of Chemical Technology) as granulates. This study focused on syngas purification for two different applications: hydrogen production and composition adjustment (H_2/CO) to feed in Fisher-Tropsch processes.

Firstly, adsorption isotherms of pure gases (CO_2, CO, N_2, CH_4 and H_2) were determined at 303, 323 and 343 K. The Langmuir isotherm was used to fit the experimental results. It was assessed the adsorption capacity and heat adsorption for each gas. The affinity of the gas towards the adsorbent has the following order: CO_2 > CH_4 > CO > N_2 > H_2 from the most adsorbed to the less adsorbed. Additionally, the isosteric heats were calculated by Clausius-Clapeyron equation.

Single, binary and ternary breakthrough curves were performed at 323 K and 4.5 bar with different feed mixtures. These experimental results allowed experimental validation of adsorption equilibrium predicted by the multicomponent extension of the Langmuir isotherm and the validation of the fixed-bed mathematical model.

Two pressure swing adsorption cycles were designed and performed experimentally. In the first cycle, the objective was the hydrogen purification from a 30%/70% CO_2/H_2 mixture. The performance obtained for this cycle was hydrogen purity of 99.8% with recovery of 35.6%. In the second PSA experiment a feed stream with a 30%/22%/48% CO_2/CO/H_2 was treated to obtain a light product with a H_2/CO ratio between 2.2 and 2.4 (obtained 2.37) and a CO_2 content of 1.56% and a CO_2 enriched stream with 83.8% as heavy product.

Keywords: adsorption, syngas, MIL-125(Ti)_NH_2, isotherm, breakthrough curves, pressure swing adsorption.

Resumo

Atualmente, as estruturas organometálicas (MOFs) têm sido estudadas como adsorventes promissores para serem utilizados em diversos processos de adsorção. Algumas características, como a grande área de superfície e o volume de poros, são propriedades que lhes conferem vantagens relativamente a outros materiais. O principal objetivo deste trabalho foi testar um MOF, o MIL-125(Ti)_NH_2 para purificação de gás de síntese. Este adsorvente em forma de grão foi fornecido pelo KRICT (*Korea Research Institute of Chemical Technology*). Este estudo incidiu na purificação do gás de síntese para duas aplicações distintas: produção de hidrogénio e ajuste da composição de H_2/CO para alimentar a processos de *Fisher-Tropsch*.

Primeiramente foram determinadas as isotérmicas de adsorção de gases puros (CO_2, CO, N_2, CH_4 e H_2) a 303, 323 e 343 K. Foi utilizada a isotérmica de *Langmuir* para ajuste dos resultados experimentais. Determinou-se a capacidade e entalpia de adsorção para cada um deles. Estes resultados permitiram determinar a afinidade de cada gás relativamente ao adsorvente, que, por ordem da maior para a menor adsorção obteve-se: CO_2 > CH_4 > CO > N_2 > H_2. De seguida, pôde-se determinar os calores isostéricos pela equação de *Clausius-Clapeyron*.

Foram realizadas experimentalmente curvas de quebra com um composto, binárias e ternárias a 323 K e 4.5 bar com diferentes misturas de alimentação. Os resultados experimentais permitiram validar o equilíbrio experimental previsto pela extensão multicomponente da isotérmica de *Langmuir* e o modelo matemático de leito fixo.

Foram realizados experimentalmente dois ciclos de adsorção com modelação de pressão. No primeiro ciclo, o objetivo fixou-se na purificação de hidrogénio a partir de uma mistura de 30% de CO_2 e 70% de H_2. Para este ciclo obteve-se uma pureza de 99,8% de hidrogénio com uma recuperação de 35,6%. Na segunda experiência, foi alimentada uma corrente constituída por 30% de CO_2, 22% de CO e 48% de H_2 com o intuito de ser tratada para obtenção de um produto leve com uma razão de H_2/CO entre 2,2 e 2,4, aproximadamente, tendo-se obtido um valor igual a 2,37 e um teor de CO_2 de 1,56% e um produto pesado enriquecido em CO_2 com 83,8%.

Palavras-chave: adsorção, gás de síntese, MIL-125(Ti)_NH_2, isotérmica, curvas de quebra, adsorção com modulação de pressão.

Table of Contents

List of Figures

List of Tables

Notation and Glossary

a_i	number of neighboring sites occupied (multisite Langmuir isotherm)	
a_p	particle external specific area	$m^2\ g^{-1}$
A_{bed}	bed area	m^2
A_i	parameter relating the thermal variation of the heterogeneity coefficient	
a_0 to a_4	parameters of the polynomial equation for the calculation of the heat capacities	
A_1 to A_8	empirical constants	
a_{pM}	particle specific area	$m^2\ g^{-1}$
B_i	Biot number	
C_{inlet}	inlet gas phase concentration	$mol\ m^{-3}$
$C_{g,i}$	gas phase concentration of component i	$mol\ m^{-3}$
$C_{g,T}$	total gas phase concentration	$mol\ m^{-3}$
C_p	heat capacity of the mixture at constant pressure	$J\ mol^{-1}\ K^{-1}$
$\widehat{C_p}$	heat capacity at constant pressure (per mass unit)	$J\ kg^{-1}\ K^{-1}$
$C_{p,i}$	heat capacity at constant pressure of component i	$J\ mol^{-1}\ K^{-1}$
$\hat{C}_{p,s}$	solid specific heat (per mass unit)	$J\ kg^{-1}\ K^{-1}$
$\hat{C}_{p,w}$	wall specific heat (per mass unit)	$J\ kg^{-1}\ K^{-1}$
$C_{s,i}$	concentration at the solid interface of component i	$mol\ m^{-3}$
d_p	particle diameter	m
D_{ax}	mass axial dispersion coefficient	$m^2\ s^{-1}$
$D_{i,j}$	binary molecular diffusivity of component i and j	$m^2\ s^{-1}$
$D_{k,i}$	Knudsen diffusivity of component i	$m^2\ s^{-1}$
D_m	molecular diffusivity	$m^2\ s^{-1}$
$D_{m,i}$	molecular diffusivity of component i	$m^2\ s^{-1}$
$D_{p,i}$	pore diffusivity	$m^2\ s^{-1}$
D_w	column diameter	m
e	column wall thickness	m
h_f	heat transfer coefficient between the gas and the particle	$W\ m^{-2}\ K^{-1}$
h_w	heat transfer coefficient between the gas phase and the wall	$W\ m^{-2}\ K^{-1}$
k_g	thermal conductivity of the gas mixture	$W\ m^{-2}\ K^{-1}$
$k_{g,i}$	thermal conductivity of component i	$W\ m^{-2}\ K^{-1}$

k_f	film mass transfer coefficient	m s^{-1}
k_{SM}	geometrical factor	
K	Boltzmann constant	J K^{-1}
K_i	adsorption constant or Langmuir constant	bar^{-1}
K_i^0	adsorption constant at infinite temperature	bar^{-1}
m_S	adsorbent mass	kg
M_i	molecular weight	kg mol^{-1}
M_{ij}	binary molecular weight of component i and j	kg mol^{-1}
M_w	adsorbate molecular weight	kg mol^{-1}
n_i	temperature-dependent constant on the isotherms equations	
Nu	Nusselt number	
P	Pressure	bar
q_i	adsorbed amount of component i	mol kg^{-1}
$\overline{q_i}$	particle averaged adsorbed concentration	mol kg^{-1}
q_i^*	adsorbed concentration in equilibrium of component i	mol kg^{-1}
$q_{m,i}$	maximum adsorption capacity of the adsorbent of component i	mol kg^{-1}
Q_{feed}	feed volumetric flow rate	L min^{-1}
Re	Reynolds number	
R_g	universal gas constant (R = 8.314)	J mol^{-1} K^{-1}
R_P	particle radius	m
t_{blow}	blowdown step time	s
t_{feed}	feed step time	s
t_{press}	pressurization step time	s
t_{rinse}	rinse step time	s
t_{purge}	purge step time	s
T	temperature	K
T_c	critical temperature of component i	K
T_g	temperature of the gas phase	K
T_{inlet}	inlet temperature	K
T_s	temperature of the solid phase	K
T_w	wall temperature	K
T_∞	external temperature	K
Sc	Schmidt number	
Sh	Sherwood number	
u_0	superficial gas velocity	m s^{-1}
U	overall heat transfer coefficient	W m^{-2} K^{-1}

V_C	volume of the permanent magnet, of the sample basket and of the glass wool used to hold the sample	$m^3\ mol^{-1}$
V_S	volume of the solid adsorbent	$m^3\ mol^{-1}$
y_i	molar faction of component i	
y_{inert}	molar fraction of inert	
z	axial position	m

Greek letters

α	adsorption separation factor	
α_w	ratio of the internal surface area to the volume of the column wall	m^{-1}
α_{wl}	ratio of the log mean surface area to the volume of the column wall	m^{-1}
ΔH	heat of adsorption	$kJ\ mol^{-1}$
ΔH_i	isosteric heat of adsorption of component i	$kJ\ mol^{-1}$
Δm	difference in weight between two measurements	kg
ϵ	attractive force constant in Lennard-Jones potential	$kJ\ mol^{-1}$
ε	bed porosity	
ε_i	energy parameter for interaction between molecules	
ε_p	particle porosity	
λ	heat axial dispersion coefficient	$W\ m^{-1}\ K^{-1}$
μ	fluid viscosity	Pa s
μ_i	viscosity of component i	Pa s
ρ	gas density	$kg\ m^{-3}$
ρ_{ap}	apparent density	$kg\ m^{-3}$
ρ_b	bulk density	$kg\ m^{-3}$
ρ_G	density of the gas phase at the measuring conditions (T,P)	$kg\ m^{-3}$
ρ_L	density of the adsorbed liquid phase	$kg\ m^{-3}$
ρ_w	wall density	$kg\ m^{-3}$
σ_i	collision diameter from the Lennard-Jones potential for component i	Å
σ_{ij}	binary constant parameter component i and j	
τ_p	particle tortuosity	
ω	acentric factor	
$\Omega_{\mu,i}$	collision integral	

List of Acronyms

ATR	Autothermal reforming
BPR	Back-pressure regulator
CPO	Catalytic partial oxidation
EDS	Energy Dispersive X-ray
GC	Gas Chromatographer
LDF	Linear driving force model
MFC	Mass Flow Controller
MFM	Mass Flow Meter
MOF	Metal-Organic Framework
PSA	Pressure Swing Adsorption
SEM	Scanning Electron Micrograph
TCD	Thermal Conductivity Detector
TSA	Temperature Swing Adsorption
TT	Thermocouple

1 Introduction

1.1 Motivation and Relevance

One of the main goals of many research groups involves the exploration of effective ways of purifying synthesis gas either for the production of high purity hydrogen or for tuning its composition (H_2+CO). Depending on its origin, syngas can contain various impurities as nitrogen (N_2), methane (CH_4), ethane (C_2H_6), ethylene (C_2H_4), carbon dioxide (CO_2), hydrogen sulfide (H_2S), ammonia (NH_3) and water (H_2O).

Besides being used to obtain high purity H_2, syngas can be converted into high value products such as methanol or synthetic fuel via the Fischer-Tropsch (FT) process. In order to be used in these processes, the syngas composition must be adjusted in terms of ideal H_2/CO ratios. The syngas is therefore treated in order to remove the impurities and/or adjust its composition to the desired values. Adsorptive processes, due to their low energy requirements, are the focus of many research works. Actually, commercial applications for hydrogen purification use PSA with layered beds of activated carbons and 5A zeolite. The hydrogen purity can reach 99.999% at 70-80% recovery (Fuderer and Rudelstorfer, 1976). In the case of composition adjustment, amine absorption is the currently used process but PSA has been looked at as a viable alternative too. One of the main focus of the ongoing research is the screening of new adsorbent materials that can improve the process performance.

In this work, the performance of a MIL-125(Ti)_NH_2 sample supplied by KRICT (Korea Research Institute of Chemical Technology) as granulates was studied for syngas purification. This material belongs to the new class of microporous crystalline materials, metal-organic frameworks (MOFs). The titanium (IV) 1,4-benzenedicarboxylate (or terephthalate) — MIL-125(Ti)_NH_2, with the chemical formula $Ti_8O_8(OH)_4(O_2C\text{-}C_6H_3NH_2\text{-}CO_2)_6$ has a three-dimensional pseudo-cubic structure with highly interconnected porous. Its large surface area and large pore volume represent two main advantages that may favor the adsorption processes.

To test the material, adsorption equilibrium data of pure gases carbon dioxide (CO_2), carbon monoxide (CO), nitrogen (N_2), methane (CH_4) and hydrogen (H_2) was measured. Single, binary and ternary adsorption and desorption breakthrough curves were carried out at 323 K and 4.5 bar. A mathematical model (Da Silva, 1999) was used to predict the breakthrough curves and to design two PSA tests, one for the purification of H_2 from a binary (CO_2/H_2) mixture; and one to adjust the syngas composition from a CO_2/CO/H_2 feed mixture.

1.2 Outline

This work is constituted by five main parts.

The description and the relevance of the work were presented in Chapter 1.

In Chapter 2, State of the art, presents a brief description about syngas, metal-organic frameworks and pressure swing adsorption processes. The principal methods for obtaining syngas and its main applications are presented. Regarding adsorbent materials, a short history about the main adsorbents is given with emphasis to the appearance of MOFs and its importance. A short description about pressure swing adsorption processes is also made and a review of some patents that exist on this process for gas separation and hydrogen purification is presented.

Chapter 3 deals with the topic of materials and methods. The characteristics of the studied MOF are presented. The experimental set-ups and methods used to determine the adsorption isotherms and to perform the fixed bed and PSA experiments are described. In this chapter the used mathematical model is also described.

Chapter 4 consists in experimental and simulation results. Firstly, adsorption equilibrium is presented together with the regression of the experimental data against the chosen thermodynamic model. After that, single, binary and ternary breakthrough curves results are showed and compared with the simulation results. At the end of the chapter, two PSA case studies are presented. Two cycles were designed, one for hydrogen purification and one for syngas composition adjustment to be fed to a Fischer-Tropsch reactor (H_2/CO ratio between 2.2 and 2.4) and simultaneous CO_2 capture (purity > 95%). These cycles were tested experimentally and compared with the simulations.

To finish, Chapter 5 presents the conclusions of this work and the suggestions for future work.

2 State of the art

2.1 Synthesis gas

Synthesis gas or syngas is used as raw material for various industrial processes. It is a key intermediate to produce a vast quantity of compounds in the chemical industry. The composition of syngas is mainly hydrogen, carbon monoxide and carbon dioxide. It may also contain small amounts of nitrogen and methane (Rostrup-Nielsen and Christiansen, 2011).

It is possible to produce syngas from different raw materials composed of carbon (natural gas, naphtha, biomass, coal, alcohols or oxygenates, liquid residues) and by diverse processes. The principal methods are (Rostrup-Nielsen and Christiansen, 2011):

- **Steam reforming of hydrocarbons (oxygenolysis):** consists in the reactions between steam (or carbon dioxide) and hydrocarbons to form a mixture of hydrogen, carbon monoxide, carbon dioxide and unconverted reactants. These reactions involve the breaking of C-H and C-C bounds by means of oxygen containing species. It can also be between steam and alcohols, such as methanol or ethanol. This method results in a H_2/CO ratio close to 3. When carbon dioxide is used as reactant a H_2/CO ratio close to 1 is obtained.
- **Gasification:** in coal or biomass gasification a reaction occurs with addition of steam and the H_2/CO ratio in syngas relates to the H/C ratio in the feed and to the presence of steam or not. For example, the H/C ratios, when methane and biomass are used as fuels, are 4 and 1.3, respectively.
- **Other manufacture routes:** these are alternative approaches to steam reforming and consist into the addition of oxygen to the feed which can be carried out in three different ways: non-catalytic partial oxidation (POX), used to complete the methane conversion and to reduce soot formation; autothermal reforming (ATR), that is a hybrid partial oxidation that allows a decrease in the temperature and oxygen consumption; catalytic partial oxidation (CPO), in which partial oxidation in a catalytic reactor without a burner occurs; in these processes H_2/CO ratio of approximately 2 is obtained.

Syngas can be used to obtain a wide range of products. Figure 1 shows a list of the main ones.

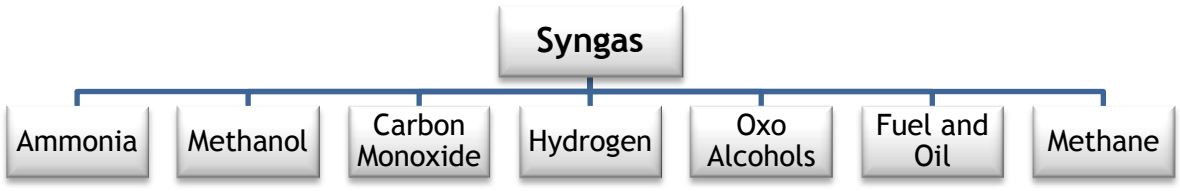

Figure 1 - Applications for synthesis gas (adapted from Higman and Burgt (2003)).

In order to use syngas in the different applications it is necessary to pretreat the syngas. During the production of syngas, most of the catalysts are sensitive to sulphur poisoning. Therefore, there is a need to purify the feedstock for the reforming processes and to purify the raw gas from gasification. When seeking to apply the syngas for ammonia production or hydrogen plants it is necessary to increase the H_2 yield. For this a water-gas-shift (WGS) reaction is used ($CO + H_2O \leftrightarrow H_2 + CO_2$). Furthermore syngas composition can be adjusted, depending on the intended application, by removal of acid gases as carbon dioxide or hydrogen sulphide. This removal is usually done by physical or chemical absorption (Rostrup-Nielsen and Christiansen, 2011).

2.2 Metal-Organic Frameworks (MOFs)

The past decades has been marked by the emergence of new materials. The molecular sieves emerged in 1932 by McBain as materials that exhibit selective adsorption properties. These materials can separate components of a mixture on the basis of molecular size and shape (Szostac, 1998). McBain defined two classes of molecular sieves: the natural zeolites and certain microporous charcoals. Afterwards, this list included more materials like synthetic zeolites, silicas, metal silicates, metal aluminates, aluminophosphates ($AlPO_4$s), and silico/ metal aluminophosphates (SAPOs) (Szostac, 1998).

Additionally, various “cornerstone” materials have been recently reported like: carbon nanotubes, ordered mesoporous silica materials, mesoporous carbons CMK, and metal organic-frameworks (MOFs) (Farrusseng, 2011). However, some of this materials are mesoporous and do not present the molecular sieving property anymore. Figure 2 shows the Euler diagram that represents the family of Metal-Organic Materials (MOMs).

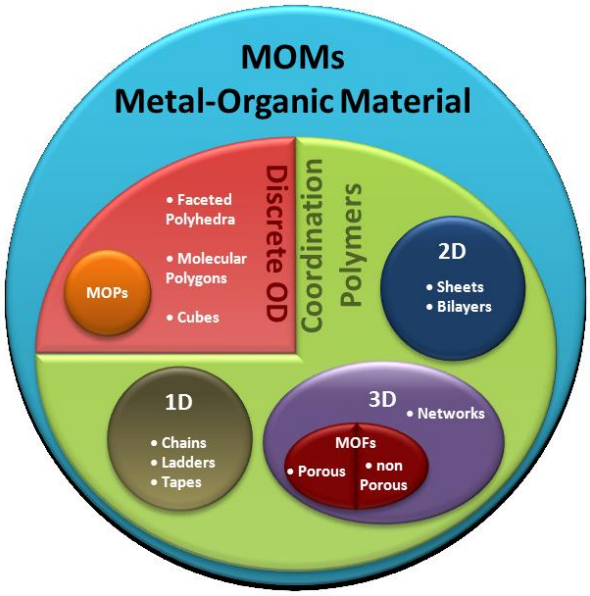

Figure 2 - Euler Diagram of the Metal-Organic Materials family.

In the 1990s, the porous coordination polymers (PCPs) emerged as a new family. A sub-family of these materials, the metal-organic frameworks (MOFs) were described for the first time in 2002 (Farrusseng, 2011). After that, various studies about their crystalline structure and porosity allowed a great development of this class of materials. In general, MOFs fill a gap between pure inorganic and organic materials.

MOFs are hybrid solids that are composed by organic and inorganic moieties linked by strong coordination bonds. These moieties can be extended infinitely in one, two or three dimensions (Férey, 2008). As a result one can obtain in some cases porous materials with regular pores ranging from micro- to mesopores with a large pore surface area. Additionally, highly designable framework, pore shape and size, and surface functionality are key features of these materials. Some MOFs can be flexible; therefore they are good materials for molecular recognition, allowing high chemo, region and enantioselectivity. Furthermore, they cover the space between organic polymers, purely inorganic ceramics and metallic materials regarding hardness and elasticity properties (Farrusseng, 2011).

MOFs present some advantages when compared to other adsorbents. The zeolite-related inorganic solids require the use of inorganic/organic templates beside the components of the skeleton and the solvent. In MOFs' synthesis a solvent that also works as the main template is used. The solvents have weaker interactions with the structure, which causes the structure to remain intact, allowing faster access to the porosity. In these adsorbents a great variety of cations can participate in the framework and a large choice of functionalized organic linkers can be associated with the inorganic parts. Therefore, these specifications provide a huge number of possibilities for creating MOFs (Férey, 2008).

The most studied gas phase separations with MOFs are light gases (e.g. H_2, N_2, O_2, CO_2 and CH_4), light olefins and paraffins (e.g. ethane/ethylene and propane/propylene), harmful gases (e.g. H_2S, SO_2 and CO), nobel gases (e.g. Ar, He and Xe) and vapors (e.g. solvents, xylene isomers and hexane isomers) (Li *et al.*, 2011). There are various extensive reviews in this topic, such as the ones by Long *et al*. (2012), Férey (2008), Kitagawa *et al*. (2004) and Rowsell *et al*. (2004). Regarding the synthesis of MOFs, more detail information can be found in useful reviews by Férey *et al*. (2008), Lee *et al*. (2013) and Norbet and Shyam (2012).

2.3 Pressure Swing Adsorption (PSA)

Pressure swing adsorption emerged as a technology with a single bed cycle with a pressurization step and a sequence of depressurization steps in the first patent published in 1932 by Finlayson and Sharp (Finlayson and Sharp, 1932). Later, PSA process became a key unit operation for gas separation/purification in the 1960s with the patents of Skarstrom (US Patent 2,944,627 (1960)), and Montgareuil (FR Patent 1,223,261 (1964a) and US Patent

3,155,468 (1964b)). Indeed, Skarstrom's patent introduced PSA technology as a commercial process for air separation.

PSA is a cyclic process which is constituted by two or more columns packed with appropriate adsorbent. The feed of the process consists of a target gas mixture. The contact between the solid and the gas allows the selective adsorption of one or more components of the feed mixture on the adsorbent while the less adsorbed component/s is/are being produced at higher purity on the other end of the column. This selective adsorption depends on the difference of adsorption equilibrium (equilibrium selectivity), differences in adsorption rates (kinetic selectivity) and/or steric effects of the different adsorbate molecules of the mixture (Ruthven, 1984).

While some columns adsorb the gas, others are under regeneration (species are partially removed from the adsorbent). This cleaning can be done by reducing the total pressure of system (PSA) or by increasing the temperature (TSA). Therefore, in PSA the regeneration occurs in two steps: adsorption and desorption step, carried out at the higher and lower pressure, respectively.

Today, there are many processes that employ PSA for gas purification, for example in production of hydrogen and simultaneous capture of carbon dioxide by Monereau and Carriere (US Patent 13/130,541 (2011)), in methane purification by Maurer (US Patent 462,514 (1991)), and in syngas purification (H_2/CO or H_2/N_2) with PSA or TSA method by Bacon and Bec (US Patent 7,309,378 (2007)). The properties of the mixture and of the adsorbent determine the design of the PSA for each separation.

3 Material and Methods

3.1 Materials used

3.1.1 Adsorbent

The adsorbent studied was MIL-125(Ti)_NH_2 in the form of granulates provided by KRICT - Korea Research Institute of Chemical Technology (Figure 3). The name defined for material is an acronym of the laboratory in which the material was prepared for the first time, thus MIL stands for *Matériauxs de l'Institut Lavoisier*. MIL-125(Ti)_NH_2 is a titanium(IV) 1,4-benzenedicarboxylate (or terephthalate), with the chemical formula $Ti_8O_8(OH)_4$-$(O_2C$-$C_6H_3NH_2$-$CO_2)_6$ and has a three-dimensional pseudo-cubic structure with highly interconnected porous (Kim *et al.*, 2013). This possesses two types of cages corresponding to the octahedral (12.5 Å) and tetrahedral (6 Å) vacancies of a *cc* packing (Figure 4) accessible through triangular narrow windows of ca. 6 Å (Kim *et al.*, 2013).

Figure 3- MIL-125(Ti)_NH_2 granulates as provided by KRICT.

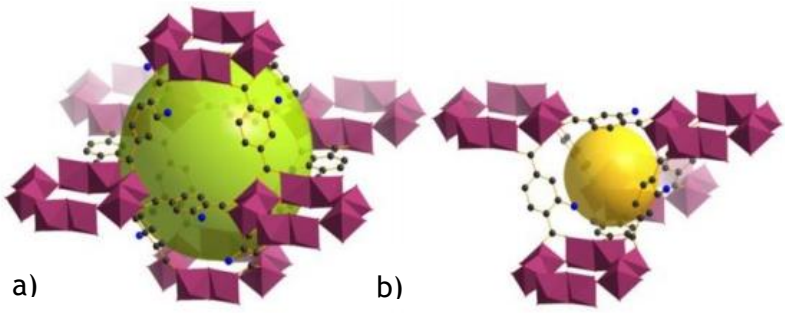

Figure 4 - Model of the a) octahedral and b) tetrahedral cages in MIL-125(Ti)_NH_2. $Ti_8O_8(OH)_4$ polyhedra, carbon, nitrogen and oxygen atoms are represented in violet, black, blue and red, respectively. Hydrogen atoms have been omitted (Vaesen *et al.*, 2013).

The MIL-125(Ti)_NH_2 granulates were characterized by helium pycnometry and mercury porosimetry at *Departamento de Engenharia Química da Faculdade de Engenharia da Universidade do Porto*, and scanning electron micrograph (SEM) / Energy Dispersive X-ray (EDS) at the *Centro de Materiais da Universidade do Porto* (CEMUP). The results of the He pycnometry and Hg porosimetry are provided in Table 1. In Figure 5, the SEM images of a granulate; its surface and its interior are presented. In Figure 5 (c) the crystals with a irregular shape but with narrow size distribution can be seen. The average crystal size is about 0.6 μm. The EDS spectra present the expected elements from the MIL-125(Ti)_NH_2 composition (C, O, Ti and N).

Table 1 - Mercury porosimetry and helium picnometry analysis.

Mercury porosimetry	
Total Intrusion Volume ($cm^3\ g^{-1}$)	1.1
Total Surface Area ($m^2\ g^{-1}$)	216.9
Apparent Density ($g\ cm^{-3}$)	0.55
Porosity	0.56
Helium picnometry	
Solid Density ($g\ cm^{-3}$)	1.45

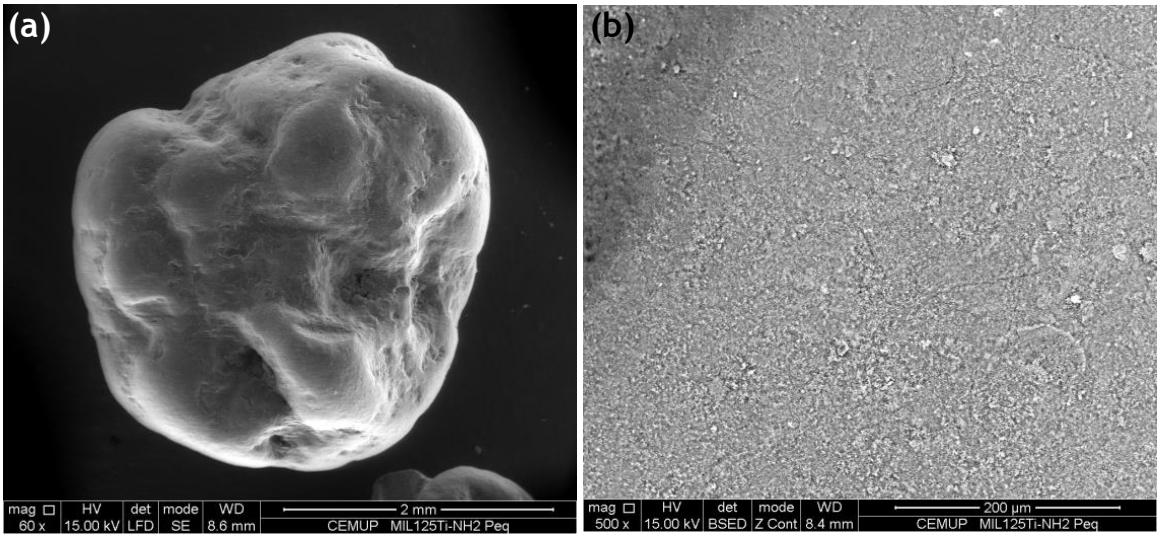

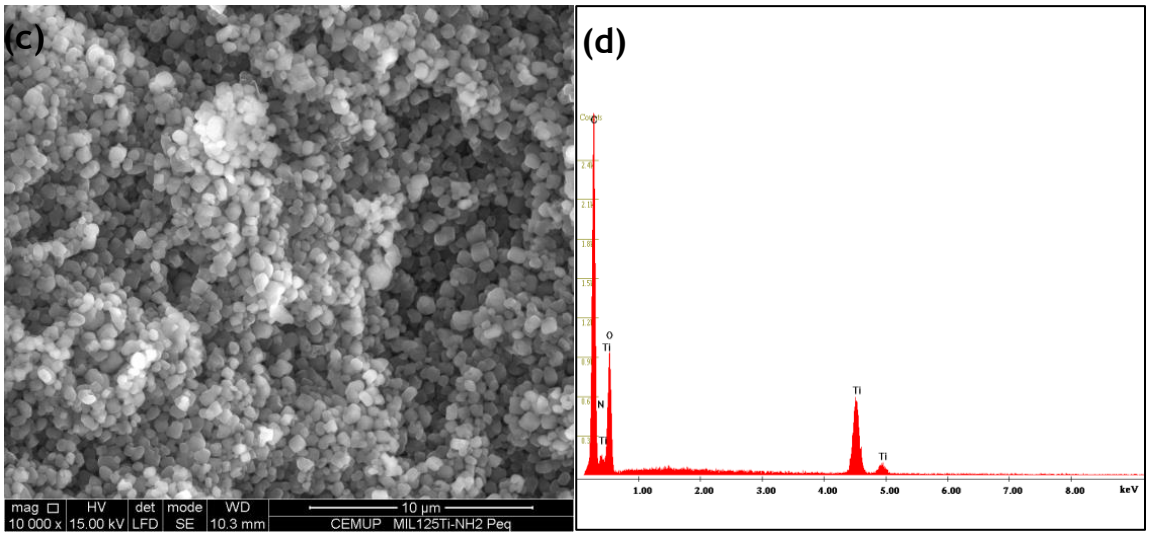

Figure 5 - SEM image of (a) a MIL-125(Ti)_NH_2 granulate, (b) granulate surface, (c) interior of the granulate showing the crystals and (d) EDX spectra from analysis.

3.1.2 Gases

The adsorption properties of the principle components of the synthesis gas were studied: H_2, CO_2, CO, CH_4 and N_2. Helium was also used for adsorbent activation and regeneration (considered as non-adsorbing). All gases were provided by Air Liquide with the following specifications: hydrogen N60, carbon dioxide N48, carbon monoxide N47, methane N35, nitrogen N45 and helium N50, which means purities greater than 99.9999, 99.998, 99.997, 99.95, 99.995, and 99.999%, respectively.

3.2 Methods

3.2.1 Adsorption equilibrium

Adsorption equilibrium is an important spontaneous phenomenon that allows the understanding of the adsorption processes. This is characterized by the contact between the fluid (gas or liquid), called adsorptive, with the surface of the solid, named adsorbent. So, the gas molecules become bounded to the surface of solid. The described process releases heat and after some time the adsorption equilibrium state is achieved. Adsorption studies are very important to understand both the equilibrium and the kinetics of single and multicomponent systems (Do, 1998).

For separations processes it is necessary to known the physical (physisorption) and chemical (chemisorption) interactions that are involved and the kinds of bonds formed, since they have different energies (Ruthven, 1984).

The adsorbate-adsorbent equilibrium can be studied through isotherms measurements. It consists in the measurement of the adsorbed concentration at different pressures or

concentrations at a constant temperature. After this, the measurements can be interpreted by many models available in literature.

The Langmuir Isotherm

The first coherent theory of adsorption onto a bare surface, based on a kinetic point of view, was proposed by Langmuir, in 1918. This theory predicts that the adsorption is a continuous process in which molecules move, maintaining zero rate of accumulation at the solid surface, at the equilibrium (Do, 1998). This model assumes some hypothesis:

- the adsorbent surface is energetically homogeneous, i.e. energy is constant over all sites (ΔH_{ads}) = constant;
- the probability of adsorbing is equal for every active site;
- each active site adsorbs only one molecule that does not interfere with the neighbor adsorbed molecules.

The Langmuir equation is:

$$q_i = q_{m,i} \frac{K_i P}{1 + K_i P} \quad (1)$$

where q_i is the adsorbed amount of the component i, $q_{m,i}$ is the maximum adsorption capacity of the adsorbent (only considering monolayer adsorption) of component i, K_i is the adsorption constant or Langmuir constant of component i, and P is the pressure. The Langmuir constant temperature dependency is expressed by the Van't Hoff equation:

$$K_i = {K_i}^0 e^{(-\Delta H/R_g T)} \quad (2)$$

where ${K_i}^0$ is the adsorption constant at infinite temperature, $(-\Delta H)$ is the heat of adsorption on the homogeneous surface, R_g is the universal gas constant and T is the temperature of the system.

For limit values of pressure, the Langmuir isotherm can be expressed as:

- low pressures: the term $K_i P$ is very small, $K_i P \ll 1$; so, equation (1 reduces to $\frac{q_i}{q_{i,m}} = K_i P$ (linear isotherm);
- high pressures: the term $K_i P$ is very large, $K_i P \gg 1$; so, equation (1 reduces to $q_i = q_{i,m}$, this means the capacity saturation of the adsorbent is complete.

The Freundlich Isotherm

In 1932, Freundlich became one of the earliest scientists to develop an empirical and nonlinear isotherm equation known as Freundlich isotherm. However, Mantell refers that this

equation was invented by Boedecker and Van Bemmelen (Seader *et al.*, 2011). This model considers the adsorption on non-uniform surface and is given by:

$$q_i = K_i P^{\frac{1}{n_i}} \tag{3}$$

where q_i is the adsorbed amount of component i, K_i and n_i are temperature-dependent constants for a particular component. The n_i can be calculated by:

$$n_i = A_i + B_i T \tag{4}$$

where A_i and B_i are parameters relating the thermal variation of the heterogeneity coefficient. K_i dependency on temperature is also given by the Van't Hoff equation ((2).

When n_i=1 (minimum admissible value), the isotherm obtained is linear. The larger the n_i value, more nonlinear the isotherm becomes. Freundlich equation is frequently used for gas phase adsorption in heterogeneous surfaces. But, for low pressures, it doesn't give the correct Henry law limit and at high pressures, it doesn't have a finite limit (Seader *et al.*, 2011).

The Langmuir-Freundlich Isotherm (Sips)

The Sips isotherm is an empirical equation and it is also called the Langmuir-Freundlich isotherm because it results from the combination between Langmuir and Freundlich equations ((1 and (3, respectively) (Do, 1998).

This isotherm is expressed by:

$$q_i = q_{m,i} \frac{(K_i P)^{\frac{1}{n_i}}}{1+(K_i P)^{\frac{1}{n_i}}} \tag{5}$$

where q_i is the adsorbed amount of component i, $q_{m,i}$ is the maximum adsorption capacity of the adsorbent, K_i and n_i are temperature-dependent constants for a particular component and adsorbent.

For *n*=1, the equation is applicable for ideal surfaces (Langmuir equation). Otherwise, this model can represent heterogeneous surfaces. But, as in the Freundlich law, the Henry law limit isn't obtained (Seader *et al.*, 2011).

The Toth Isotherm

The Toth isotherm is an empirical model that was developed to yield an improved fit, when compared with the empirical equations presented before. The Toth equation was developed

in 1971 and allows a good description of many systems with sub-monolayer coverage (Do, 1998). The Toth isotherm equation is given by:

$$q_i = q_{m,i}\frac{K_i P}{[1+(K_i P)^{n_i}]^{\frac{1}{n_i}}} \quad (6)$$

where q_i and $q_{m,i}$ are the adsorbed amount and the maximum adsorption capacity of component i, K_i and n_i are parameters specific for adsorbate-adsorbent pairs.

Once again, for *n*=1, the Toth isotherm reduces to Langmuir equation. As *n* deviates further away from unity, the system is said to be more heterogeneous. This isotherm assumes that adsorption occurs in only one layer and allows the interaction between adsorbed molecules (Do, 1998).

The Nitta Isotherm

This model, derived by Nitta *et al*. (1984), is based on the statistical thermodynamics and assumes that:

- the formation of only one adsorption layer occurs;
- the adsorbent surface is heterogeneous, which implies that one molecule adsorbs in more than one active center;

This model is represented by:

$$\frac{q_i}{q_{m,i}} = a_i K_i P\left[1-\frac{q_i}{q_{m,i}}\right]^{a_i} \quad (7)$$

where q_i and $q_{m,i}$ are the adsorbed amount and the maximum adsorption capacity of the adsorbent of the component i, respectively. The adsorption constant K_i is calculated by equation (2) and the exponent a_i corresponds to the number of neighboring sites that a molecule can occupy.

3.2.2 Isosteric heat of adsorption

The isosteric heat of adsorption can be estimated by the Clausius-Clapeyron equation (Do, 1998):

$$(-\Delta H_i) = R_g T^2\left(\frac{\partial \ln P_i}{\partial T}\right)_q \quad (8)$$

where ΔH_i is the isosteric heat of adsorption of component i, R_g is the universal gas constant and T is the temperature of the system. The derivative is evaluated at constant amount

adsorbed q. By plotting $\ln P_i$ versus $1/T$, it is possible to determine the isosteric heat of adsorption through the straight line equation with a slope equal to $\Delta H_i/R_g$.

3.2.3 Adsorption equilibrium experimental

The pure gases adsorption equilibrium isotherms were measured in a magnetic suspension microbalance (Rubotherm, Germany) with a precision of 0.01 mg. The experimental set-up used is shown in Figure 6 a). The inlet of the balance is connected to a system of valves, three-way and needle, for adsorptive addition. The outlet is connected to a K-type thermocouple to measure the temperature; to two pressure transducers, one that operates between 0 and 350 mbar and the other between 0 and 10 bar; and to a vacuum pump used for sample activation and cell depressurization. The temperature inside the cell is controlled by fluid circulation in the cell jacket. The thermostatic bath (Huber, Germany) shown in Figure 6 b) is used. The system control and data acquisition is done by a Labview software.

The measurements were performed for CO_2, CO, CH_4, N_2 and H_2, at 303, 323, and 343 K.

a)  b) 

Figure 6 - Magnetic suspension balance (Rubotherm, Bochum, Germany) a) magnetic suspense weighing (Rubotherm®); b) thermostatic bath.

Initially, approximately 2 g of adsorbent was placed in a basket suspended by the permanent magnet of the balance. The adsorbent was activated at 423 K under vacuum. The heating rate to reach this temperature was 1 K/min. In order to correct the buoyancy effects two helium pycnometries to the systems were performed, one with and other without the adsorbent (showed in Appendix 1). A small of amount of gas is added to the cell that contains the adsorbent sample to obtain one experimental point of the adsorption isotherm. The system monitories the pressure and weight variations and when the change in the weight is approximately zero equilibrium has been reached. Another small amount of gas is added to the cell and another equilibrium point is determined. This step is repeated until the high

desired pressure is achieved. Afterwards, the cell is progressively depressurized and desorption points of the isotherm are obtained.

In order to calculate the amount adsorbed it is necessary to correct for the buoyancy effect, in particularly for high pressures. This was performed according to the following equation (Ferreira *et al.*, 2011):

$$q = \frac{\Delta m + \rho_G (V_s + V_c)}{m_s M_w} \frac{\rho_L}{\rho_L - \rho_G} \tag{9}$$

where Δm is the difference of weight between one measurement and the previous one, V_S is the volume of the solid adsorbent, V_C is the volume of the permanent magnet, of the sample basket and of the glass wool used to hold the sample, ρ_G is the density the gas phase at the measuring conditions (T,P), ρ_L is the density of the adsorbed phase, m_S is the adsorbent mass, and M_w is the adsorbate molecular weight. V_S, V_C and m_S are measured by helium picnometry, assuming that helium is not adsorbed.

3.2.4 Fixed bed experimental

Breakthrough curves were performed in a lab-scale fixed-bed/PSA unit (Figure 7).This unit can work at temperatures between 298 and 423 K and in the pressure range of 0.1-5 bar.

A stainless steel column was used to pack the adsorbent material for breakthrough curves measurement. This column has 2.11 cm internal diameter and was packed with 40.2 g of MIL-125(Ti)_NH_2 which resulted in 32.3 cm of bed length. Along the bed are three thermocouples (TT) that allow following the temperature variations. TT are located at the 8.1 cm (bottom), 19.1 cm (middle) and 30 cm (top) from the beginning of the bed and are placed approximately at the center of the adsorbent bed, measuring the gas temperature. The characteristics of the column are given in Table 2.

The experiments were carried out at 323 K and 4.5 bar. The system pressure is controlled via a back-pressure regulator (BPR) from Bronkhorst which works between 0-5 bar. The feed is obtained from individual gas streams, through the accurate control of three mass flow controllers from Alicat Scientific. The total flow rate at the outlet of the column is assessed by a flow meter also from Alicat Scientific. The step-up is remotely and automatically controlled by Labview software. The temperature histories of the three thermocouples as well as the total flow rate at the outlet of the column were recorded during the breakthrough experiments.

The composition of the outlet stream was analyzed by gas chromatography. A Varian CP-3800 gas chromatographer (GC) was used, coupled with a system of two valves, a two position, 6-port automatic valve and a 16 loop valve to collect the samples.

The analysis was done using a Supelco GC packed column under isothermal conditions (483 K) and using a constant inert carrier gas flow rate, which was helium. A thermal conductivity detector (TCD) that operates at 453 K was used.

The schematic representation of the unit is shown in Figure 8.

Figure 7 - The fixed-bed/PSA experimental set-up connected to a GC analysis system (a) and the column with MIL-125(Ti)_NH_2.

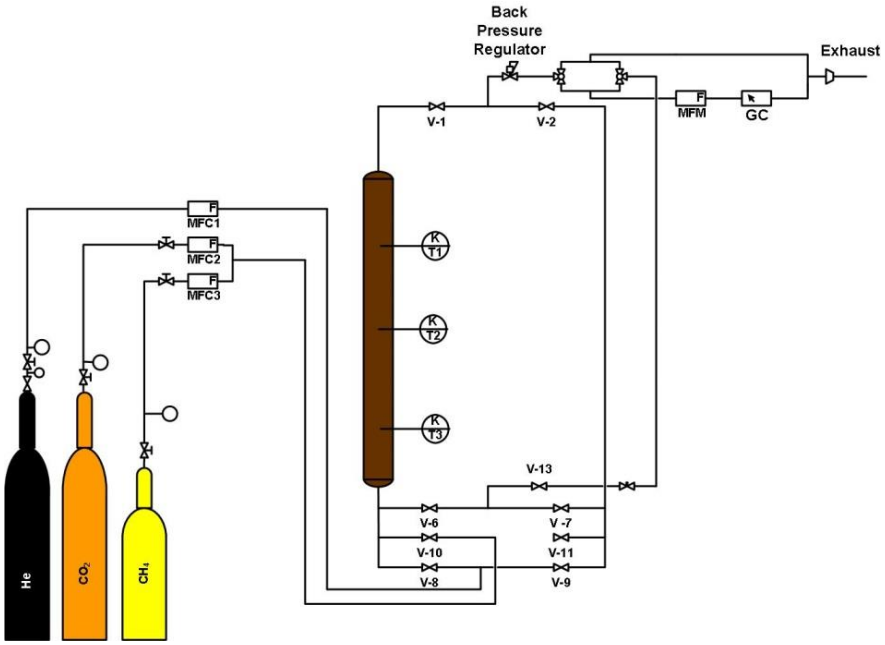

Figure 8- Schematic representation of the fixed-bed/PSA experimental set-up used for breakthrough measurement connected to a GC analysis system (adapted from Ferreira *et al.* (2014)).

Table 2 - Characteristics of the MIL-125(Ti)_NH_2 granulates, adsorption bed and feed stream under which the fixed bed experiments were performed.

Adsorbent MIL-125(Ti)_NH_2	
Shape	granulate
Hydrated adsorbent mass (g)	42.4
Dehydrated adsorbent mass (g)	40.2
Activation conditions	423 K, under 0.05 SLPM helium flow, overnight, heating rate of 0.5 K min^{-1}
Mass loss up on activation (wt. %)	5.2
Adsorbent average particle diameter (mm)	2.00
Adsorbent average crystal diameter (μm)	0.6
Particle bulk density (kg m^{-3})	549
Apparent (skeletal) particle density (kg m^{-3})	5488
Particle porosity	0.56
Adsorption bed	
Bed length (cm)	32.3
Bed diameter (cm)	2.11
Bed voidage	0.35
Bed density (kg m^{-3})	549
Feed	
Temperature (K)	323
Pressure (bar)	4.5
Flow rate (SLPM)	0.5

Initially, the column was packed with 42.4 g of the MIL-125(Ti)_NH_2 granulates. The adsorbent was active in situ under 0.05 SLPM helium flow rate at 423 K overnight. After the activation, the final mass of adsorbent is 40.2 g, which corresponds to 5.2% loss. A feed flow rate equal to 0.5 SLPM with different molar compositions was used in all test done at 323 K and 4.5 bar. When the bed is saturated with the feed, the procedure is repeated with helium or hydrogen at the same temperature and pressure.

3.2.5 Mathematical model

To describe the dynamic behavior of single or multicomponent adsorption in a fixed-bed it is necessary to write the material, energy and momentum balances (Da Silva, 1999). The energy balance is important because the adsorption is an exothermic process, and therefore the process is non isothermal. The variation in gas velocity along the bed is important as non-diluted system is being considered.

The following assumptions were made in order to write the necessary conservation equations:

- Ideal gas behavior throughout the column;

- No mass, heat or velocity gradients in the radial direction;
- Axial dispersed flow;
- External mass and heat transfer resistances expressed with the film model;
- Internal mass transfer resistance expressed with the Linear Driving Force (LDF) model;
- No temperature gradients inside each particle since the heat transfer in the solid particles is much faster than in the gas phase;
- Constant porosity along the bed;
- The Ergun equation is valid locally, i.e., in the momentum balance, only the terms of pressure drop and velocity change are considered.

The gas phase exchanges mass and energy with the solid phase and only energy with the column wall. The material balance for each component is in this phase given by:

$$\frac{\partial}{\partial z}\left(\varepsilon D_{ax} C_{g,T} \frac{\partial y_i}{\partial z}\right) - \frac{\partial}{\partial z}\left(u_0 C_{g,i}\right) - \varepsilon \frac{\partial C_{g,i}}{\partial t} - (1-\varepsilon) a_p k_f \left(C_{g,i} - C_{s,i}\right) = 0 \tag{10}$$

where z is the axial position, t is the time, ε is the bed porosity, u_0 is the superficial velocity, $C_{g,T}$ and $C_{g,i}$ are respectively the total and component i gas phase concentrations, y_i is the component i molar fraction, $C_{s,i}$ is the concentration of component i at the solid interface, D_{ax} is the mass axial dispersion coefficient, k_f is the film mass transfer coefficient and a_p is the particle external specific area.

In the momentum balance, the forces acting in a reference control volume are described, considering only the terms of pressure drop and velocity change, which are related through the Ergun equation defined by:

$$-\frac{\partial P}{\partial z} = \frac{150\mu(1-\varepsilon)^2}{\varepsilon^3 {d_p}^2} u_0 + \frac{1.75(1-\varepsilon)\rho}{\varepsilon^3 d_p} |u_0| u_0 \tag{11}$$

where P is the total pressure, μ is the gas viscosity, ρ is the gas density and d_p is the particle diameter.

The energy balance in the gas phase is written by:

$$\begin{aligned} &\frac{\partial}{\partial z}\left(\lambda \frac{\partial T_g}{\partial z}\right) - u_0 C_{g,T} C_p \frac{\partial T_g}{\partial z} + \varepsilon R_g T_g \frac{\partial C_{g,T}}{\partial t} \\ &-(1-\varepsilon) a_p h_f \left(T_g - T_p\right) - \frac{4h_w}{d_{wi}}\left(T_g - T_w\right) - \varepsilon C_{g,T} C_V \frac{\partial T_g}{\partial t} = 0 \end{aligned} \tag{12}$$

with T_g, T_p and T_w respectively as the gas, particle and wall temperatures; C_v and C_p as the gas molar specific heats at constant volume and pressure respectively; R_g as the ideal gas constant; d_{wi} as the wall internal diameter, λ as the heat axial dispersion coefficient. The film heat transfer coefficient between the gas phase and the particle is represented by h_f, while the heat transfer coefficient between the gas phase and the wall is represented by h_w.

The linear driving force model (LDF) is employed to describe the mass transfer rates in the solid phase. This approximation has a large impact on the computational time. The material balance in the solid phase is then given by:

$$\frac{\partial \overline{q_i}}{\partial t} = \frac{15 D_{p,i}}{{R_p}^2}(q_i^* - \overline{q_i}) \tag{13}$$

where $D_{p,i}$ is the pore diffusivity, R_p is the particle radius, $\overline{q_i}$ is the particle averaged adsorbed concentration, and q_i^* is the adsorbed concentration in equilibrium with $C_{s,i}$ calculated with the multicomponent extension of the Langmuir isotherm (14).

$${q_i}^* = q_{m,i}\frac{K_i P_i}{[1 + \sum_{j=1}^{n} K_j P_j]} \tag{14}$$

Equations (12) and (13) are linked with the fluxes equality at particle surface given by:

$$\frac{(1-\varepsilon) a_p k_f}{\rho_b}\left(C_{g,i} - C_{s,i}\right) = \frac{15 D_{p,i}}{R_p^2}(q_i^* - \overline{q_i}) \tag{15}$$

where ρ_b is the bulk density of the column.

Assuming that there are no temperature gradients inside an adsorbent particle, an energy balance averaged over the gas phase, the adsorbed phase and the solid phase inside a particle is given by:

$$\begin{aligned}&(1-\varepsilon)\left[\varepsilon_p \sum_{i=1}^{n} \overline{C_{p,i}} C_{v,i} + \rho_p \sum_{i=1}^{n} \overline{q_i} C_{v,ads,i} + \rho_p \hat{C}_{ps}\right]\frac{\partial T_p}{\partial t} \\ &= (1-\varepsilon)\varepsilon_p R_g T_p \frac{\partial \overline{C_{p,T}}}{\partial t} + \rho_b \sum_{i=1}^{n} (-\Delta H_{ads})_i \frac{\partial \overline{q_i}}{\partial t} + (1-\varepsilon) a_p h_f (T_g - T_p)\end{aligned} \tag{16}$$

where $\hat{C}_{ps}$ is the solid specific heat per mass unit and $(-\Delta H_{ads})_i$ is the heat of adsorption of component i.

An energy balance to the column wall considers that it interchanges energy with the gas phase inside the column and with the external environment being expressed as:

$$\rho_w \hat{C}_{p,w} \frac{\partial T_w}{\partial t} = \alpha_w h_w (T_g - T_w) - \alpha_{wl} U (T_w - T_\infty) \quad (17)$$

where T_∞ is the external temperature, ρ_w is the wall density, $\hat{C}_{p,w}$ is the wall specific heat per mass unit, U is the overall heat transfer coefficient and α_w and α_{wl} are defined by:

$$\alpha_w = \frac{d_{wl}}{e(d_{wl} + e)} \quad (18)$$

$$\alpha_{wl} = \frac{2}{(d_{wl} + e) \ln\left(\frac{d_{wl} + 2e}{d_{wl}}\right)} \quad (19)$$

where e is the wall thickness.

In order to solve this system of partial differential equations initial and boundary conditions are needed. In breakthrough experiments with the column initially filled with helium, inert gas, and in which the pressure is controlled at the end of the column, such conditions are:

Initial conditions

$y_i = q_i = 0$ for $i \neq inert$

$y_{inert} = 1$

$C_{g,T} = C_{g,T\,inlet}$

$T_g = T_p = T_w = T_{inlet}$

Boundary conditions

z = 0, inlet:

$$u_{0inlet} C_{inlet,i} = u_0 C_{g,i} - \varepsilon D_{ax} C_{g,T} \frac{\partial y_i}{\partial z}$$

$$u_{0inlet} C_{inlet,T} = u_0 C_{g,T}$$

$$u_{0inlet} C_{inlet,T} C_p T_{inlet} = u_0 C_{g,T} C_p T_g - \lambda \frac{\partial T_g}{\partial z}$$

z = L, outlet:

$$\frac{\partial C_{g,i}}{\partial z} = 0$$

$$P = P_{exit}$$

$$\frac{\partial T_g}{\partial z} = 0$$

Some transport parameters appear in the model equations and must be calculated. The following relations were used.

The pore diffusivity ($D_{p,i}$) is calculated with the Bosanquet equation (Prausnitz *et al.*, 2001):

$$\frac{1}{D_{p,i}} = \tau_p \left(\frac{1}{D_{m,i}} + \frac{1}{D_{k,i}} \right) \tag{20}$$

where $D_{m,i}$ is the molecular diffusivity for component i, $D_{k,i}$ is Knudsen diffusivity for component i and τ_p is the particle tortuosity. The molecular diffusivity for the mixture is given by (Prausnitz *et al.*, 2001):

$$D_{m,i} = \frac{1 - y_i}{\sum_{j=1, j \neq i}^{n} \frac{y_j}{D_{ij}}} \tag{21}$$

where y_i is the molar fraction of component i and D_{ij} is the binary molecular diffusivity, that it is calculated by Chapman-Enskog equation (Prausnitz *et al.*, 2001):

$$D_{ij} = \frac{2.66 \times 10^{-2} T^{\frac{3}{2}}}{P M_{ij}^{\frac{1}{2}} \sigma_{ij}^2 \Omega_D} \tag{22}$$

where P and T represents the pressure and temperature of the system, M_{ij} is the molecular weight of the mixture between component i and j, σ_{ij} is the binary constant parameter and Ω_D is the collision integral.

The Knudsen diffusivity is calculated by:

$$D_{k,i} = 0.97 r_p \sqrt{\frac{T_g}{M_i}} \tag{23}$$

where r_p is the pore radius in cm, T_g is the gas temperature and M_i is the molecular weight of the adsorbate of component i.

The Wakao and Funazkri correlations, valid for 3 < Re < 10000, allow the calculation of the axial mass and heat dispersions coefficients and the mass and heat transfer coefficients (Prausnitz *et al.*, 2001):

$$\frac{\varepsilon D_{ax}}{D_m} = 20 + 0.5\, Sc\, Re \tag{24}$$

where ε is the porosity, D_{ax} is the axial dispersion coefficient, D_m is the diffusivity for the mixture, Sc and Re are the Schmidt and Reynolds numbers, and:

$$\frac{\lambda}{k_g} = 7 + 0.5\, Pr\, Re \tag{25}$$

where λ is the heat axial dispersion coefficient, k_g is the thermal conductivity of gas and Pr is the Prandtl number.

$$Sh = 2.0 + 1.1 Re^{0.6} Sc^{\frac{1}{3}} \tag{26}$$

$$Nu = 2.0 + 1.1 Re^{0.6} Pr^{\frac{1}{3}} \tag{27}$$

where Nu is the Nusselt number.

In order to use the correlations mentioned above other properties must be calculated. The equations required for these calculations are presented in Appendix 2.

3.2.6 PSA

In cyclic adsorption processes, among which is the pressure swing adsorption, there are two steps involved: adsorption and desorption. In adsorption step, the heavier components are more adsorbed in the adsorbent and the lighter components elute to the end of the bed. In desorption, the heavier components are removed from the bed, and therefore the adsorbent is partially regenerated and the column is ready for a new cycle.

A PSA cycle is a sequence of several steps such as pressurization, feed, rinse, blowdown, and purge. The feed, rinse and purge steps are done at constant pressure. In blowdown and pressurization steps, the pressure changes with time. An exponential decrease with the time is assumed to represent the pressure change during the blowdown step (approximate representation of the valve).

In the simulation of the PSA process the same equations presented in the previous section (3.2.5) are used, coupled with the appropriate boundary conditions for each step, presented in Table 3.

Table 3 - Boundary conditions suitable for PSA process.

Pressurization with feed	
$z = 0$, inlet	$z = L$
$u_{0inlet} C_{inlet,i} = u_0 C_{g,i} - \varepsilon D_{ax} C_{g,T} \frac{\partial y_i}{\partial z}$	$\frac{\partial C_{g,i}}{\partial z} = 0$
$P = P_{inlet}$	$u_0 = 0$
$u_{0inlet} C_{inlet,T} C_p T_{inlet} = u_0 C_{g,T} C_p T_g - \lambda \frac{\partial T_g}{\partial z}$	$\frac{\partial T_g}{\partial z} = 0$
Feed	
$z = 0$, inlet	$z = L$, outlet
$u_{0inlet} C_{inlet,i} = u_0 C_{g,i} - \varepsilon D_{ax} C_{g,T} \frac{\partial y_i}{\partial z}$	$\frac{\partial C_{g,i}}{\partial z} = 0$
$u_{0inlet} C_{inlet,T} = u_0 C_{g,T}$	$P = P_{outlet}$
$u_{0inlet} C_{inlet,T} C_p T_{inlet} = u_0 C_{g,T} C_p T_g - \lambda \frac{\partial T_g}{\partial z}$	$\frac{\partial T_g}{\partial z} = 0$
Counter-current blowdown	
$z = 0$, outlet	$z = L$
$\frac{\partial C_{g,i}}{\partial z} = 0$	$\frac{\partial C_{g,i}}{\partial z} = 0$
$P = P_{outlet}$	$u_0 = 0$
$\frac{\partial T_g}{\partial z} = 0$	$\frac{\partial T_g}{\partial z} = 0$
Purge	
$z = 0$, outlet	$z = L$, inlet
$\frac{\partial C_{g,i}}{\partial z} = 0$	$u_{0inlet} C_{inlet,i} = u_0 C_{g,i} - \varepsilon D_{ax} C_{g,T} \frac{\partial y_i}{\partial z}$
$P = P_{outlet}$	$u_{0inlet} C_{inlet,T} = u_0 C_{g,T}$
$\frac{\partial T_g}{\partial z} = 0$	$u_{0inlet} C_{inlet,T} C_p T_{inlet} = u_0 C_{g,T} C_p T_g - \lambda \frac{\partial T_g}{\partial z}$

4 Results and Discussion

4.1 Adsorption equilibrium

4.1.1 Isotherms

Adsorption equilibrium of CO_2, N_2, CH_4 and H_2 on MIL-125(Ti)_NH_2 (KRICT) was determined at 303, 323 and 343 K in the pressure range of 0 to 7 bar. The adsorption equilibrium of CO was measured at the same three temperatures but in the pressure range of 0 to 1 bar. The results are presented in Figure 9.

a)

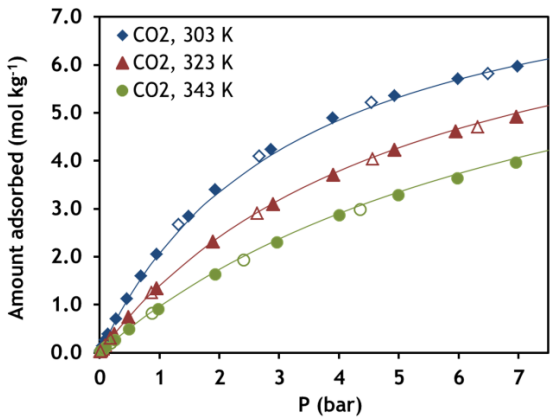

b)

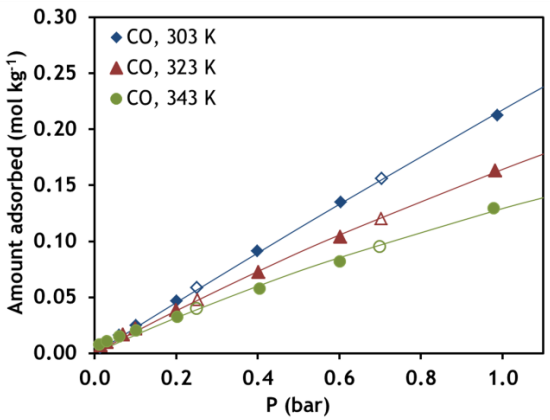

c)

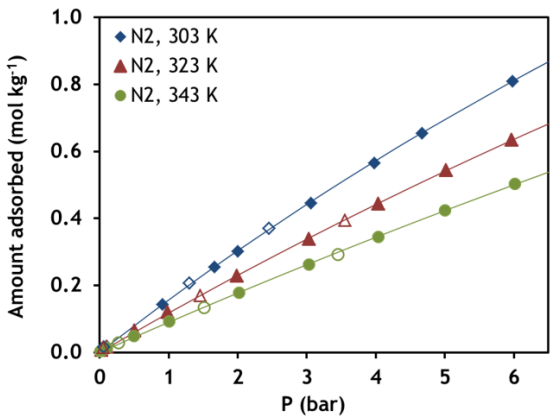

d)

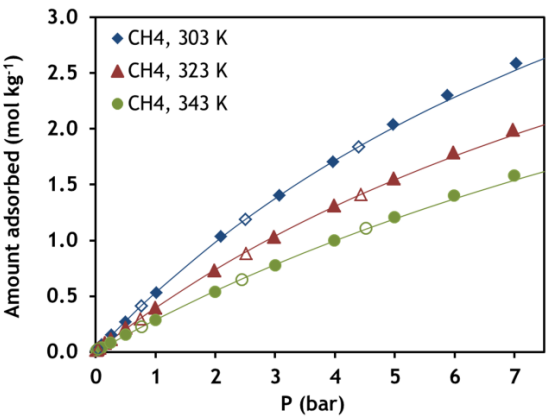

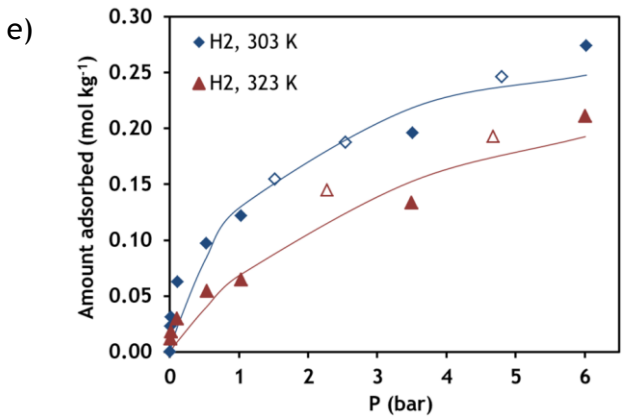

Figure 9 - Amount of a) CO_2, b) CO, c) N_2, d) CH_4 and e) H_2 adsorbed on MIL-125(Ti)_NH_2: experimental points (closed adsorption, open desorption) at 303 (◆), 323 (▲), 343 K (●) and ─ Langmuir isotherm fitting.

In these graphics, closed and open symbols represents points determined for adsorption and desorption, respectively. No hysteresis was observed for any of the adsorbates at the three different temperatures.

The results were fitted with the Langmuir isotherm (equation (1). The parameters of this isotherm for each adsorbate, q_m, K_i^0 and $(-\Delta H)$, were obtained by minimizing the sum of absolute errors between the calculated and experimental values with the Excel Solver add-in. The values obtained are given in Table 4.

Table 4 - Fitting parameters of the Langmuir model for CO_2, CO, N_2, CH_4 and H_2 adsorption equilibrium on MIL-125(Ti)_NH_2.

Species	q_m (mol kg^{-1})	K_i^0 (bar^{-1})	$(-\Delta H)$ (kJ mol^{-1})
CO_2	8.509	0.5782×10^{-5}	21.9
CO	5.229	3.2700×10^{-4}	11.9
N_2	5.377	2.8069×10^{-4}	11.7
CH_4	7.093	2.4223×10^{-4}	14.6
H_2	0.294	9.3900×10^{-7}	35.3

In general a good fitting is obtained, except for H_2 for which higher deviations are observed (Schell *et al.*, 2012). As hydrogen has low molecular weight, a small change in the mass of

adsorbent causes large changes in the amount adsorbed (mol per kilogram). Therefore, the error in the hydrogen measurement is large (Schell *et al.*, 2012).

It is possible to observe the following order of adsorption: CO_2 > CH_4 > CO > N_2 > H_2, from the most adsorbed to the less adsorbed.

The MIL-125(Ti)_NH_2 is a isostructural material of MIL-125(Ti) where the H atoms are substituted on the phenyl rings with the NH_2 functional groups (Vaesen *et al.*, 2013). When comparing the two materials it is observed that the heats of CO_2 adsorption for the material contained NH_2 are higher than for the material without NH_2 (Kim *et al.*, 2013).

4.1.2 Isosteric heat adsorption

From the adsorption equilibrium results, it is possible to determine the experimental isosteric heat of adsorption as function of the loading. For this, the Clausius-Clapeyron - equation (8) was employed as described in section 3.2.1.1 (Do, 1998). The results obtained are presented in Figure 10 where they are also compared with the heats of adsorption obtained through the Langmuir isotherm model. A good agreement was found.

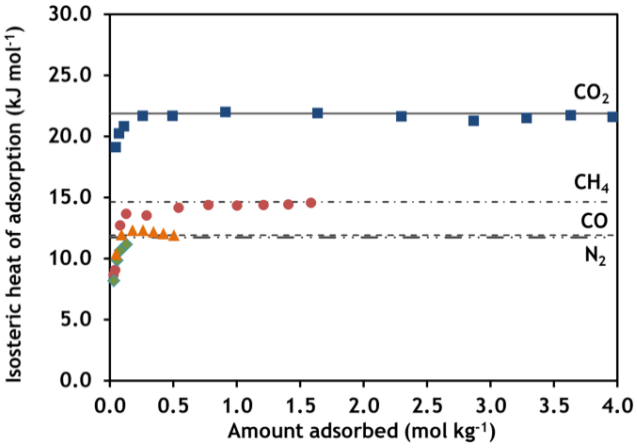

Figure 10 - Single-component isosteric heats of adsorption on MIL-125(Ti)_NH_2 for CO_2 (■), CH_4 (●), N_2 (▲) and CO (◆) as a function of amount adsorbed in the temperature range of 303-343 K; Lines are the values obtained through the Langmuir fitting.

Comparing the heats of adsorption of this material with values reported in the literature, one can observe that the values obtained in work are slightly lower (Kim *et al.*, 2013).

4.2 Fixed bed

Single, binary and ternary breakthrough curves were measured in accordance with the experimental conditions given in Table 5. Each breakthrough curve was simulated with

gProms using the mathematical model described in section 3.2.4. The experimental results and simulations results are compared.

At the beginning of each experiment, the column is filled with He or H_2 at the feed temperature and pressure. The gas mixture is fed the column until saturation. This step corresponds to the adsorption. After this, the inlet stream was changed to helium or hydrogen and desorption step start. In adsorption and desorption steps, the total volumetric flow rate is kept constant. The temperature histories and the volumetric flow rate were recorded. Samples of the outlet stream were collected in the loops and the molar composition was determined by chromatography.

Some breakthrough tests had already been performed at LSRE before the start of this thesis (but not simulated). Therefore, the fixed bed results will be presented in two stages: experiments 1 to 7 (Exp.1 to Exp.7) that correspond to tests and simulations performed in this thesis; experiments 8 to 20 (Exp.8 to Exp.20) are the tests performed previously and simulated in this work. The experimental conditions used in breakthrough curves 8 to 20 are given in Table 6.

Table 5 - Experimental conditions used in the breakthrough curves performed with MIL-125(Ti)_NH_2.

Experiment	Exp.1	Exp.2	Exp.3	Exp.4	Exp.5	Exp.6	Exp.7
Temperature (K)	323	323	323	323	323	323	323
Pressure (bar)	4.5	4.5	4.5	4.5	4.5	4.5	4.5
Flow rate (mmol s^{-1}) [a]	0.359	0.345	0.369	0.362	0.382	0.367	0.389
Starting of desorption (s)	4004	5304	5754	5754	8404	8404	8504
Desorption gas	He	He	He	He	H_2	H_2	H_2
Column initial conditions [b]	He	He	He	He	H_2	H_2	H_2
Feed molar fraction	CO_2: 0.358 He: 0.642	CO_2: 0.324 H_2: 0.676	CO_2: 0.375 CH_4: 0.625	CO_2: 0.189 CH_4: 0.811	CO_2: 0.279 CH_4: 0.077 H_2: 0.644	CO_2: 0.249 N_2: 0.042 H_2: 0.709	CO_2: 0.266 CO: 0.235 H_2: 0.499

[a] Flow rate of adsorption (with feed) and desorption (with He or H_2) steps.
[b] At the beginning of each experiment, the column was saturated with He or H_2.

Table 6 - Experimental conditions used in the breakthrough curves performed with MIL-125(Ti)_NH_2 (Exp.8 to 20).

Experiment	Exp.8	Exp.9	Exp.10	Exp.11	Exp.12	Exp.13	Exp.14
Temperature (K)	323	323	323	323	323	323	323
Pressure (bar)	4.5	4.5	4.5	4.5	4.5	4.5	4.5
Flow rate (mmol s^{-1}) [a]	0.353	0.380	0.274	0.290	0.346	0.445	0.139
Starting time of desorption (s)	3474	3706	3004	3004	3600	3608	3000
Desorption gas	He	He	He	He	He	He	He
Column initial conditions [b]	He	He	He	He	He	He	He
Feed molar fraction	CO_2: 0.416 He: 0.594	CO_2: 0.842 He: 0.158	CO: 0.080 He: 0.920	CO: 0.215 He: 0.785	N_2: 0.178 He: 0.822	N_2: 0.829 He: 0.171	H_2: 0.570 He: 0.430

Experiment	Exp.15	Exp.16	Exp.17	Exp.18	Exp.19	Exp.20
Temperature (K)	323	323	323	323	323	323
Pressure (bar)	4.5	4.5	4.5	4.5	4.5	4.5
Flow rate (mmol s^{-1}) [a]	0.242	0.245	0.385	0.439	0.286	0.272
Starting time of desorption (s)	4004	4008	4704	4704	4214	4504
Desorption gas	He	He	He	He	He	He
Column initial conditions [b]	He	He	He	He	He	He
Feed molar fraction	CH_4: 0.199 He: 0.801	CH_4: 0.789 He: 0.211	CO_2: 0.425 N_2: 0.080 He: 0.495	CO_2: 0.687 N_2: 0.113 He: 0.200	CO_2: 0.390 CO: 0.069 He: 0.541	CO_2: 0.708 CO: 0.174 He: 0.118

[a] Flow rate of adsorption (with feed) and desorption (with He or H_2) steps.
[b] At the beginning of each experiment, the column was saturated with He or H_2.

The results of the experiments are presented in Figure 11 to Figure 19, for the first group (Exp.1 to Exp.7) and in Figure A4.1 to Figure A4.13, for the second group (Exp.8 to Exp.20) presented in Appendix 4. In these figures graphic (a) presents the molar flow rate of each component at the column outlet, graphic (b) shows the molar fraction history of each component at the column outlet, graphic (c) presents the temperature history at the bottom (8.1 cm), middle (19.1 cm) and top (30 cm) positions in the column and graphic (d) shows the total flow rate at the column outlet. These graphs present experimental data (points) and simulations results (lines).The transport parameters values required for the simulations are shown respectively in Table 7 and Table 8 for the two groups of tests. These parameters were

calculated at feed conditions using the correlations presented in mathematical model section (3.2.5) and were kept constant during the simulations.

Experiment 1 represents a single breakthrough curve of carbon dioxide and is shown in Figure 11.

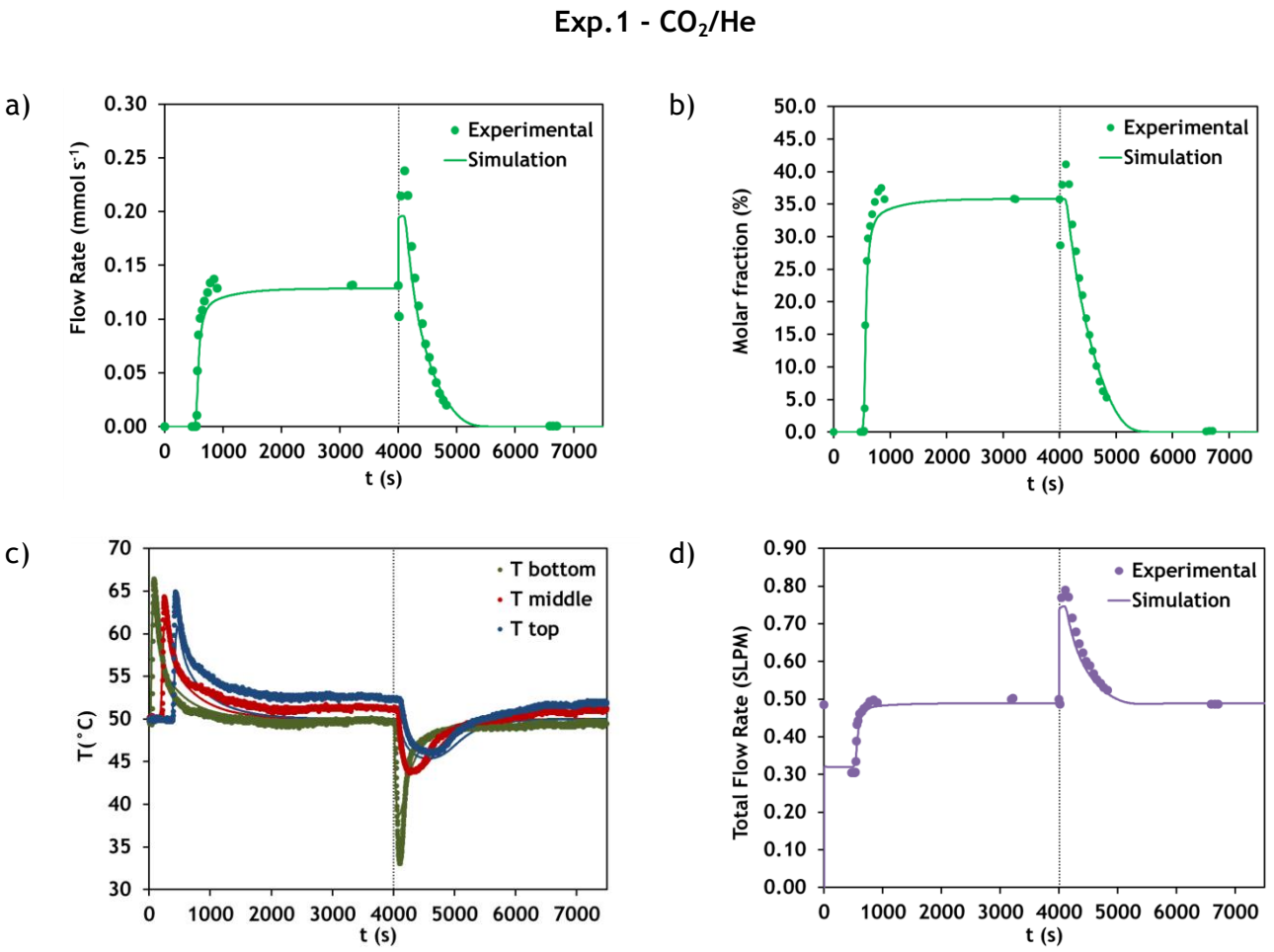

Figure 11 - Breakthrough results of experiment 1 (CO_2/He): molar flow rate at the column outlet (a), molar fraction at the column outlet (b), temperatures histories at 8.1 cm (bottom), 19.1 cm (middle) and 30 cm (top) (c) and total flow rate at the column outlet (d). Points correspond to experimental data and lines to simulation results. Vertical line corresponds to the beginning of desorption.

The time which the CO_2 takes to reach the top of the column is the breakthrough time. In this moment, it is possible to verify an increase in CO_2 molar flow and molar fraction. This represents the adsorption step. At the beginning of desorption, an increase in the flow rate is observed due to the release of the adsorbed gas and afterwards the flow starts to decrease. In the temperature histories (graphic c), it is possible to see an increase of temperature due to the adsorption while in the desorption step a dwell in the temperature occurs. The simulation represents well the experimental results of the single component CO_2 breakthrough.

A binary breakthrough curve with a carbon dioxide and hydrogen was performed. The results are given in Figure 12.

Exp.2 - CO_2/H_2

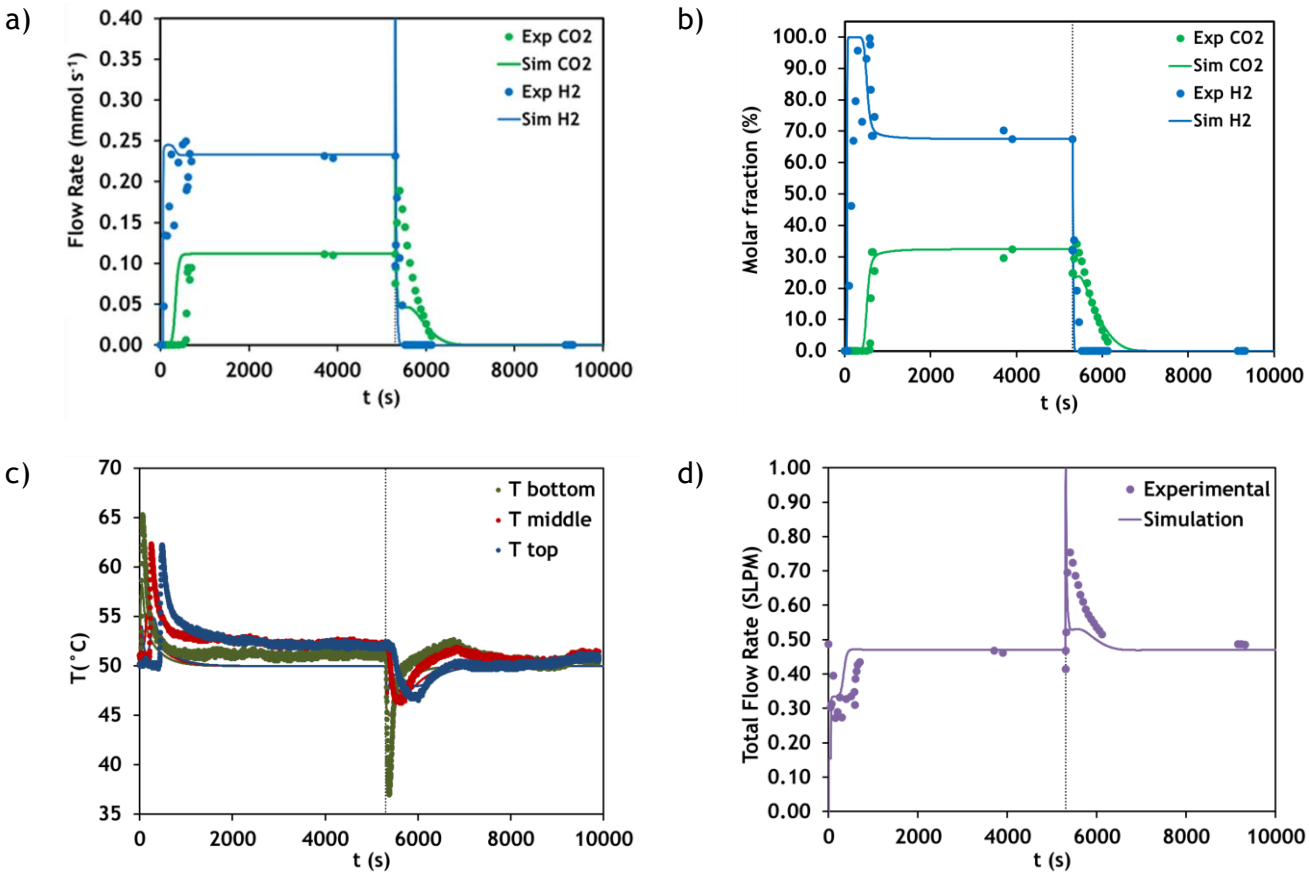

Figure 12 - Breakthrough results of experiment 2 (CO_2/H_2): molar flow rate at the column outlet (a), molar fraction at the column outlet (b), temperatures histories at 8.1 cm (bottom), 19.1 cm (middle) and 30 cm (top) (c) and total flow rate at the column outlet (d). Points correspond to experimental data and lines to simulation results. Vertical line corresponds to the beginning of desorption.

In this case a significant difference between the experimental and simulation results are observed. Competitive adsorption of CO_2 and H_2 predicted with multicomponent extended Langmuir isotherm (14) was considered in the simulation of experiment 2. It can be seen that the predicted decrease of the adsorption capacity of CO_2 due to the presence of H_2, is not observed experimentally. To explain this deviation between experiment and simulation two hypothesis were made, leading to two new simulations. The first one assumes that H_2 doesn't adsorb ($K_i^0 = 0$) and the second assumes that H_2 adsorbs without competition with the gases (in this case CO_2). The results obtained are given in Figure 13 and Figure 14, respectively. In both cases, the values of the transport parameters used were the same (see Table 7).

Exp.2 - CO_2/H_2 (with $K_i^0 = 0$)

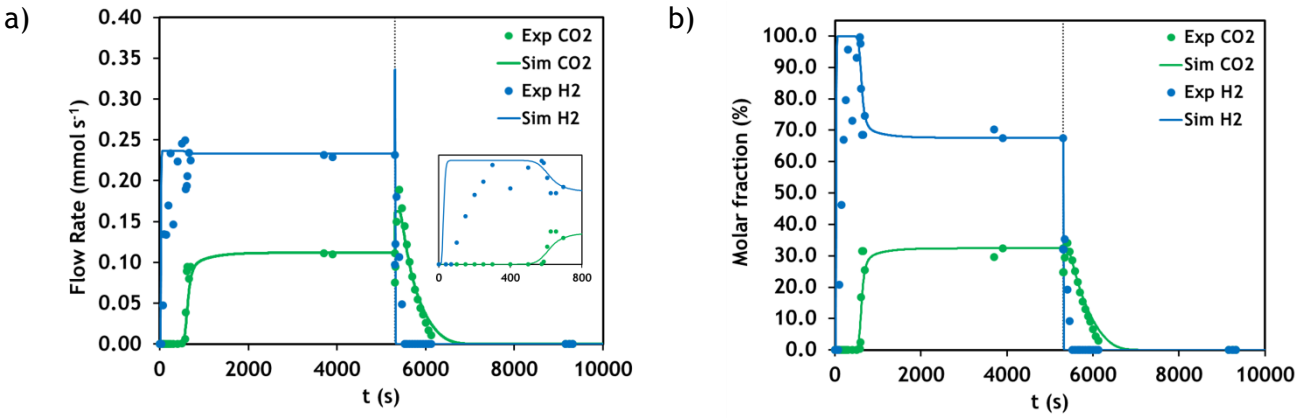

Figure 13 - Breakthrough results of experiment 2 (CO_2/H_2) with $K_i^0 = 0$: flow rate at the column outlet (a) and molar fraction at the column outlet (b). Points correspond to experimental data and lines to simulation results. Vertical line corresponds to the beginning of desorption.

Exp.2 - CO_2/H_2 (without competition of H_2)

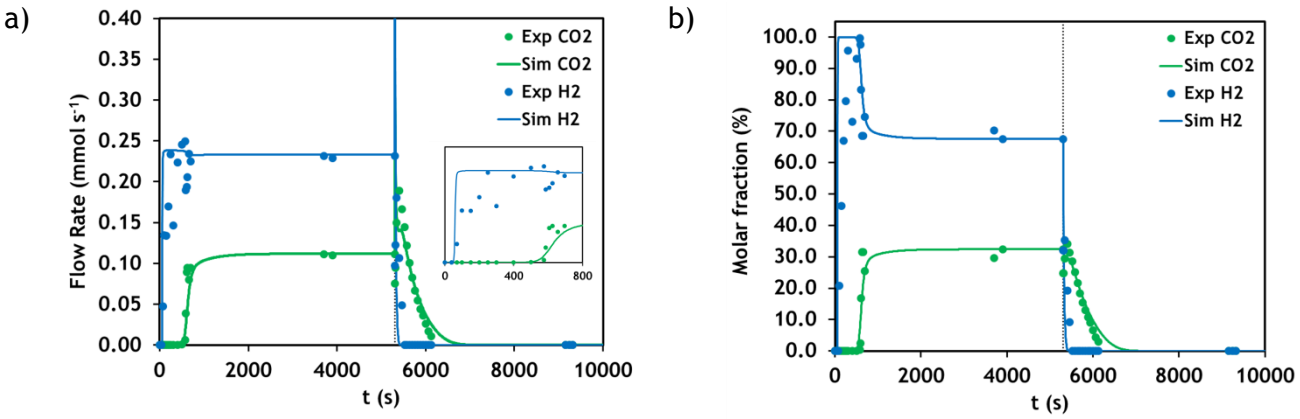

Figure 14 - Breakthrough results of experiment 2 (CO_2/H_2) without competition of H_2: flow rate at the column outlet (a) and molar fraction at the column outlet (b). Points correspond to experimental data and lines to simulation results. Vertical line corresponds to the beginning of desorption.

In these figures, it can observe that when it is considered that hydrogen doesn't adsorb in MIL-125(Ti)_NH_2 (Figure 13), the CO_2 front is well predicted but H_2 breakthrough earlier than observed experimentally and therefore this hypothesis cannot explain the deviation neither predict the experimental results. When non-competitive adsorption is considered (Figure 14), the simulation predicts well the behavior of both compounds, including the breakthrough time of H_2. Nevertheless it should be noticed that values of the determined hydrogen composition has large errors. This is because the analysis was done with TCD that compares the conductivity of helium and other gases, and as the conductivity of He and H_2 is very

similar, the detector sensibility is lower and the error for hydrogen measurements is higher than for the other compounds. These comparisons seem to show that the second hypothesis represents better the experimental results and therefore it will be used to simulate all other runs, which is competitive adsorption of all compounds except H_2 will be considered.

Two binary breakthrough curves of mixtures containing carbon dioxide and methane were performed feeding two different compositions. They are shown in Figure 15 and Figure 16. These binary breakthrough curves are well predicted by the simulation, including the height of the typical roll-up observed when competitive adsorption occurs.

Exp.3 - CO_2/CH_4

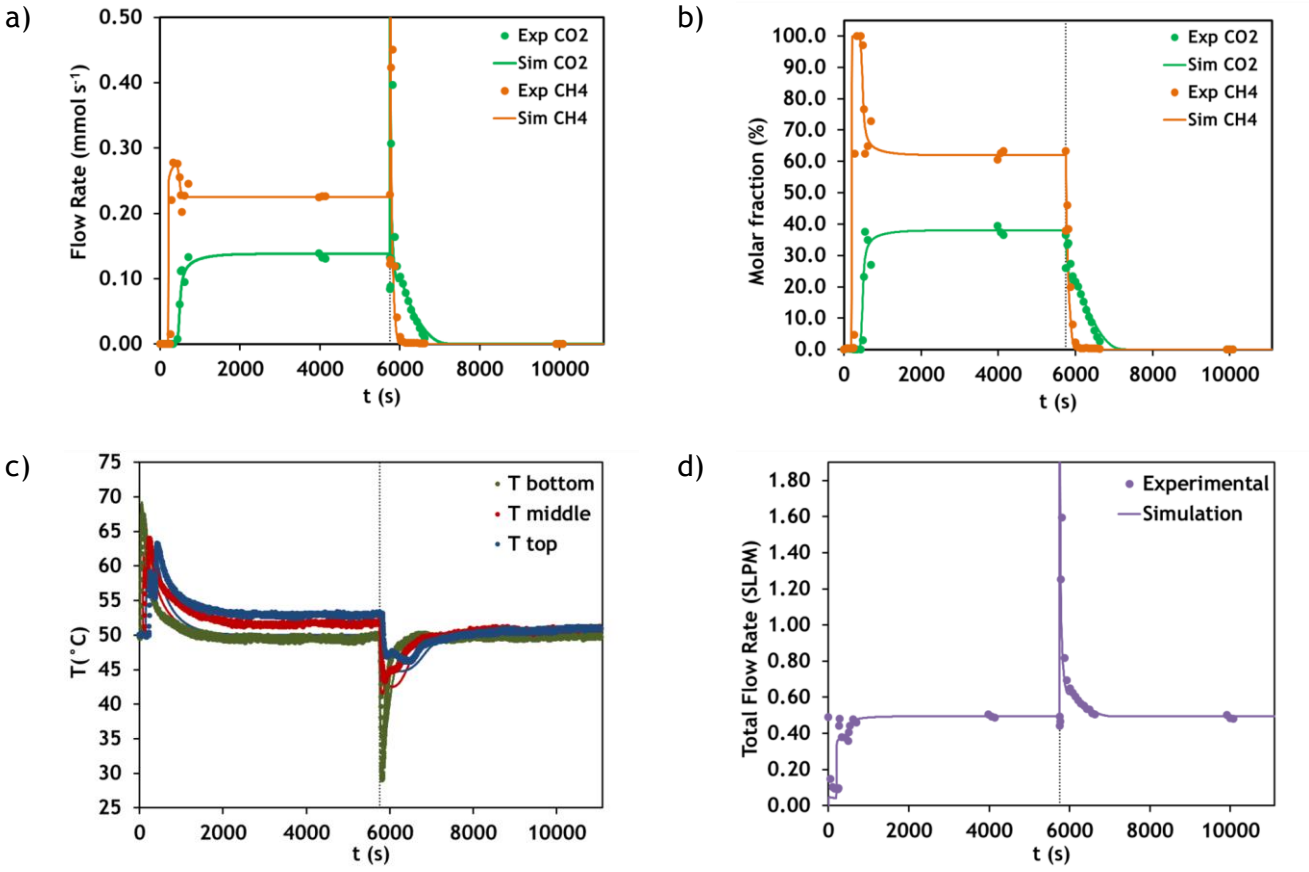

Figure 15 - Breakthrough results of experiment 3 (CO_2/CH_4): molar flow rate at the column outlet (a), molar fraction at the column outlet (b), temperatures histories at 8.1 cm (bottom), 19.1 cm (middle) and 30 cm (top) (c) and total flow rate at the column outlet (d). Points correspond to experimental data and lines to simulation results. Vertical line corresponds to the beginning of desorption.

Exp.4 - CO_2/CH_4

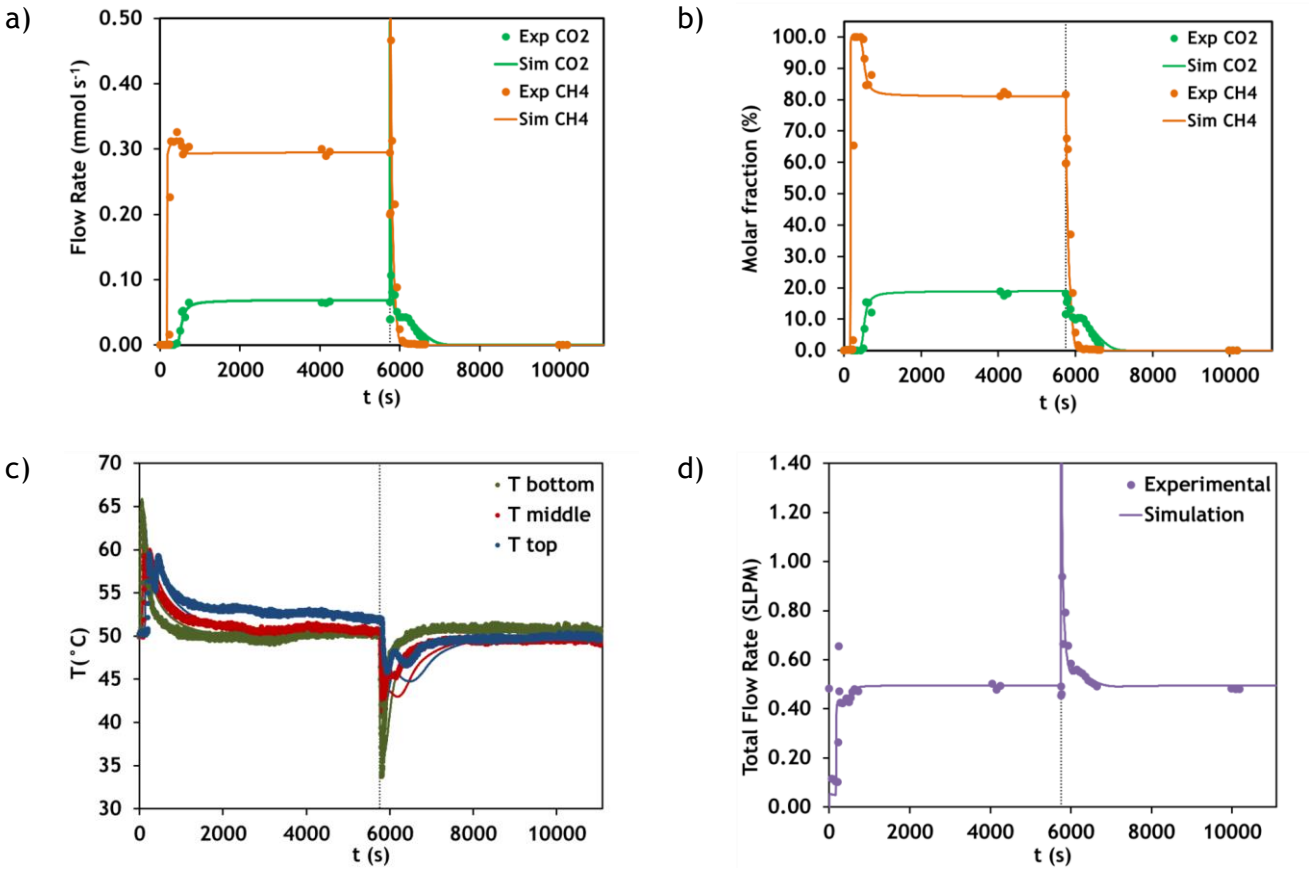

Figure 16 - Breakthrough results of experiment 4 (CO_2/CH_4): molar flow rate at the column outlet (a), molar fraction at the column outlet (b), temperatures histories at 8.1 cm (bottom), 19.1 cm (middle) and 30 cm (top) (c) and total flow rate at the column outlet (d). Points correspond to experimental data and lines to simulation results. Vertical line corresponds to the beginning of desorption.

A ternary breakthrough curve with a carbon dioxide, methane and hydrogen mixture was performed. The results are presented in Figure 17.

Exp.5 - $H_2/CO_2/CH_4$

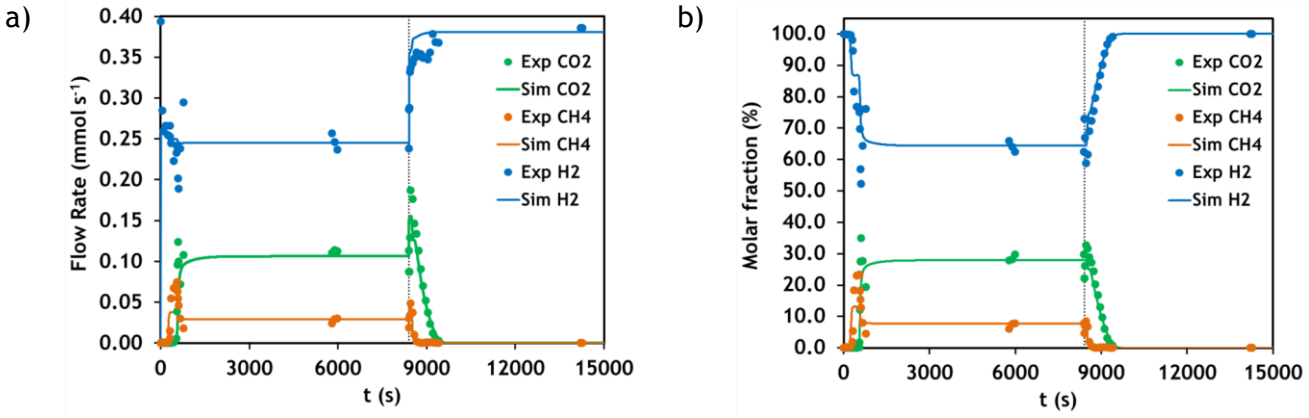

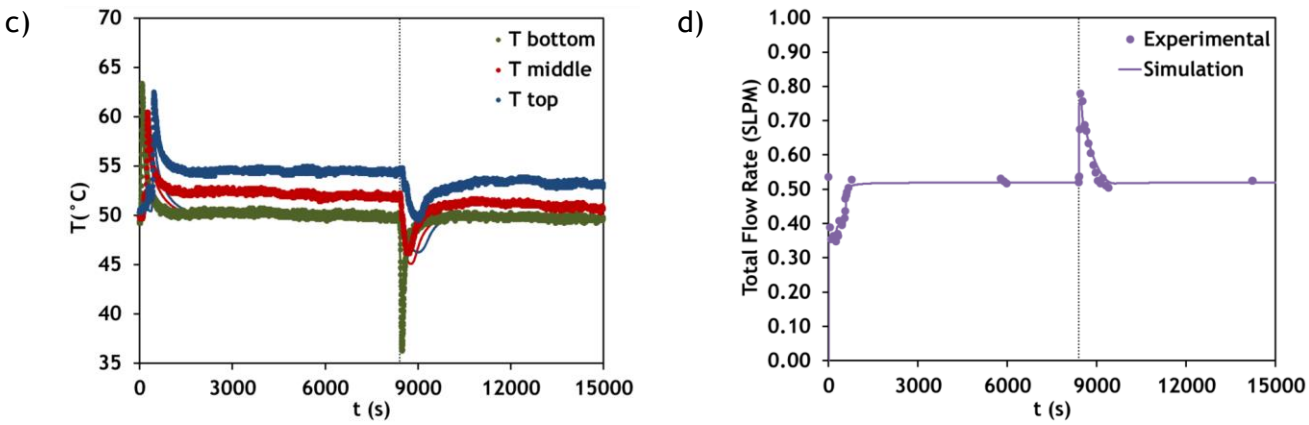

Figure 17 - Breakthrough results of experiment 5 ($H_2/CO_2/CH_4$): molar flow rate at the column outlet (a), molar fraction at the column outlet (b), temperatures histories at 8.1 cm (bottom), 19.1 cm (middle) and 30 cm (top) (c) and total flow rate at the column outlet (d). Points correspond to experimental data and lines to simulation results. Vertical line corresponds to the beginning of desorption.

The results of the ternary breakthrough curve with carbon dioxide, nitrogen and hydrogen are given in Figure 18.

Exp.6 - $H_2/CO_2/N_2$

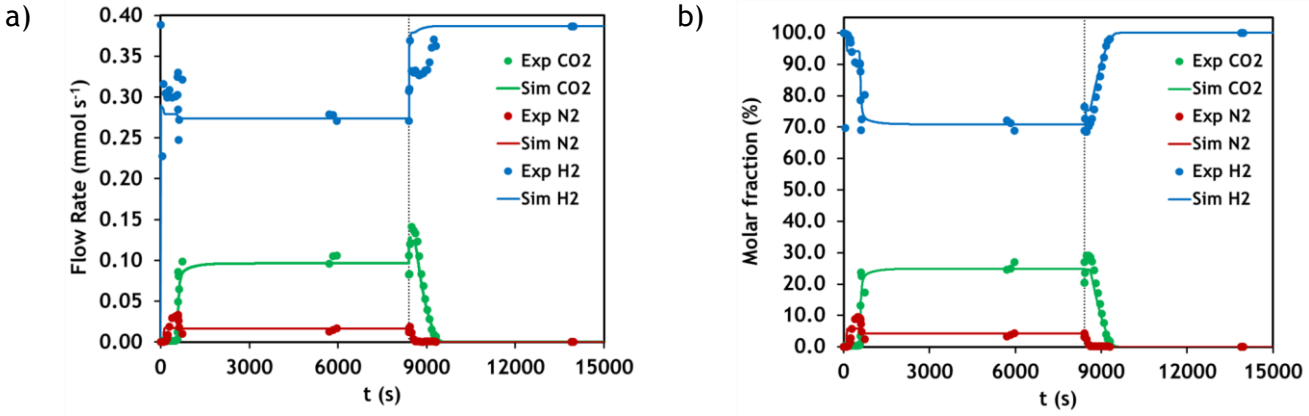

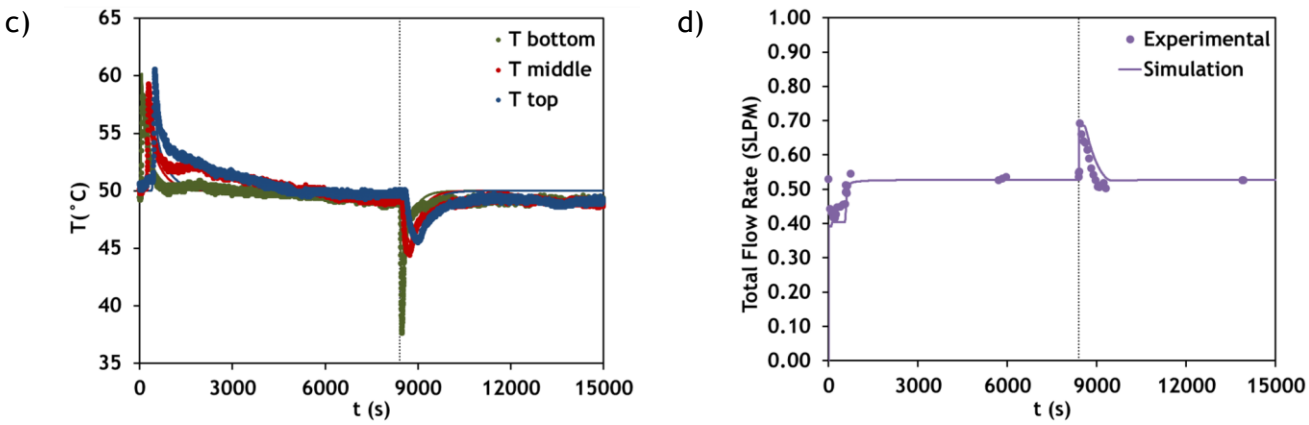

Figure 18 - Breakthrough results of experiment 6 ($H_2/CO_2/N_2$): molar flow rate at the column outlet (a), molar fraction at the column outlet (b), temperatures histories at 8.1 cm (bottom), 19.1 cm (middle) and 30 cm (top) (c) and total flow rate at the column outlet (d). Points correspond to experimental data and lines to simulation results. Vertical line corresponds to the beginning of desorption.

Figure 19 presents the results of the carbon dioxide, carbon monoxide and hydrogen ternary breakthrough curve.

Exp.7 - $H_2/CO_2/CO$

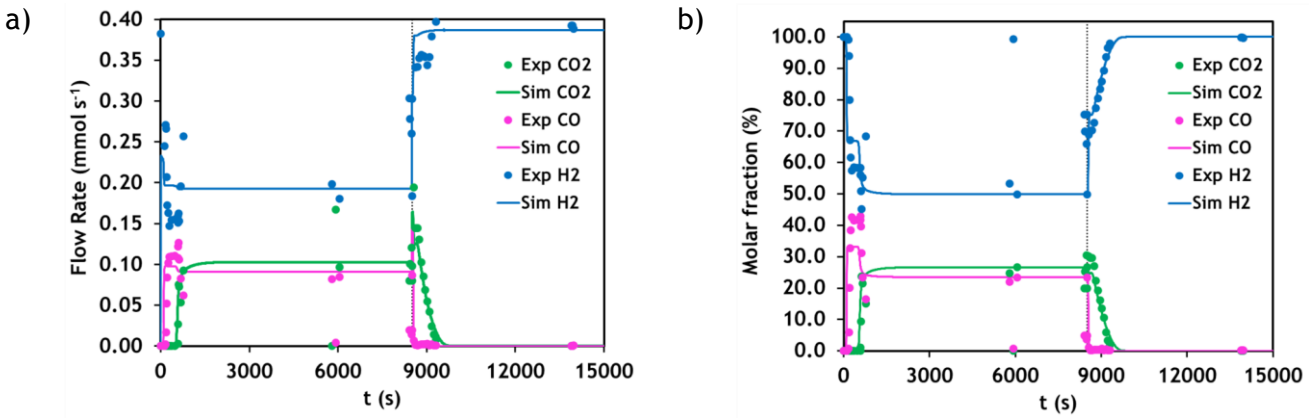

c) d)

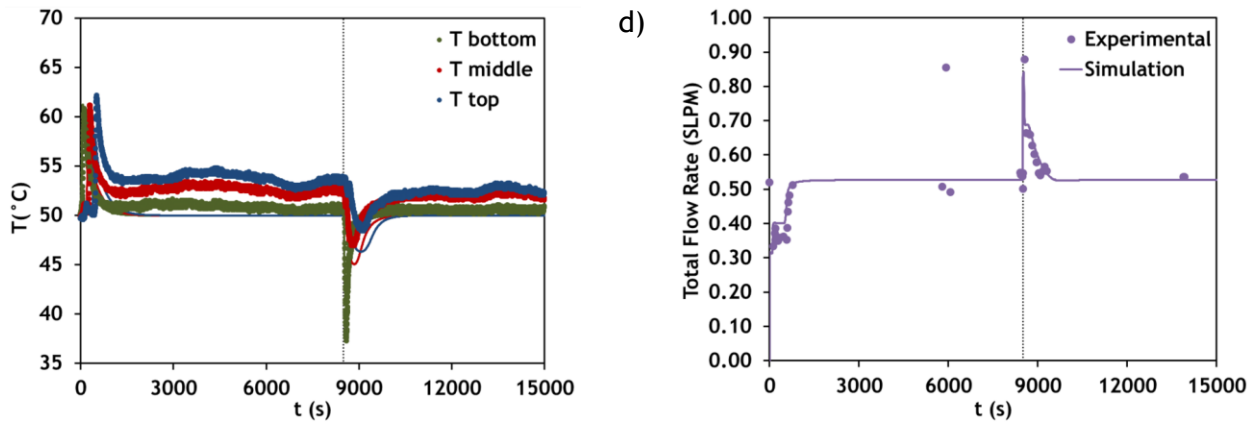

Figure 19 - Breakthrough results of experiment 7 ($H_2/CO_2/CO$): molar flow rate at the column outlet (a), molar fraction at the column outlet (b), temperatures histories at 8.1 cm (bottom), 19.1 cm (middle) and 30 cm (top) (c) and total flow rate at the column outlet (d). Points correspond to experimental data and lines to simulation results. Vertical line corresponds to the beginning of desorption.

The simulations of experiments 5, 6 and 7 represent well the experimental results. Only some differences in the height of the overshoot of methane, nitrogen and carbon monoxide are seen.

Table 7 - Transport parameter values used in the simulation of the breakthrough curve experiments 1 to 7.[a]

Experiment	D_p (m^2 s^{-1})	D_{ax} (m^2 s^{-1})	k_f (m s^{-1})	h_f (W m^{-2} K^{-1})	h_w (W m^{-2} K^{-1})	U (W m^{-2} K^{-1})
Exp.1	CO_2: 8.45×10^{-7} He: 2.22×10^{-6}	8.70×10^{-5}	2.53×10^{-2}	114	48	26
Exp.2	CO_2: 8.53×10^{-7} He: 2.54×10^{-6}	1.50×10^{-4}	3.93×10^{-2}	152	65	31
Exp.3	CO_2: 6.58×10^{-7} CH_4: 4.26×10^{-6} He: 2.28×10^{-6}	9.52×10^{-5}	2.84×10^{-2}	58	18	14
Exp.4	CO_2: 6.58×10^{-7} CH_4: 9.06×10^{-7} He: 2.30×10^{-6}	9.81×10^{-5}	2.85×10^{-2}	63	21	15
Exp.5	CO_2: 8.27×10^{-7} CH_4: 1.18×10^{-6} H_2: 2.13×10^{-6}	4.83×10^{-5}	1.47×10^{-2}	153	63	30
Exp.6	CO_2: 8.37×10^{-7} N_2: 9.41×10^{-7} H_2: 1.86×10^{-6}	3.82×10^{-5}	1.17×10^{-2}	164	69	32

Exp.7	CO_2: 7.72×10^{-7} CO: 9.77×10^{-7} H_2: 2.54×10^{-6}	6.91×10^{-5}	2.08×10^{-2}	128	50	27

[a] Values calculated at feed conditions.

Table 8 - Transport parameter values used in the simulation of the breakthrough curve experiments 8 to 20.[a]

Experiment	D_p ($m^2\ s^{-1}$)	D_{ax} ($m^2\ s^{-1}$)	k_f ($m\ s^{-1}$)	h_f ($W\ m^{-2}\ K^{-1}$)	h_w ($W\ m^{-2}\ K^{-1}$)	U ($W\ m^{-2}\ K^{-1}$)
Exp.8	CO_2: 8.45×10^{-7} He: 2.22×10^{-6}	8.69×10^{-5}	2.53×10^{-2}	111	53	40
Exp.9	CO_2: 8.45×10^{-7} He: 2.22×10^{-6}	8.69×10^{-5}	2.66×10^{-2}	52	30	40
Exp.10	CO: 1.07×10^{-6} He: 2.35×10^{-6}	1.05×10^{-4}	2.47×10^{-2}	178	93	36
Exp.11	CO: 1.08×10^{-6} He: 2.35×10^{-6}	1.05×10^{-4}	2.71×10^{-2}	155	73	33
Exp.12	N_2: 9.69×10^{-7} He: 2.34×10^{-6}	1.03×10^{-5}	2.64×10^{-2}	152	72	32
Exp.13	N_2: 3.54×10^{-7} He: 2.34×10^{-6}	1.03×10^{-5}	2.72×10^{-2}	35	13	10
Exp.14	H_2: 2.06×10^{-6} He: 2.73×10^{-6}	2.31×10^{-4}	4.94×10^{-2}	217	118	39
Exp.15	CH_4: 1.34×10^{-6} He: 2.32×10^{-6}	1.01×10^{-4}	2.57×10^{-2}	156	74	33
Exp.16	CH_4: 1.34×10^{-6} He: 2.32×10^{-6}	1.01×10^{-4}	2.57×10^{-2}	157	74	33
Exp.17	CO_2: 8.09×10^{-7} N_2: 8.57×10^{-7} He: 2.24×10^{-6}	8.93×10^{-5}	2.24×10^{-2}	94	35	22
Exp.18	CO_2: 8.03×10^{-7} N_2: 8.55×10^{-7} He: 2.24×10^{-6}	9.01×10^{-5}	2.71×10^{-2}	97	40	30
Exp.19	CO_2: 8.16×10^{-7} CO: 9.13×10^{-7} He: 2.24×10^{-6}	8.90×10^{-5}	2.47×10^{-2}	98	39	24
Exp.20	CO_2: 7.11×10^{-7} CO: 8.26×10^{-7} He: 2.24×10^{-6}	8.97×10^{-5}	2.56×10^{-2}	50	17	13

[a] Values calculated at feed conditions.

4.3 PSA

Two PSA cycles were studied aiming two different scenarios. In the first case study (PSA 1), hydrogen purification was performed from a mixture containing 30% CO_2 and 70% H_2. In the second case study (PSA 2), a mixture with $H_2/CO_2/CO$ (48, 30 and 22%) was fed to the PSA process in order to obtain two products: a CO_2 enriched stream and a (H_2+CO) product with H_2/CO stoichiometric ratio of approximately 2.3, suitable as feed stream for Fischer-Tropsch process.

The PSA cycle schemes used for each case study are presented in Figure 20.

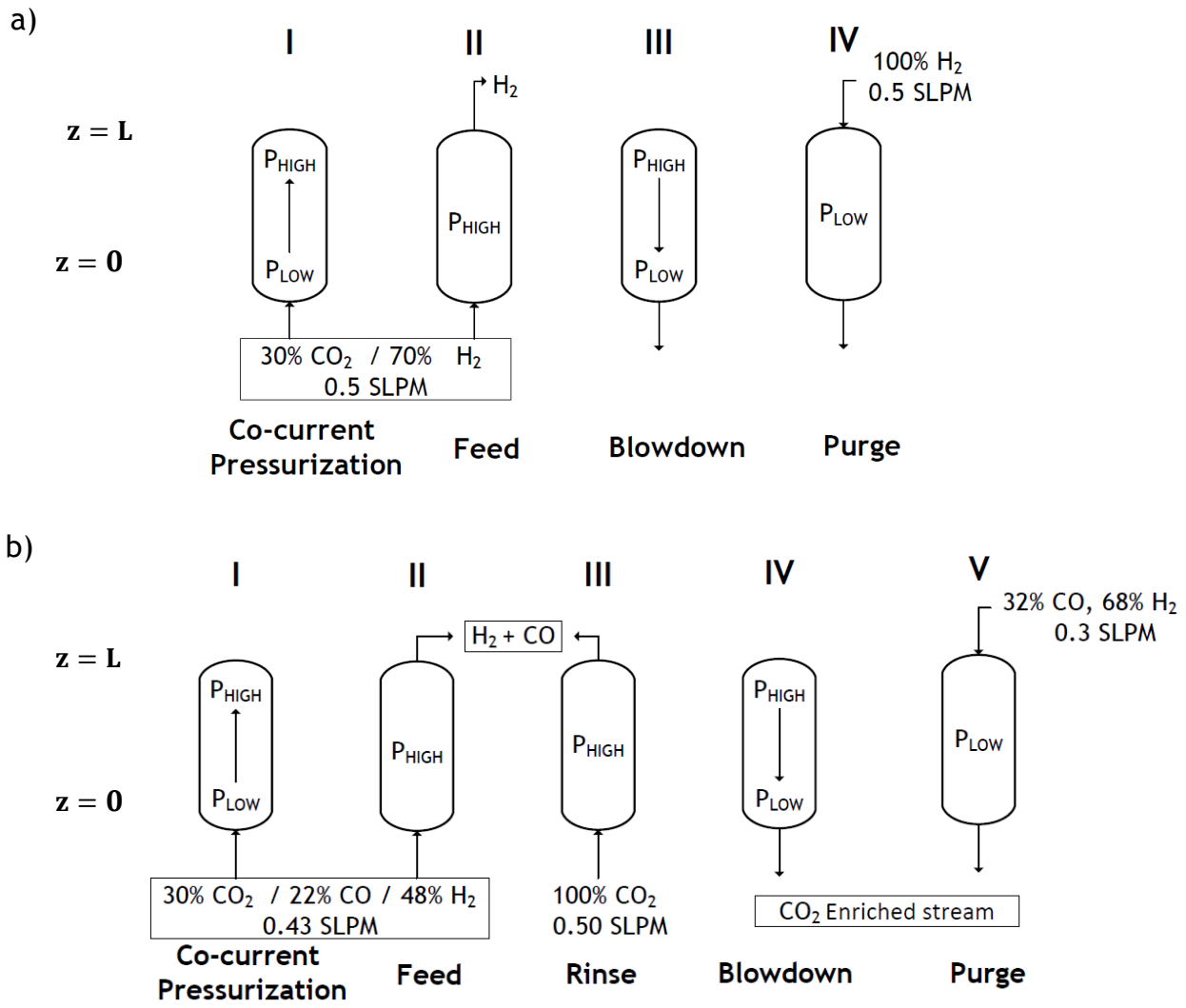

Figure 20 - Cycle sequence used in the PSA 1 (a) and PSA 2 (b) simulations.

The mathematical model presented in section 3.2.4 was applied for the PSA simulations. The boundary conditions used for the simulation of a PSA process are given in Table 3 (section 3.2.5).

The column employed for the fixed-bed breakthrough experiments (described in section 3.2.3) was also used for the PSA experiments. PSA cycles were performed in accordance with the elementary steps showed in Figure 20. PSA 1 cycle started with co-current pressurization followed by feed, blowdown and purge steps. In PSA 2 cycle a rinse step was included after the feed and the others steps were maintained.

At the beginning of each PSA experiments, the column was filled with hydrogen at high pressure (4 bar) and feed temperature. The conditions used in the experiments are presented in Table 9.

Table 9 - Operating conditions used in PSA experiments and simulations.

Temperature (K)	323
P_{high} (bar)	4.0 (feed and rinse steps)
P_{low} (bar)	1.0 (purge step)

Experiment	Q_{feed} (SLPM)	Q_{rinse} (SLPM)	Q_{purge} (SLPM)	t_{feed} (s)	t_{rinse} (s)	t_{blow} (s)	t_{purge} (s)
PSA 1	0.50 30% CO_2 70% H_2	-	0.50 100% H_2	310	-	79	123
PSA 2	0.43 30% CO_2 22%CO 48% H_2	0.50 100% CO_2	0.30 32% CO_2 68% H_2	332	221	94	92

PSA 1 - CO_2/H_2

a)

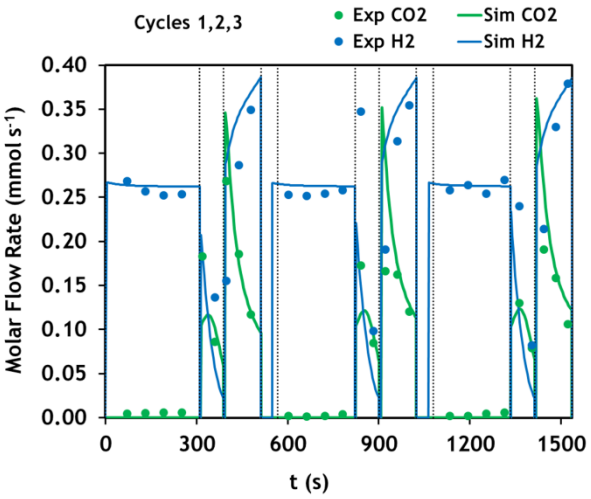

b)

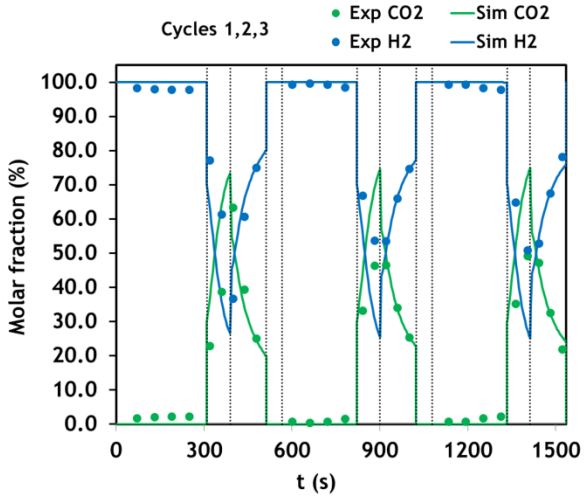

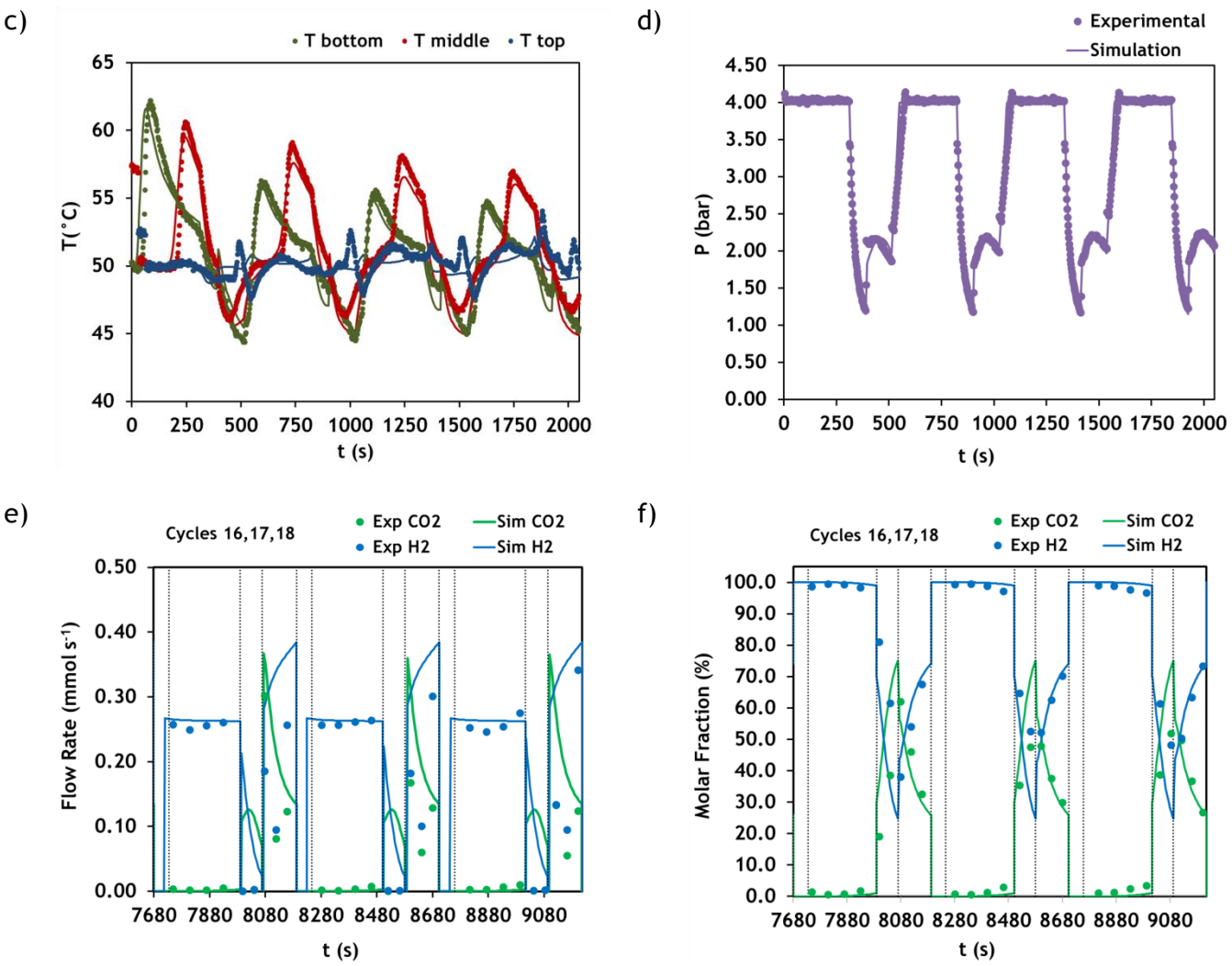

Figure 21 - PSA results of experiment PSA 1 (CO_2/H_2): molar flow rate at the column outlet (a and e) for cycles 1,2,3 and 16,17 and 18, respectively; molar fraction at the column outlet (b and f) for cycles 1,2,3 and 16,17 and 18, respectively; temperatures histories at 8.1 cm (bottom), 19.1 cm (middle) and 30 cm (top) (c) and pressure history (d). Points correspond to experimental data and lines to simulation results. Vertical lines indicate the duration of each step (pressurization, feed, blowdown and purge) along the cycles.

The experimental results obtained for PSA 1 are shown in Figure 21 (molar flow rate for cycles, molar fraction, temperature and pressure). In this experiment, the pressure in the purge step did not reach the desired atmospheric pressure due to an experimental fault (non-opening of a valve). In order to simulate the pressure history correctly, the experimental values were adjusted with an exponential function that was then used in the simulation. The experimental results were generally well described by the mathematical model. Cycles 16,17 and 18 are presented in Figure 21 e) and f) since it is considered that the cyclic steady state (CSS) was achieved by then.

PSA 2 - $CO_2/CO/H_2$

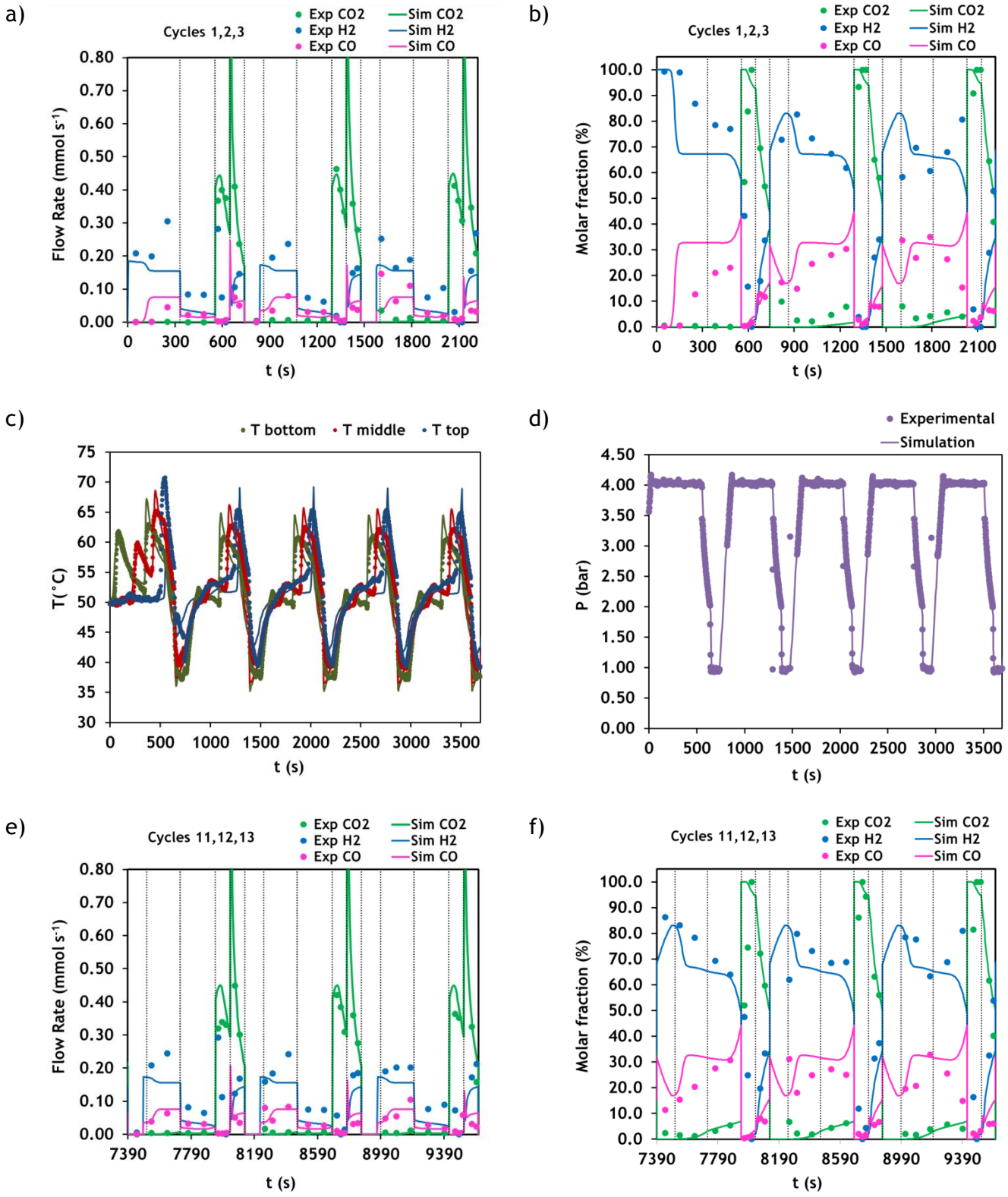

Figure 22 - PSA results of experiment PSA 2 ($CO_2/CO/H_2$): molar flow rate at the column outlet (a and e) for cycles 1,2,3 and 11,12 and 13, respectively; molar fraction at the column outlet (b and f) for cycles 1,2,3 and 11,12 and 13, respectively; temperatures histories at 8.1 cm (bottom), 19.1 cm (middle) and 30 cm (top) (c) and pressure history (d). Points correspond to experimental data and lines to simulation results. Vertical lines indicate the duration of each step (pressurization, feed, rinse, blowdown and purge) along the cycles.

The results of PSA 2 experiment are given in Figure 22. In this case the temperature and pressure histories were well described by the simulation. The molar flow rate and molar fraction present some deviations, especially for CO.

The performance of PSA processes is normally evaluated according to basic parameters of product purity, product recovery and adsorbent productivity.

For hydrogen purification (PSA 1), the purity, recovery and productivity are defined by:

$$\mathrm{H_2\ Purity\ (\%)} = \frac{\int_0^{t_{feed}} C_{H_2}\, u_0|_{z=L} dt}{\sum_{i=1}^{n} \int_0^{t_{feed}} C_i\, u_0|_{z=L} dt} \tag{28}$$

$$\mathrm{H_2\ Recovery\ (\%)} = \frac{\int_0^{t_{feed}} C_{H_2}\, u_0|_{z=L} dt - \int_0^{t_{purge}} C_{H_2}\, u_0|_{z=L} dt}{\int_0^{t_{press}} C_{H_2}\, u_0|_{z=0} dt + \int_0^{t_{feed}} C_{H_2}\, u_0|_{z=0} dt} \tag{29}$$

$$\mathrm{H_2\ Productivity\ (mol\ kg^{-1}\ h^{-1})} = \frac{\int_0^{t_{feed}} C_{H_2}\, u_0|_{z=L} dt - \int_0^{t_{purge}} C_{H_2}\, u_0|_{z=L} dt}{t_{cycle} \times mass\ dry\ adsorbent} \tag{30}$$

$$\mathrm{CO_2\ Purity\ (\%)} = \frac{\int_0^{blow} C_{CO_2}\, u_0|_{z=L} dt + \int_0^{purge} C_{CO_2}\, u_0|_{z=L} dt}{\sum_{i=1}^{n} [\int_0^{t_{blow}} C_i\, u_0|_{z=L} dt + \int_0^{t_{purge}} C_i\, u_0|_{z=L} dt\,]} \tag{31}$$

$$\mathrm{CO_2\ Recovery\ (\%)} = \frac{\int_0^{t_{blow}} C_{CO_2}\, u_0|_{z=0} dt + \int_0^{t_{purge}} C_{CO_2}\, u_0|_{z=0} dt}{\int_0^{t_{press}} C_{CO_2}\, u_0|_{z=0} dt + \int_0^{t_{feed}} C_{CO_2}\, u_0|_{z=0} dt} \tag{32}$$

$$\mathrm{CO_2\ Productivity\ (mol\ kg^{-1}\ h^{-1})} = \frac{\int_0^{t_{blow}} C_{CO_2}\, u_0|_{z=0} dt + \int_0^{t_{purge}} C_{CO_2}\, u_0|_{z=0}\, dt}{t_{cycle} \times mass\ dry\ adsorbent} \tag{33}$$

In the case of PSA 2, in which the objective is the syngas composition adjustment for use in a Fischer-Tropsch reactor, the H_2/CO ratio and the inert fraction in the light product is also important. The performance parameters for this case study are given by:

$$\frac{H_2}{CO} = \frac{\int_0^{t_{feed}} C_{H_2}\, u_0|_{z=L} + \int_0^{t_{rinse}} C_{H_2}\, u_0|_{z=L}}{\int_0^{t_{feed}} C_{CO}\, u_0|_{z=L} + \int_0^{t_{rinse}} C_{CO}\, u_0|_{z=L}} \tag{34}$$

H_2 Recovery (%)

$$= \frac{\int_0^{t_{feed}} C_{H_2}\, u_0|_{z=L} dt + \int_0^{t_{rinse}} C_{H_2}\, u_0|_{z=L} dt - \int_0^{t_{purge}} C_{H_2}\, u_0|_{z=L} dt}{\int_0^{t_{press}} C_{H_2}\, u_0|_{z=0} dt + \int_0^{t_{feed}} C_{H_2}\, u_0|_{z=0} dt} \tag{35}$$

$$CO_2 \text{ Purity (\%)} = \frac{\int_0^{blow} C_{CO_2}\, u_0|_{z=0} dt + \int_0^{purge} C_{CO_2}\, u_0|_{z=0} dt}{\sum_{i=1}^{n} [\int_0^{t_{blow}} C_i\, u_0|_{z=0} dt + \int_0^{t_{purge}} C_i\, u_0|_{z=0} dt]} \tag{36}$$

CO_2 Recovery (%)

$$= \frac{\int_0^{t_{blow}} C_{CO_2}\, u_0|_{z=0} dt + \int_0^{t_{purge}} C_{CO_2}\, u_0|_{z=0} dt - \int_0^{t_{rinse}} C_{CO_2}\, u_0|_{z=0} dt}{\int_0^{t_{press}} C_{CO_2}\, u_0|_{z=0} dt + \int_0^{t_{feed}} C_{CO_2}\, u_0|_{z=0} dt} \tag{37}$$

H_2 + CO Productivity ($mol_{H_2+CO}\ kg^{-1}\ h^{-1}$)

$$= \frac{\int_0^{t_{feed}} C_{H_2+CO}\, u_0|_{z=L} dt + \int_0^{t_{rinse}} C_{H_2+CO}\, u_0|_{z=L} dt - \int_0^{t_{purge}} C_{H_2+CO}\, u_0|_{z=L} dt}{t_{cycle} \times mass\ dry\ adsorbent} \tag{38}$$

CO_2 Productivity ($mol_{CO_2}\ kg^{-1}\ h^{-1}$)

$$= \frac{\int_0^{t_{blow}} C_{CO_2}\, u_0|_{z=0} dt + \int_0^{t_{purge}} C_{CO_2}\, u_0|_{z=0} dt - \int_0^{t_{rinse}} C_{CO_2}\, u_0|_{z=0} dt}{t_{cycle} \times mass\ dry\ adsorbent} \tag{39}$$

The performance parameters for each experiment calculated by simulation are presented in Table 10.

Table 10 – Process performance obtained by simulation for the two PSA experiments.

PSA 1	
Purity (%)	99.8% H_2 ; 40.0% CO_2
Recovery (%)	35.6% H_2 ; 100% CO_2
Productivity (mol kg^{-1} h^{-1})	4.7 mol_{H2} kg^{-1} h^{-1}
PSA 2	
H_2/CO	2.37
inert gases in light product (%)	1.56%
Purity (%)	83.8% CO_2
Recovery (%)	4.5% H_2 ; 17.1% CO_2
Productivity (mol kg^{-1} h^{-1})	3.15 mol_{CO2} kg^{-1} h^{-1} 5.32 mol_{H2+CO} kg^{-1} h^{-1}

5 Conclusions

In this work the MOF MIL-125(Ti)_NH_2 was studied for gas mixtures separation. The adsorption equilibrium isotherms of CO_2, CH_4, CO, N_2 and H_2 were measured using a gravimetric method by means of a Rubotherm micro-balance. The results presented the following order of affinity: CO_2 > CH_4 > CO > N_2 > H_2 from the most adsorbed to the less adsorbed. The experimental data was fitted using the Langmuir model. Single, binary and ternary breakthrough curves were performed in a fixed-bed set-up. The modeling of the dynamic adsorption in a fixed-bed was done using a model developed by Da Silva. (1999) using the multicomponent extension of the Langmuir isotherm. The mathematical model was solved in gProms (version 3.5.3, 2012, PSE Enterprise, UK). The results showed that the multicomponent adsorption of mixtures with hydrogen isn't well described considering competition between hydrogen and other adsorbates. The hypothesis that H_2 adsorbs without competition and that the other compounds compete with each other was made. With this hypotheses most of the experimental data was successfully described by the model. This possibility may be due to the small size of the hydrogen molecules that therefore may adsorb in sites where competition with other components does not occur.

PSA experiments were performed focusing on two main purposes: hydrogen purification (PSA 1) and syngas composition adjustment (H_2/CO≈2.3) and co-production of a CO_2 enriched stream (PSA 2). For the first case study (PSA 1) a cycle with four steps, co-current pressurization, feed, blowdown, and purge was designed. Starting with a feed stream of 70%/30% of H_2/CO_2, a hydrogen product with 99.8% H_2 and a recovery of 35.6% was obtained. For the second case study a cycle with five steps, co-current pressurization, feed, rinse, blowdown and purge, was designed. Using a feed stream with 30% CO_2, 22% CO and 48% H_2, a light product with a H_2/CO ratio of 2.37 and 1.56% of CO_2 was obtained. The other product of the process was a CO_2 enriched stream with 83.8%. A CO_2 recovery of 17.1% was attained. The feasibility of using this adsorbent in PSA processes for syngas purification was shown.

Nevertheless, it is important to mention that the experiments were designed taking into consideration the limitations of the experimental set-up, for example the impossibility of using counter-current pressurization. Therefore the obtained process performance does not represent the ideal cycle for each of the case-studies.

For future work, design of an industrial scale process and its optimization should be performed in order to improve the productivity and recovery of the PSA cycles. Some parameters should be taken in account: cycle design, step times, feed temperature and pressures. Furthermore, other applications can be assessed such as separation of hydrocarbon

mixtures, water adsorption, syngas adjustment for methanol production and carbon dioxide capture.

In conclusion, the balance of the work is highly positive.

References

Bancon, S. and Bec, R. L. *Syngas purification process*. U.S. Patent 462,514, 2007.

Da Silva, F. A. 1999. *Cyclic Adsorption Processes: Application to Propane/Propylene Separation*. Tese de Doutoramento, FEUP.

Do, D. D. *Adsorption Analysis: Equilibria and Kinetics*. Imperial College Press, Department of Chemical Engineering, University of Queensland, Australia, 1998.

Domine, D. and Montgareuil, P. G. D. *Process for separating a binary gaseous mixture by adsorption*. FR Patent 1,223,261, 1964a.

Domine, D. and Montgareuil, P. G. D. *Process for separating a binary gaseous mixture by adsorption*. U.S. Patent 3,155,468, 1964b.

Farrusseng, D. *Metal-Organic Frameworks: Applications from Catalysis to Gas Storage*. Wiley-VCH, University Lyon, France, 2011.

Férey, G. *Hybrid porous solids: past, present, future*. Chemical Society Reviews. Volume 37, 191-214, 2008.

Ferreira, A. F. P., Ribeiro, A. M., Kulaç, S. and Rodrigues, A. E. *Methane purification by adsorptive processes on MIL-53(Al)*. Chemical Engineering Science. 2014.

Ferreira, A. F. P., Santos, J. C., Plaza, M. G., Lamia, N., Loureiro, J. M. and Rodrigues, A. E. *Suitability of Cu-BTC extrudates for propane-propylene separation by adsorption processes*. Chemical Engineering Journal. 167, 1-12, 2011.

Finlayson, D. and Sharp, A. J. *Improvements in or relating to the treatment of gaseous mixtures for the purpose of separating them into their components or enriching them with respect to one or more of their components*. G.B. Patent 365,092, 1932.

Fuderer, A. and Rudelstorfer, E. *Selective Adsorption Process*. U. S. Patent 3,986,849, 1976.

Higman, C. and Burgt., M. v. d. *Gasification*. Elsevier Science, (2003).

Kim, S.-N., Kim, J., Kim, H.-Y., Cho, H.-Y. and Ahn, W.-S. *Adsorption/catalytic properties of MIL-125 and NH2-MIL-125*. Catalysis Today. 204, 85-93, 2013.

Kitagawa, S., Kitaura, R. and Noro, S. i. *Functional porous coordination polymers*. Angewandte Chemie International Edition. 43, 2334-2375, 2004.

Lee, Y.-R., Kim, J. and Ahn, W.-S. *Synthesis of metal-organic frameworks: A mini review*. Korean Journal of Chemical Engineering. 30, 1667-1680, 2013.

Li, J.-R., Sculley, J. and Zhou, H.-C. *Metal-Organic Frameworks for Separations*. Chemical Reviews. 112, 869-932, 2011.

Long, J. R., Zhou, H.-C. and Yaghi, O. M. *Introduction to Metal-Organic Frameworks*. Chemical Reviews. 112, 673-674, 2012.

Maurer, R. T. *Methane purification by pressure swing adsorption*. U.S. Patent 462,514, 1991.

Monereau, C. and Carriere, C. *Production of hydrogen from a reforming gas and simultaneous capture of CO_2 co-product*. U.S. Patent 130,541, 2011.

Nitta, T., Shigetomi, T., Kurooka, M. and Katayama, T. *An Adsorption Isotherm of Multi-Site Occupancy Model for Homogeneous Surface*. J. Chem. Eng. Japan. 17, 1984.

Norbert, S. and Shyam, B. *Synthesis of Metal—Organic Frameworks (MOFs): Routes to Various MOF Topologies, Morphologies, and Composites*. ChemInform. 43, 2012.

Prausnitz, J. M., O'Connell, J. P. and Poling, B. E. *Properties of Gases and Liquids*. McGRAW-HILL, United States of America, 2001.

Rostrup-Nielsen, J. and Christiansen, L. J. *Concepts in Syngas Manufacture*. Imperial College Press, London, 2011.

Rowsell, J. L. C. and Yaghi, O. M. *Microporous and Mesoporous Materials*. Microporous and Mesoporous Materials. 73, 3-14, 2004.

Ruthven, D. M. *Principles of Adsorption and Adsorption Processes*. John Wiley & Sons, University of New Brunswick, Fredericton, 1984.

Schell, J., Casas, N., Blom, R., Spjelkavik, A., Andersen, A., Cavka, J. and Mazzotti, M. *MCM-41, MOF and UiO-67/MCM-41 adsorbents for pre-combustion CO_2 capture by PSA: adsorption equilibria*. Adsorption. 18, 213-227, 2012.

Seader, J. D., Henley, E. J. and Keith Roper, D. *Separation Process Principles - Chemical and Biochemical Operations*. John Wiley & Sons, Inc., 2011.

Skarstrom, C. W. *Method and apparatus for fractionating gaseous mixtures by adsorption*. U.S. Patent 2,944,627, 1960.

Szostac, R. *Molecular Sieves: Principles of Synthesis and Identification*. Blackie Academic & Professional, Thomson Science, Germany, 1998.

Vaesen, S., Guillerm, V., Yang, Q., Wiersum, A. D., Marszalek, B., Gil, B., Vimont, A., Daturi, M., Devic, T., Llewellyn, P. L., Serre, C., Maurin, G. and De Weireld, G. *A robust amino-functionalized titanium(iv) based MOF for improved separation of acid gases*. Chemical Communications. 49, 10082-10084, 2013.

Appendix 1 - Helium pycnometries

Two helium pycnometries to the systems were performed. One for the system composed by the basket (where the sample is placed), the permanent magnet and the suspension shaft (where is the basket handing), and the other for the same system but also with the activated adsorbent. They are represented respectively in Figure A1.1 and Figure A1.2.

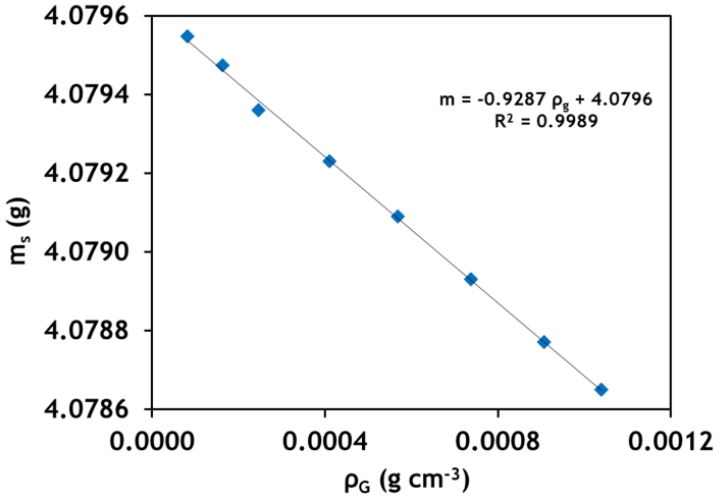

Figure A1.1 - Helium pycnometry of system with basket permanent magnet and suspension shaft.

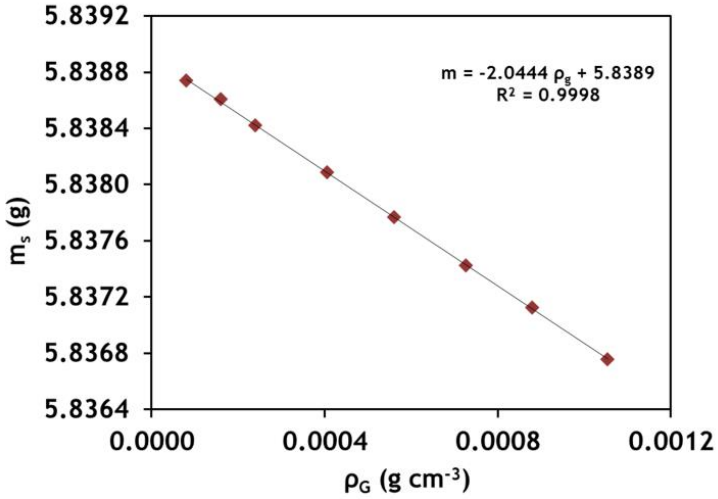

Figure A1.2 - Helium pycnometry in system with basket, permanent magnet, suspension shaft and adsorbent.

Appendix 2 – Correlations

In order to simulate the breakthrough curves in gProms using the proposed model, it is necessary to define some parameters. These parameters are related with adsorbent particle, adsorption column and experimental conditions.

The particle specific area (a_{pM}) is given by:

$$a_{pM} = \frac{k_{sM} + 1}{R_p} \tag{A2. 1}$$

where k_{sM} is geometrical factor (0 to slab, 1 to cylinder and 2 to sphere) and R_p is the particle radius.

The bulk density (ρ_b) can be calculated by:

$$\rho_b = \frac{1 - \varepsilon}{\rho_{ap}} \tag{A2. 2}$$

where ε is the bulk porosity and ρ_{ap} is the apparent density.

The inlet concentration is based on experimental conditions:

$$C_{inlet} = \frac{P}{R_g T} \tag{A2. 3}$$

where P and T are the pressure and temperature of the system and R_g is the ideal gas constant.

The feed flow (Q_{feed}) is determined by:

$$Q_{feed} = u_{0\,inlet} \times A_{bed} \tag{A2. 4}$$

where $u_{0\,inlet}$ is superficial velocity and A_{bed} is the bed area. This area is based on the column diameter (D_w):

$$A_{bed} = \pi \times \left(\frac{D_w}{2}\right)^2 \tag{A2. 5}$$

Reynolds number (Re) represents the ratio between the inertial and viscous forces and it is given by:

$$Re = \frac{\rho u_0 d_p}{\mu} \quad \text{(A2. 6)}$$

where ρ is the fluid density, u_0 is the superficial velocity, d_p is the particle diameter and μ is the fluid viscosity.

The viscosity of pure gas, μ_i, can be calculated by (Prausnitz *et al.*, 2001):

$$\mu_i = 2{,}669 \times 10^{-6} \frac{(M_i T_g)^{\frac{1}{2}}}{\sigma^2 \Omega_{\mu,i}} \quad \text{(A2. 7)}$$

where M_i is the molecular weight of component i, T_g is the gas phase temperature, σ is the collision diameter and $\Omega_{\mu,i}$ represents the collision integral, that is calculated by (Prausnitz *et al.*, 2001):

$$\Omega_D = \frac{A_1}{\omega^{A_5}} + \frac{A_2}{\exp(A_6\omega)} + \frac{A_3}{\exp(A_7\omega)} + \frac{A_4}{\exp(A_8\omega)} \quad \text{(A2. 8)}$$

where A_1 to A_8 are empirical constants and ω is defined as:

$$\omega = \frac{kT_g}{\varepsilon_i} \quad \text{(A2. 9)}$$

where k is the Boltzman constant, T_g is the gas phase temperature and ε_i is the energy parameter for interaction between molecules of component i. The constants used for each compound in the equations presented before are shown in Table A2.1:

Table A2.1 - Molecular weight and Lennard-Jones parameters.

Compound	M_i (g mol^{-1})	**σ** (A)	**ε_i/k** (K)
He	4.003	2.576	10.2
CH_4	16.043	3.780	154
CO	28.010	3.590	110
CO_2	44.010	3.996	190
H_2	2.016	2.915	38
N_2	28.014	3.667	99.8

The viscosity of the mixture, μ, is determined by:

$$\mu = \sum_{i=1}^{n} \frac{y_i \mu_i}{\sum_{j=1}^{n} y_i \Phi_{ij}} \quad \text{(A2. 10)}$$

where y_i is a molar fraction of component i, μ_i is the viscosity of pure component i and Φ_{ij} is calculated by:

$$\Phi_{ij} = \frac{\left[1 + \left(\frac{\mu_i}{\mu_j}\right)^{\frac{1}{2}} \left(\frac{M_j}{M_i}\right)^{\frac{1}{4}}\right]^2}{\left[8\left(1 + \frac{M_i}{M_j}\right)\right]^{\frac{1}{2}}} \quad \text{(A2. 11)}$$

M_{ij} is the molecular weight of the mixture between component i and j and it is given by:

$$M_{ij} = 2\left[\frac{1}{M_i} + \frac{1}{M_j}\right]^{-1} \quad \text{(A2. 12)}$$

Schmidt number (Sc) is defined as the ratio of viscosity and mass diffusivity and it is calculated by:

$$Sc = \frac{\mu}{\rho D_m} \quad \text{(A2. 13)}$$

where D_m is the molecular diffusivity.

The rules to obtain the interaction value σ_{ij} from σ_i and σ_j and ε_{ij} from ε_i and ε_j are:

$$\sigma_{ij} = \frac{\sigma_i + \sigma_j}{2} \quad \text{(A2. 14)}$$

$$\varepsilon_{ij} = \sqrt{\varepsilon_i \varepsilon_j} \quad \text{(A2. 15)}$$

Prandtl number (Pr) represents the ratio of the momentum diffusivity and thermal diffusivity and it is given by:

$$Pr = \frac{\hat{C}_p \mu}{k_g} \quad \text{(A2. 16)}$$

where $\hat{C}_p$ is the heat capacity at constant pressure (per mass unit) and k_g is the thermal conductivity. The heat capacity at constant pressure of pure component, $C_{p,i}$, can be calculated by (Prausnitz *et al.*, 2001):

$$\frac{C_{p,i}}{R_g} = a_0 + a_1 T_g + a_2 T_g^2 + a_3 T_g^3 + a_4 T_g^4 \quad \text{(A2. 17)}$$

where a_0 to a_4 are parameters of the polynomial equation. The constants a_0 to a_4 used for each compound in the equations presented before are shown in Table A2.2:

Table A2.2 - Parameters of the polynomial equation.

Compound	a_0	a_1	a_2	a_3	a_4
He	2.5	0	0	0	0
CH_4	4.568	-8.98×10^{-3}	3.63×10^{-5}	-3.41×10^{-8}	1.09×10^{-11}
CO	3.912	-3.91×10^{-3}	1.18×10^{-5}	-1.30×10^{-8}	5.15×10^{-12}
CO_2	3.259	1.36×10^{-3}	1.50×10^{-5}	-2.37×10^{-8}	1.06×10^{-11}
H_2	2.883	3.68×10^{-3}	-7.72×10^{-6}	6.92×10^{-9}	-2.13×10^{-12}
N_2	3.539	-2.61×10^{-3}	7.00×10^{-8}	1.57×10^{-9}	-9.90×10^{-12}

The heat capacity of the mixture, C_p, can be calculated through knowledge of the pure components by (Prausnitz *et al.*, 2001):

$$C_p = \sum_{i=1}^{n} y_i C_{p,i} \quad \text{(A2. 18)}$$

The heat capacity at constant pressure (per mass unit) can be calculated by (Prausnitz *et al.*, 2001):

$$\widehat{C_p} = \frac{C_p}{\sum_{i=1}^{n} y_i M_i} \quad \text{(A2. 19)}$$

The heat capacity at constant volume, C_v, is calculated by (Prausnitz *et al.*, 2001):

$$C_v = C_p - R_g \tag{A2. 20}$$

The thermal conductivity of pure gas, $k_{g,i}$, can be calculated from (Prausnitz *et al.*, 2001):

$$k_{g,i} = \left(\widehat{C_{p,i}} + \frac{5}{4}\frac{R_g}{M_i}\right)\mu_i \tag{A2. 21}$$

For the mixture, the thermal conductivity, k_g, is calculated from (Prausnitz *et al.*, 2001):

$$k_g = \sum_{i=1}^{n} \frac{y_i k_{g,i}}{\sum_{j=1}^{n} y_j \Phi_{ij}} \tag{A2. 22}$$

The Sherwood number (Sh) is used in mass-transfer operation and it represents the ratio of convective and diffusive mass transport. It is calculated by:

$$Sh = \frac{k_{f,i} d_p}{D_m} \tag{A2. 23}$$

where $k_{f,i}$ is the film mass transfer coefficient of component i.

The Nusselt number (Nu) represents the ratio between convective and conductive heat transfer and it is given by:

$$Nu = \frac{h_f d_p}{k_g} \tag{A2. 24}$$

where h_f is the film heat transfer coefficient between the gas and particle.

Appendix 3 – Calibrations

1. Mass Flow Controllers Calibration

The calibration of the three mass flow controllers of the fixed bed set-up (MFC 1, MFC 2 and MFC 3) was carried out for He, CO_2, N_2, CH_4 and H_2. For each MFC and each gas, gas flow rate set-points were fixed and were measured with a bubble flow meter (BFM). The results obtained are represented in the figures below (Figure A3.1 to Figure A3.5).

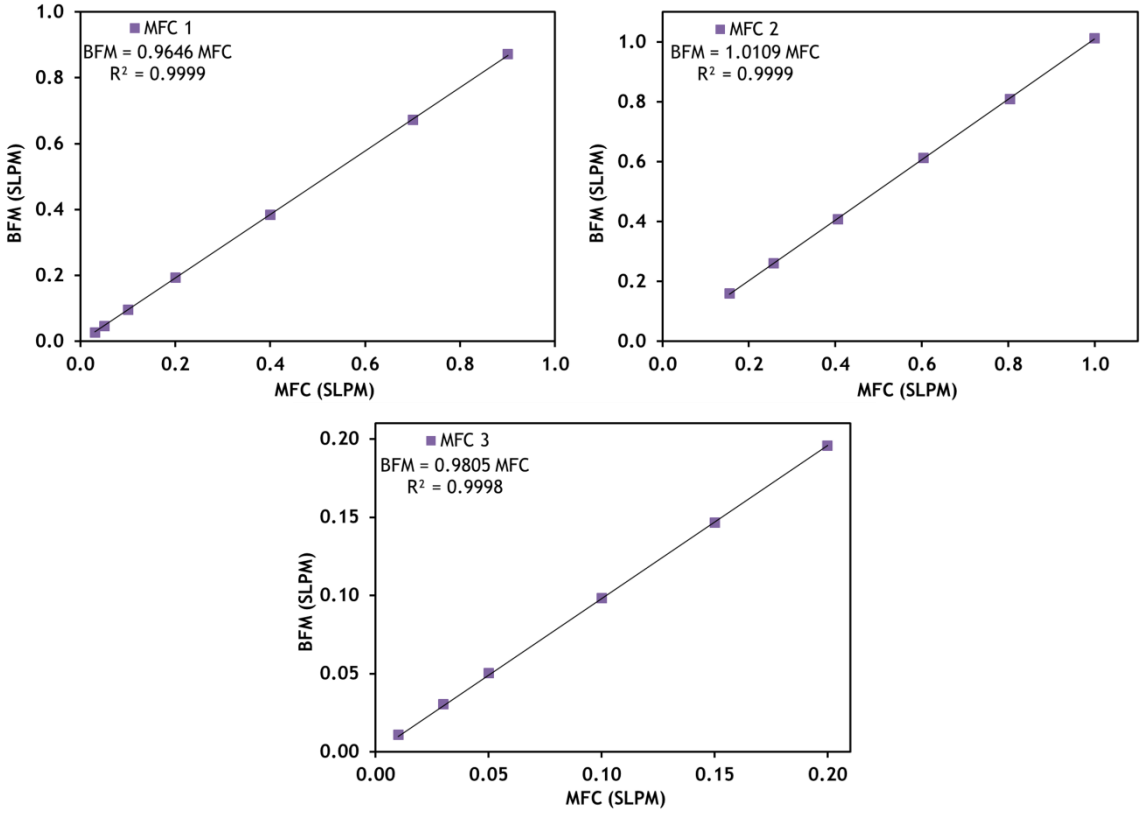

Figure A3.1 - Mass flow controllers calibration (MFC 1, MFC 2 and MFC 3) for helium. Points correspond to experimental data and line to adjusted curve.

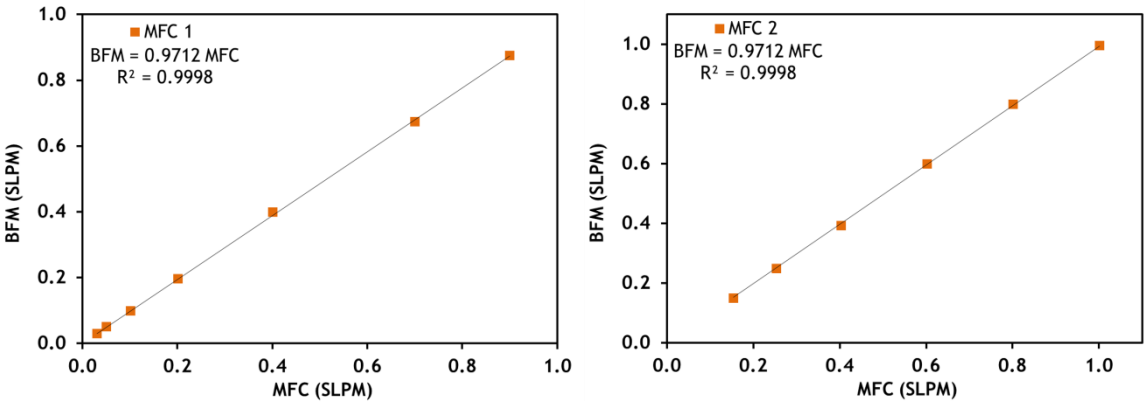

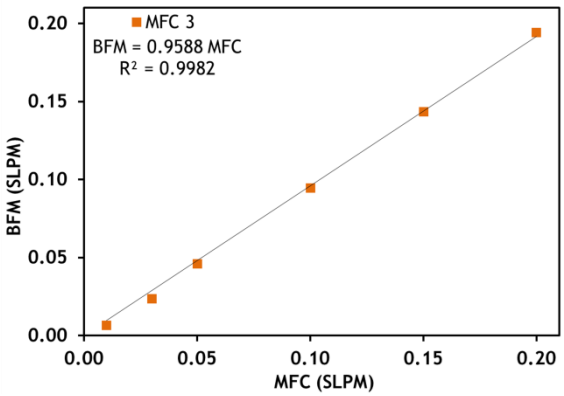

Figure A3.2 - Mass flow controllers calibration (MFC 1, MFC 2 and MFC 3) for carbon dioxide. Points correspond to experimental data and line to adjusted curve.

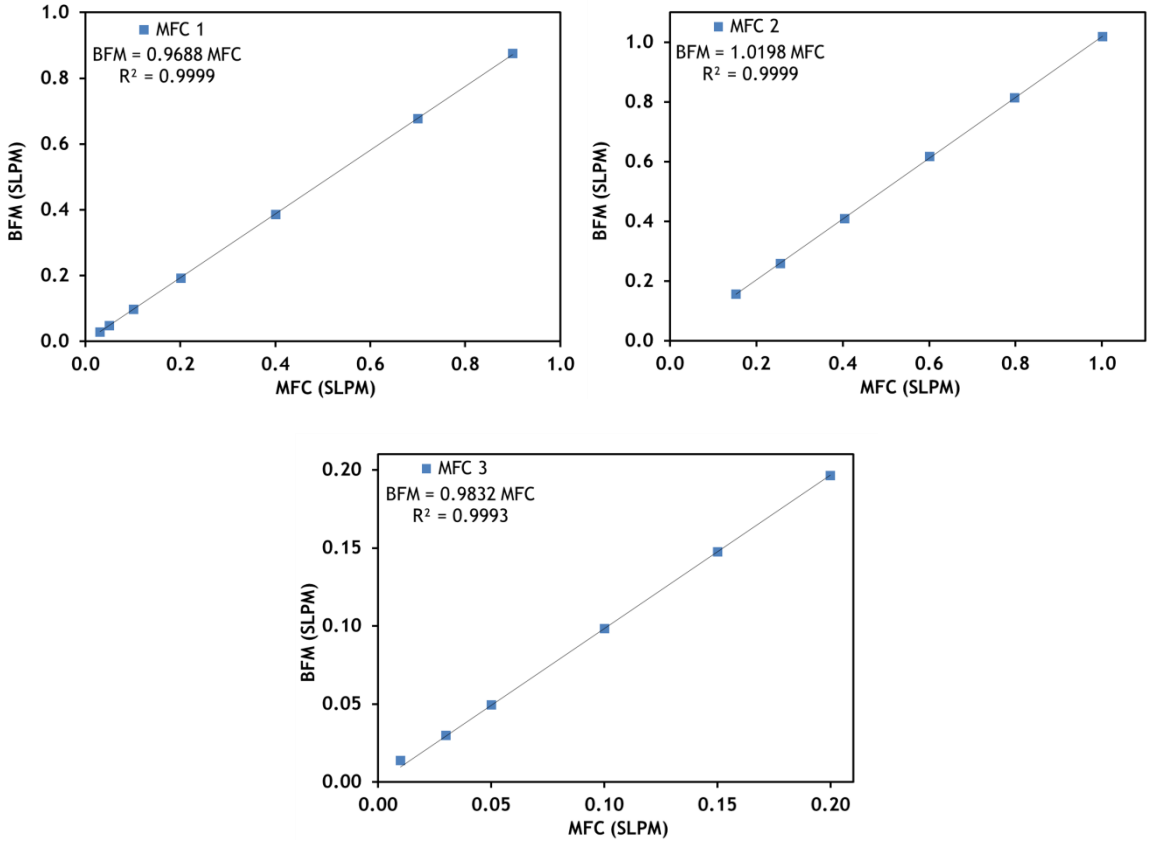

Figure A3.3 - Mass flow controllers calibration (MFC 1, MFC 2 and MFC 3) for nitrogen. Points correspond to experimental data and line to adjusted curve.

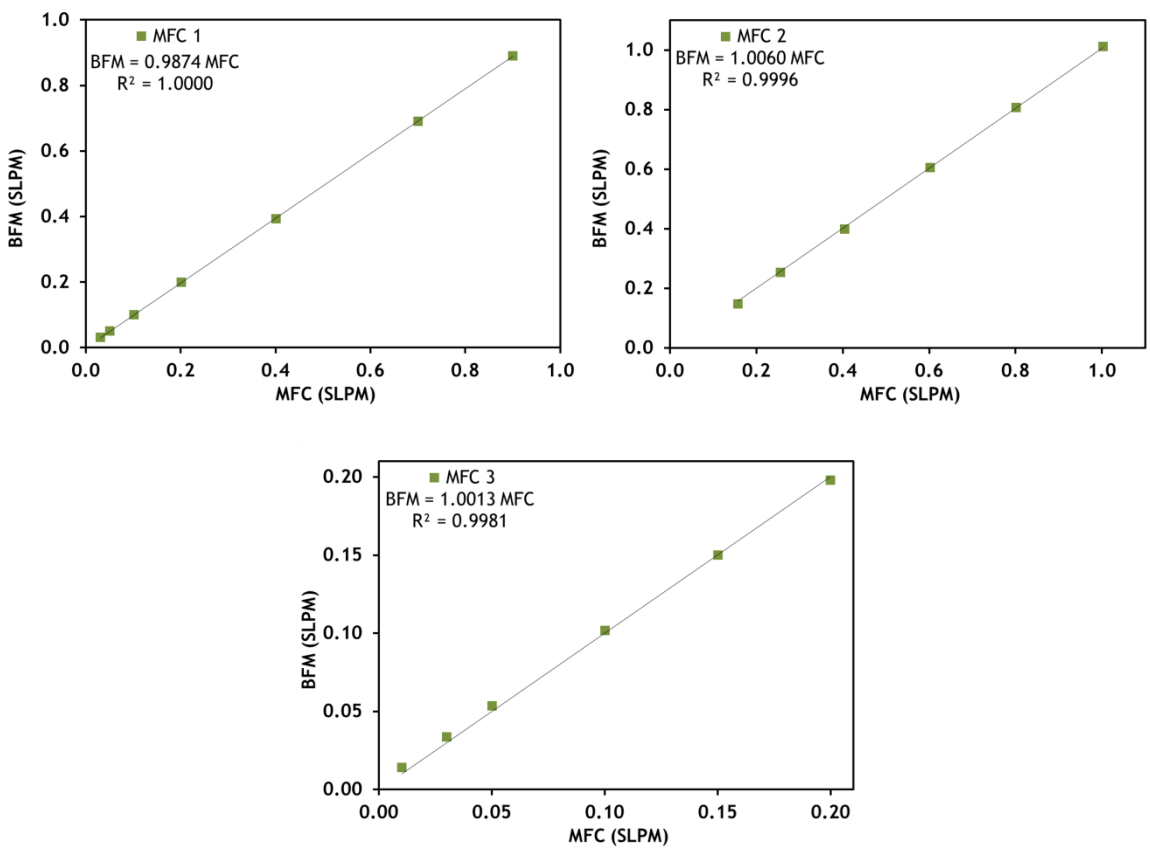

Figure A3.4 - Mass flow controllers calibration (MFC 1, MFC 2 and MFC 3) for methane. Points correspond to experimental data and line to adjusted curve.

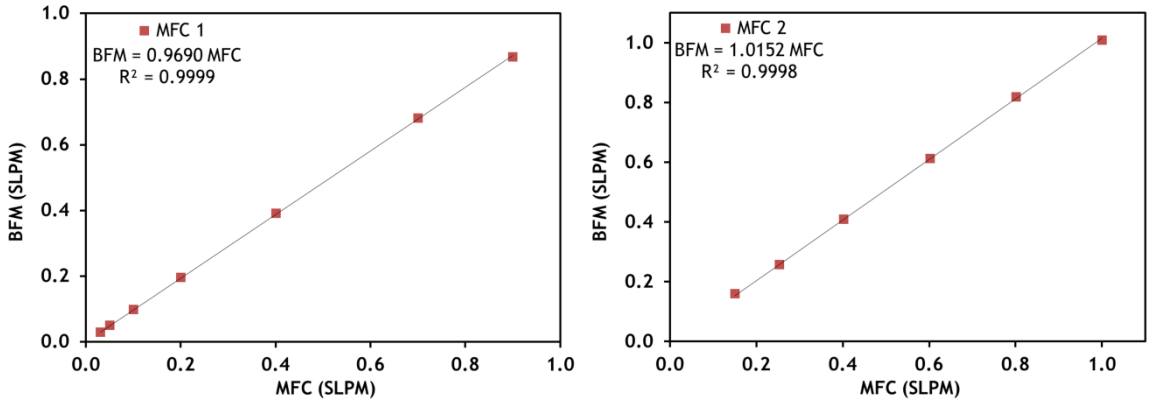

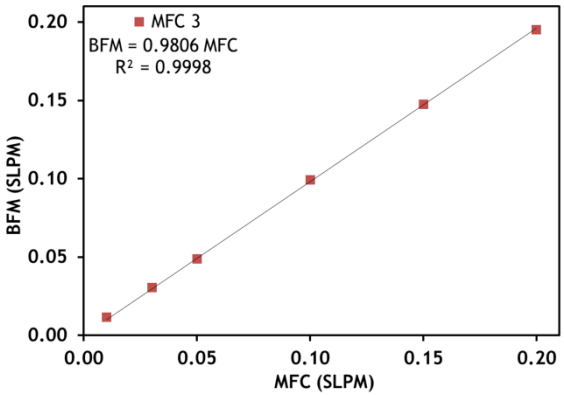

Figure A3.5 - Mass flow controllers calibration (MFC 1, MFC 2 and MFC 3) for hydrogen. Points correspond to experimental data and line to adjusted curve.

2. Chromatograph calibration

The calibration of the chromatograph was performed beforehand with the pure five gases, CO_2, N_2, CH_4, H_2 and CO. The analysis system, composed by 16 loops, is able to store up to 15 samples. Each loop was calibrated for each gas as function of the gas molar fraction. The loops were filled with the desired molar fraction (balanced with He) and then each sample was analyzed by the detector of the gas chromatograph and the peak area measured. The results are shown in the graphics below (Figure A3.6 to Figure A3.9).

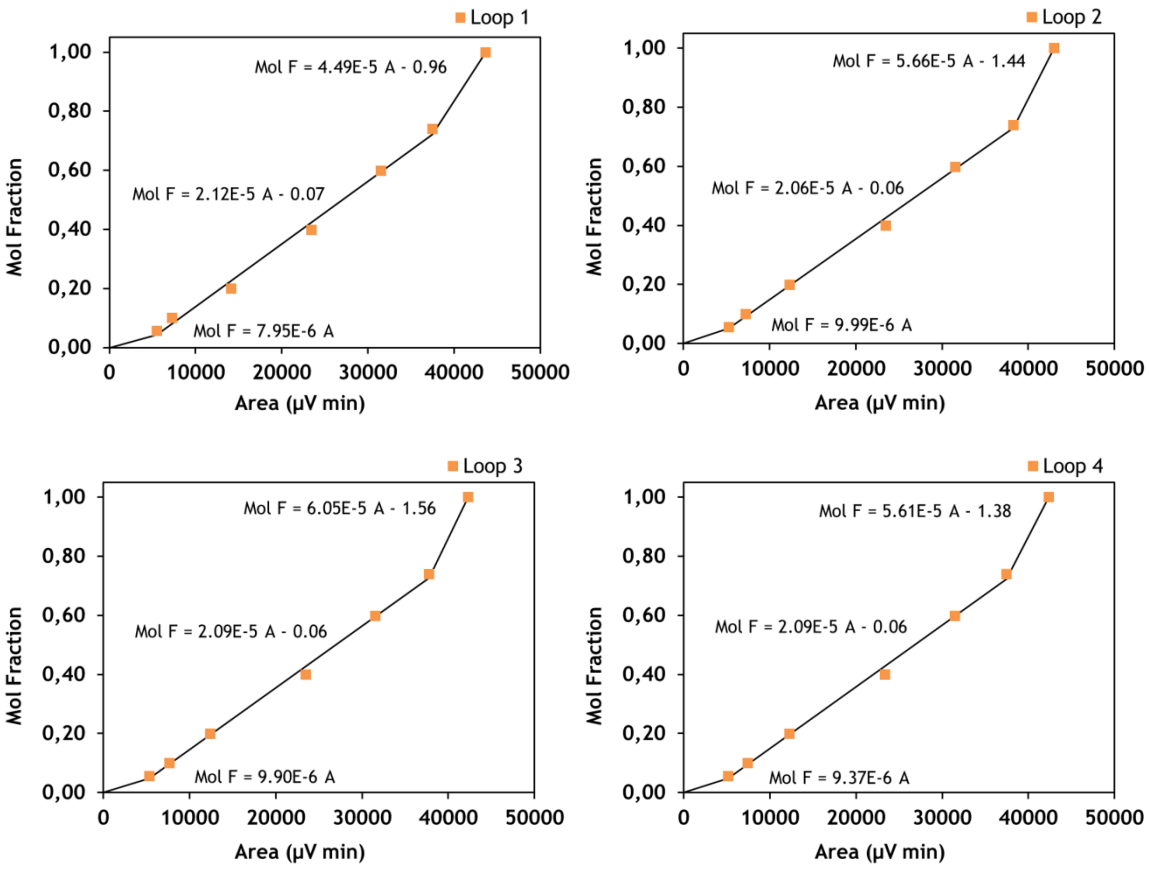

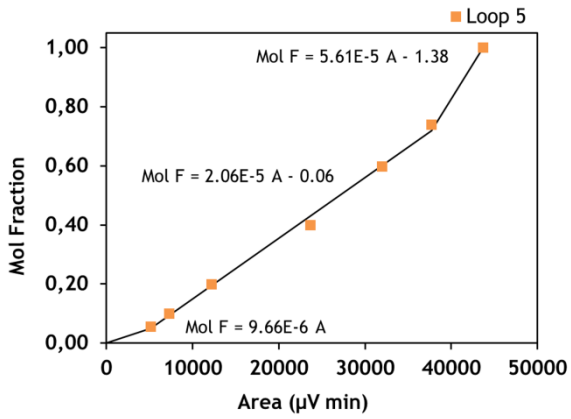
Loop 5
Mol F = 5.61E-5 A - 1.38
Mol F = 2.06E-5 A - 0.06
Mol F = 9.66E-6 A
Mol Fraction
Area (µV min)

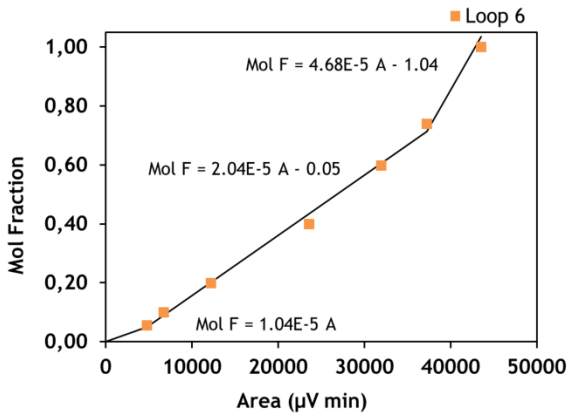
Loop 6
Mol F = 4.68E-5 A - 1.04
Mol F = 2.04E-5 A - 0.05
Mol F = 1.04E-5 A
Mol Fraction
Area (µV min)

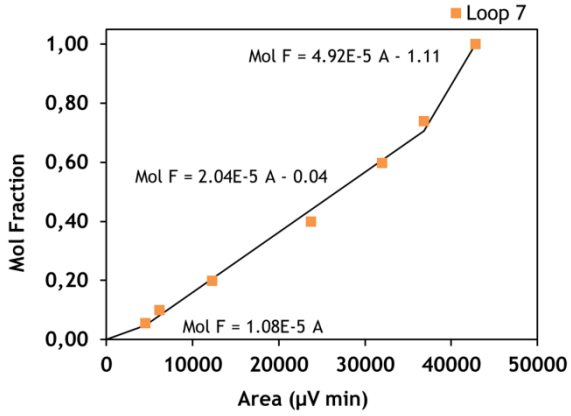
Loop 7
Mol F = 4.92E-5 A - 1.11
Mol F = 2.04E-5 A - 0.04
Mol F = 1.08E-5 A
Mol Fraction
Area (µV min)

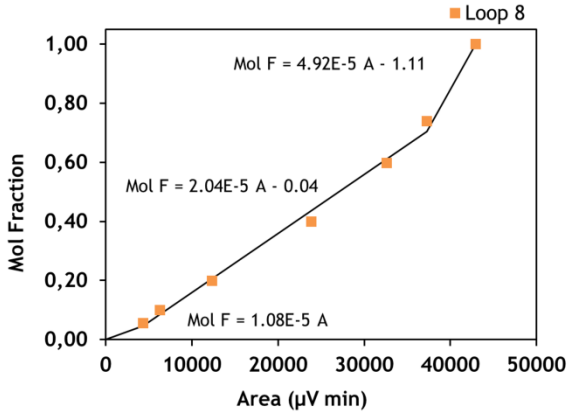
Loop 8
Mol F = 4.92E-5 A - 1.11
Mol F = 2.04E-5 A - 0.04
Mol F = 1.08E-5 A
Mol Fraction
Area (µV min)

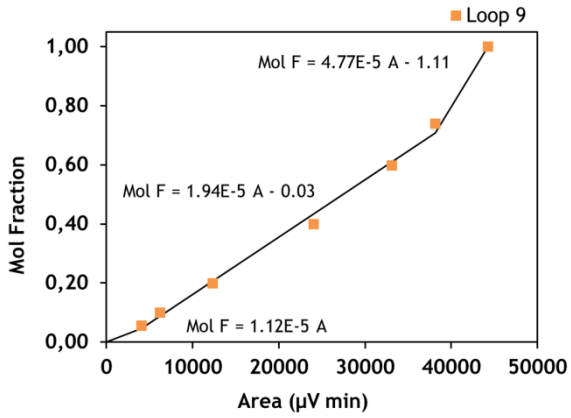
Loop 9
Mol F = 4.77E-5 A - 1.11
Mol F = 1.94E-5 A - 0.03
Mol F = 1.12E-5 A
Mol Fraction
Area (µV min)

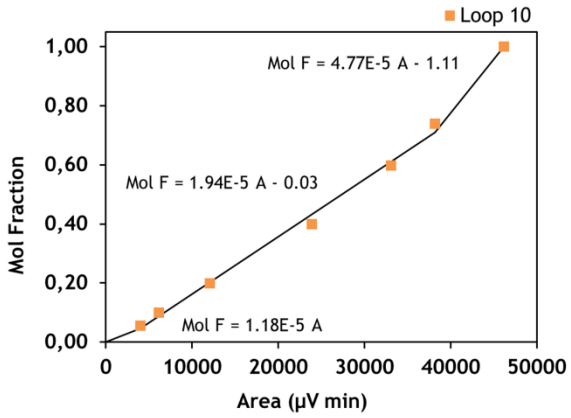
Loop 10
Mol F = 4.77E-5 A - 1.11
Mol F = 1.94E-5 A - 0.03
Mol F = 1.18E-5 A
Mol Fraction
Area (µV min)

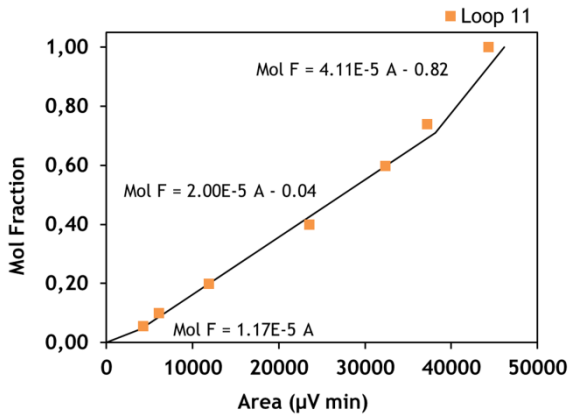
Loop 11
Mol F = 4.11E-5 A - 0.82
Mol F = 2.00E-5 A - 0.04
Mol F = 1.17E-5 A
Mol Fraction
Area (µV min)

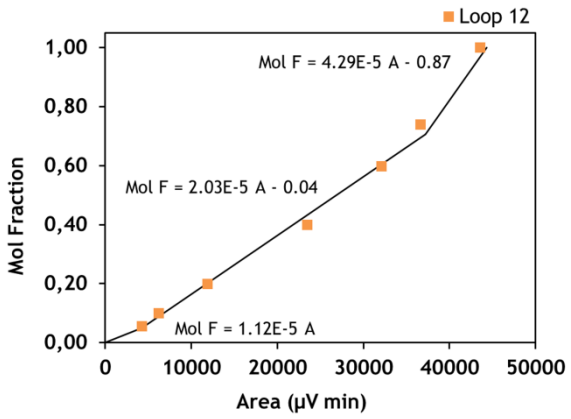
Loop 12
Mol F = 4.29E-5 A - 0.87
Mol F = 2.03E-5 A - 0.04
Mol F = 1.12E-5 A
Mol Fraction
Area (µV min)

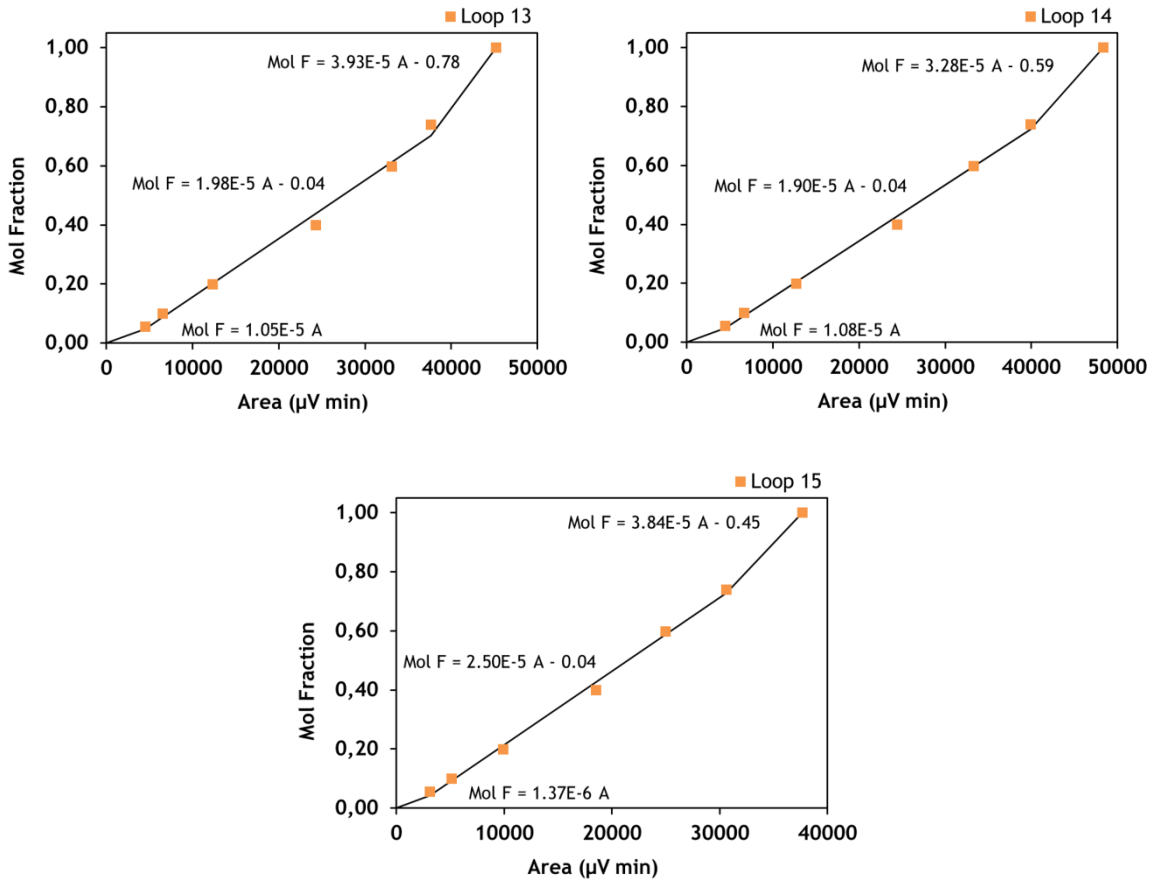

Figure A3.6 - Loops calibration (Loop 1 to 15) for carbon dioxide. Points correspond to experimental data and line to adjusted curve.

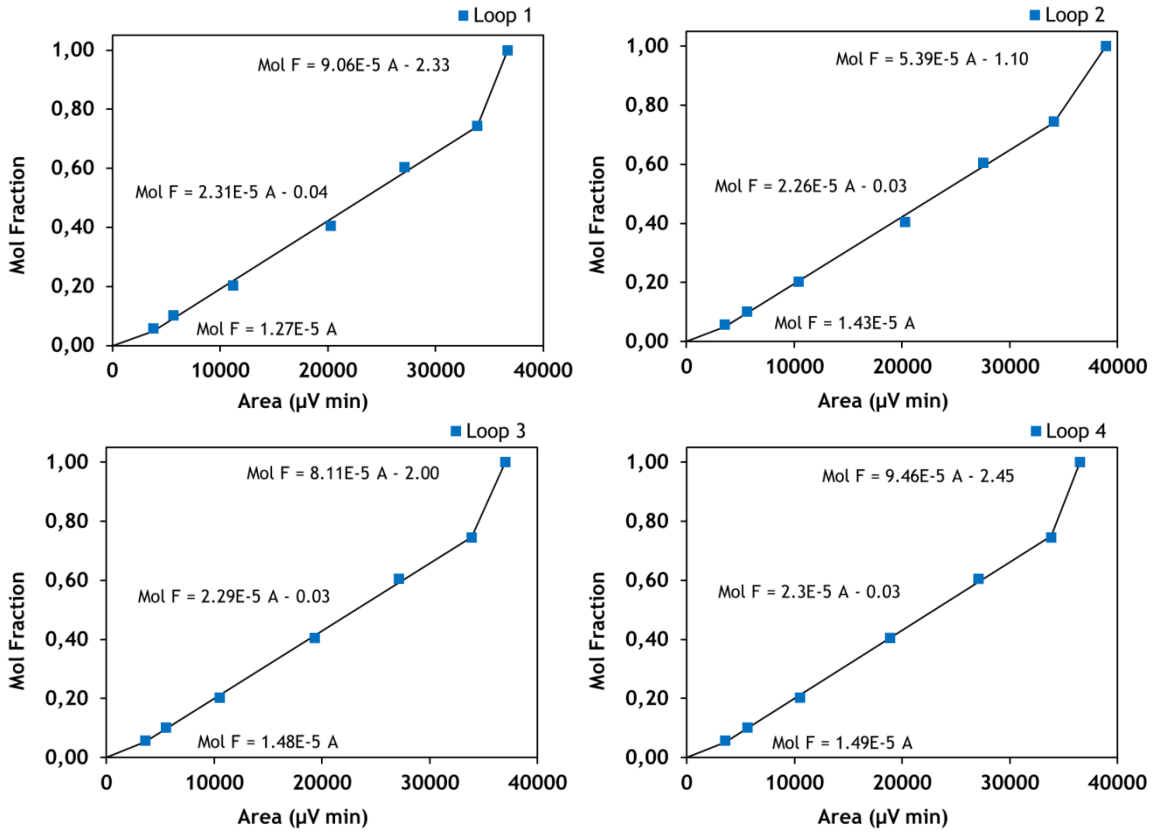

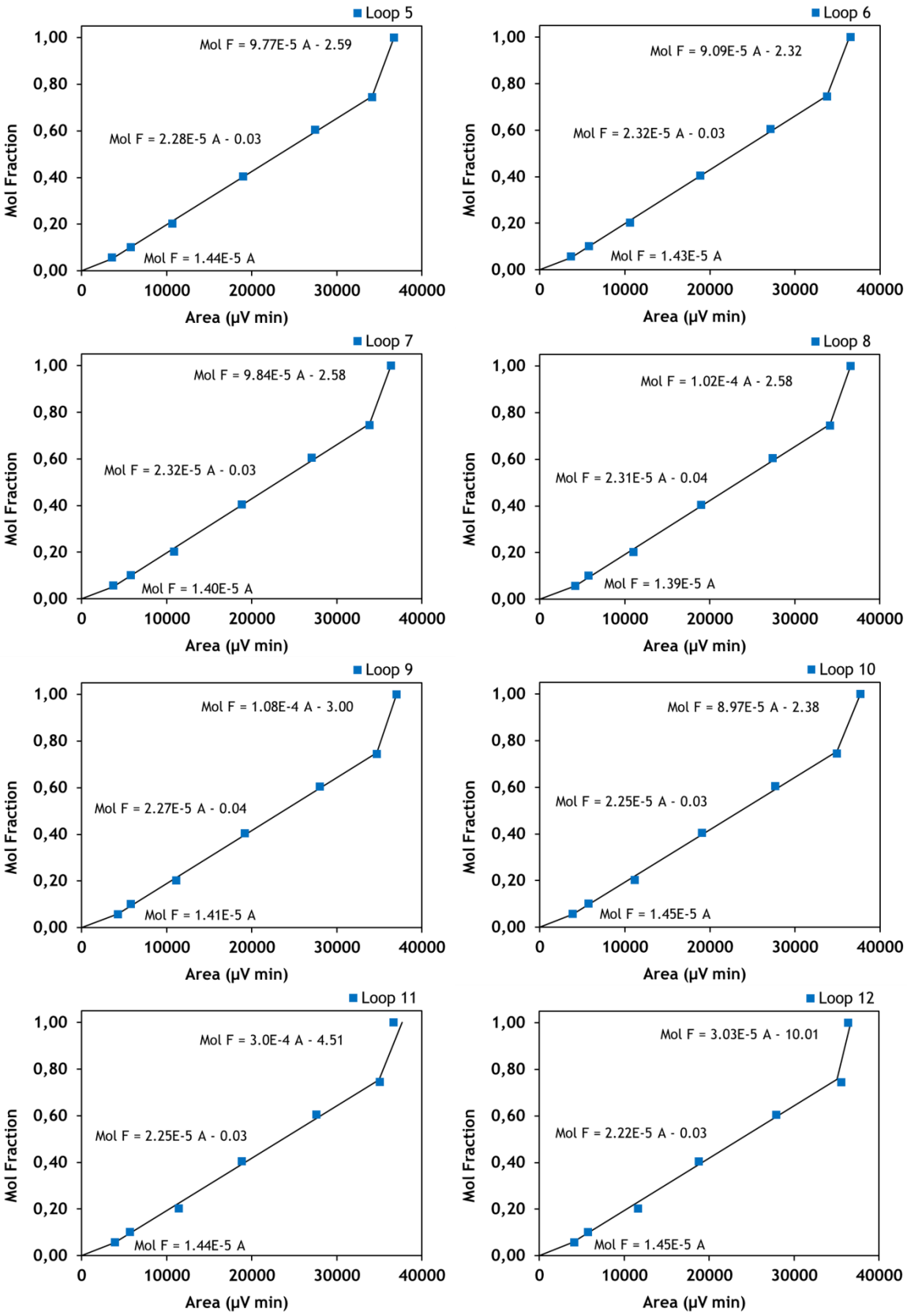
Loop 5
Mol F = 9.77E-5 A - 2.59
Mol F = 2.28E-5 A - 0.03
Mol F = 1.44E-5 A
Loop 6
Mol F = 9.09E-5 A - 2.32
Mol F = 2.32E-5 A - 0.03
Mol F = 1.43E-5 A
Loop 7
Mol F = 9.84E-5 A - 2.58
Mol F = 2.32E-5 A - 0.03
Mol F = 1.40E-5 A
Loop 8
Mol F = 1.02E-4 A - 2.58
Mol F = 2.31E-5 A - 0.04
Mol F = 1.39E-5 A
Loop 9
Mol F = 1.08E-4 A - 3.00
Mol F = 2.27E-5 A - 0.04
Mol F = 1.41E-5 A
Loop 10
Mol F = 8.97E-5 A - 2.38
Mol F = 2.25E-5 A - 0.03
Mol F = 1.45E-5 A
Loop 11
Mol F = 3.0E-4 A - 4.51
Mol F = 2.25E-5 A - 0.03
Mol F = 1.44E-5 A
Loop 12
Mol F = 3.03E-5 A - 10.01
Mol F = 2.22E-5 A - 0.03
Mol F = 1.45E-5 A
Mol Fraction
Area (µV min)
0,00
0,20
0,40
0,60
0,80
1,00
0
10000
20000
30000
40000

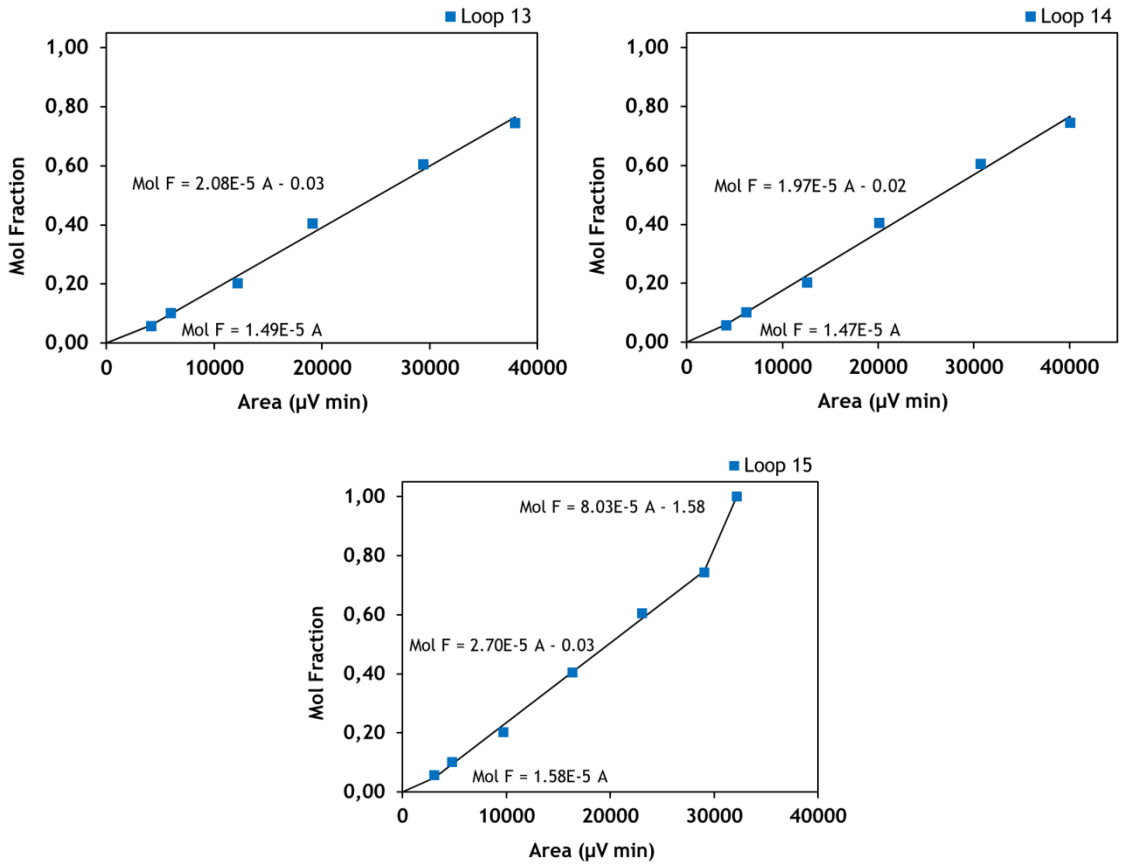

Figure A3.7 - Loops calibration (Loop 1 to 15) for nitrogen. Points correspond to experimental data and line to adjusted curve.

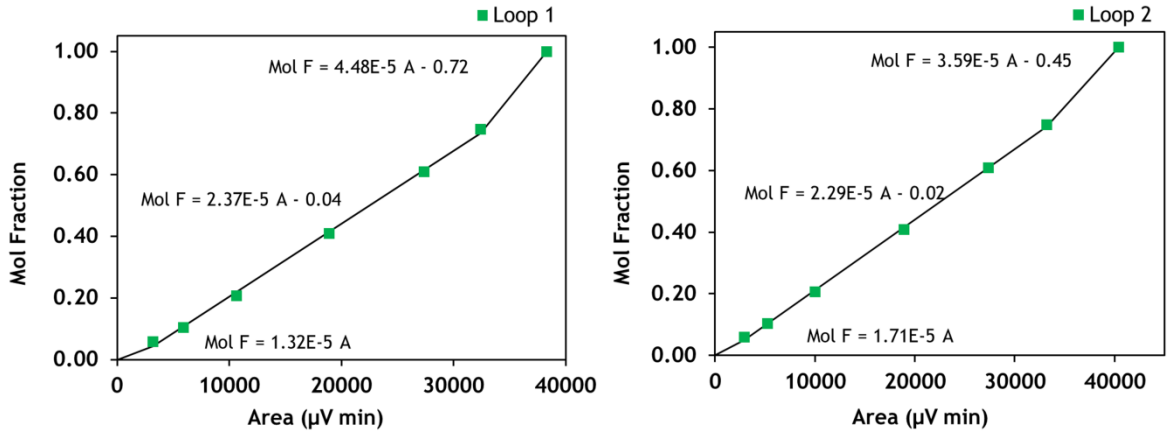

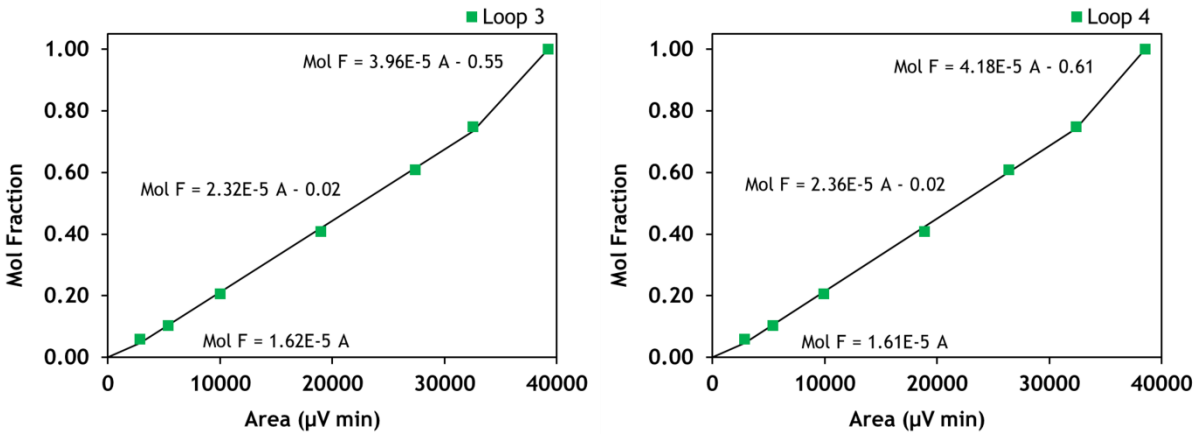
Loop 3
Mol F = 3.96E-5 A - 0.55
Mol F = 2.32E-5 A - 0.02
Mol F = 1.62E-5 A
Mol Fraction
Area (µV min)

Loop 4
Mol F = 4.18E-5 A - 0.61
Mol F = 2.36E-5 A - 0.02
Mol F = 1.61E-5 A
Mol Fraction
Area (µV min)

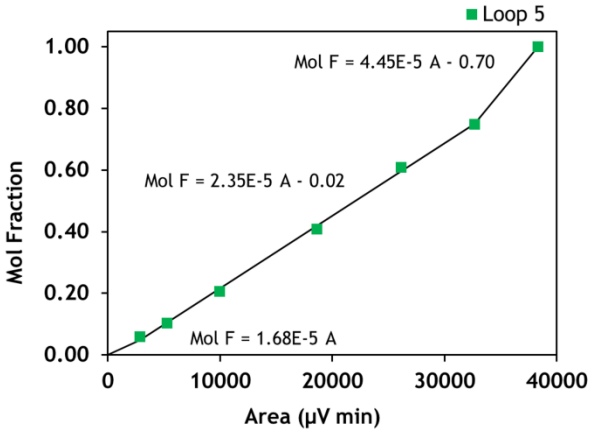
Loop 5
Mol F = 4.45E-5 A - 0.70
Mol F = 2.35E-5 A - 0.02
Mol F = 1.68E-5 A
Mol Fraction
Area (µV min)

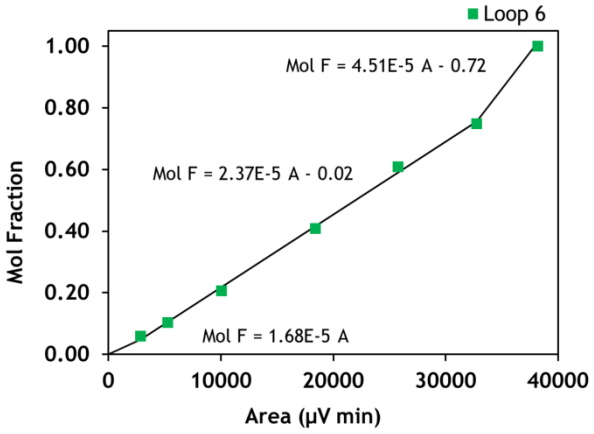
Loop 6
Mol F = 4.51E-5 A - 0.72
Mol F = 2.37E-5 A - 0.02
Mol F = 1.68E-5 A
Mol Fraction
Area (µV min)

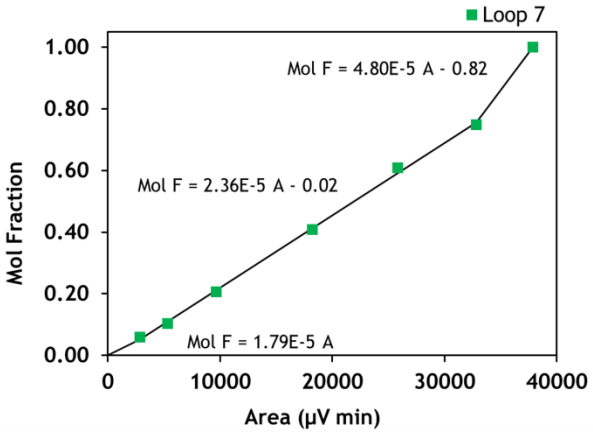
Loop 7
Mol F = 4.80E-5 A - 0.82
Mol F = 2.36E-5 A - 0.02
Mol F = 1.79E-5 A
Mol Fraction
Area (µV min)

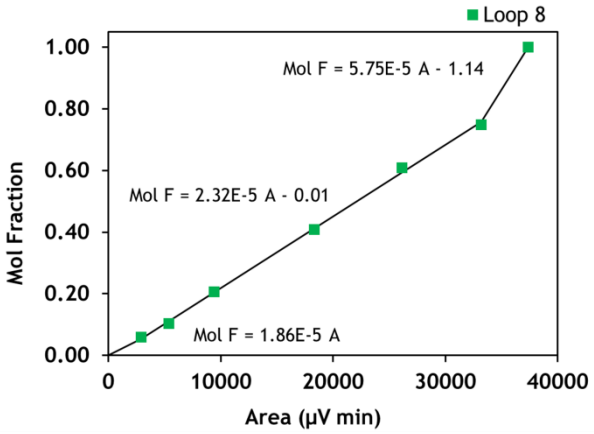
Loop 8
Mol F = 5.75E-5 A - 1.14
Mol F = 2.32E-5 A - 0.01
Mol F = 1.86E-5 A
Mol Fraction
Area (µV min)

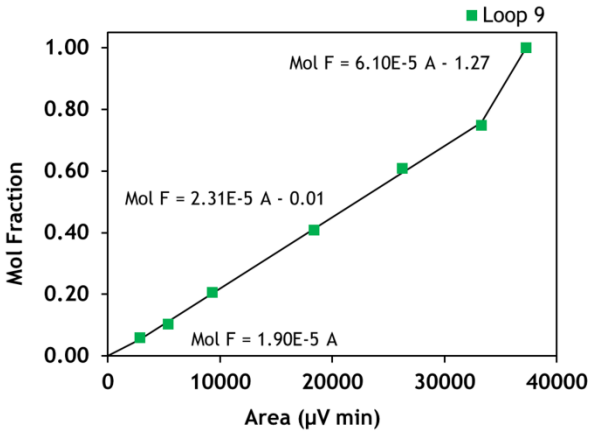
Loop 9
Mol F = 6.10E-5 A - 1.27
Mol F = 2.31E-5 A - 0.01
Mol F = 1.90E-5 A
Mol Fraction
Area (µV min)

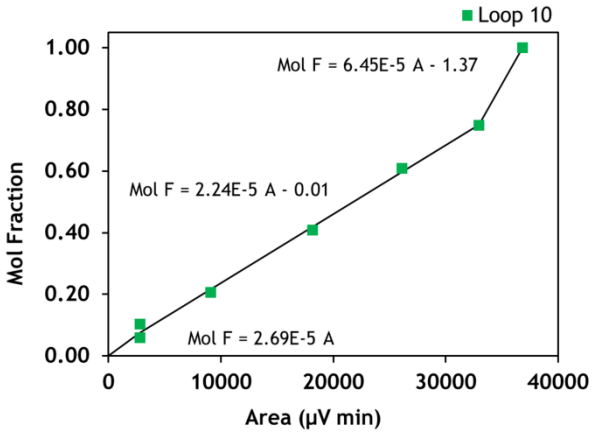
Loop 10
Mol F = 6.45E-5 A - 1.37
Mol F = 2.24E-5 A - 0.01
Mol F = 2.69E-5 A
Mol Fraction
Area (µV min)

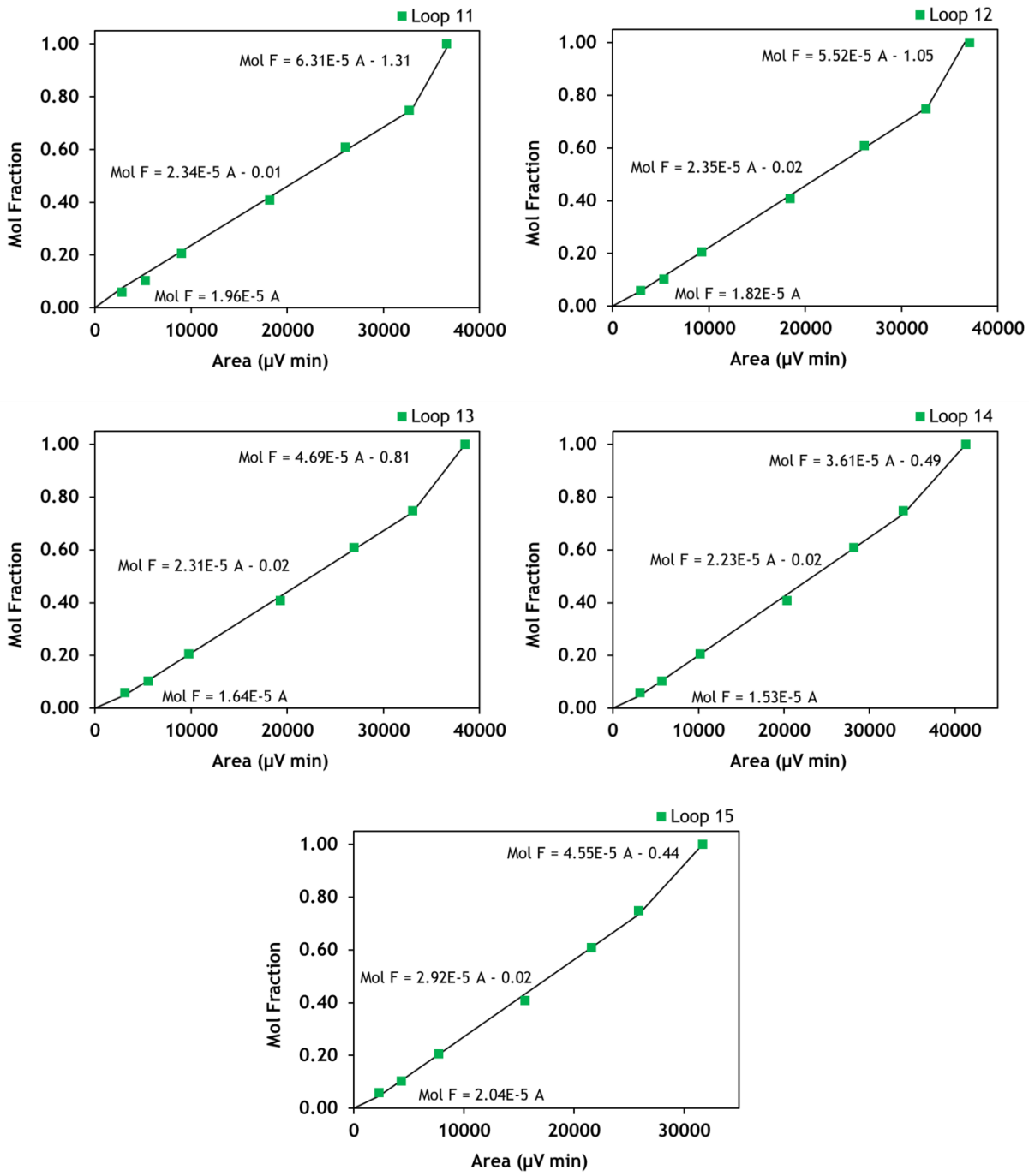

Figure A3.8 - Loops calibration (Loop 1 to 15) for methane. Points correspond to experimental data and line to adjusted curve.

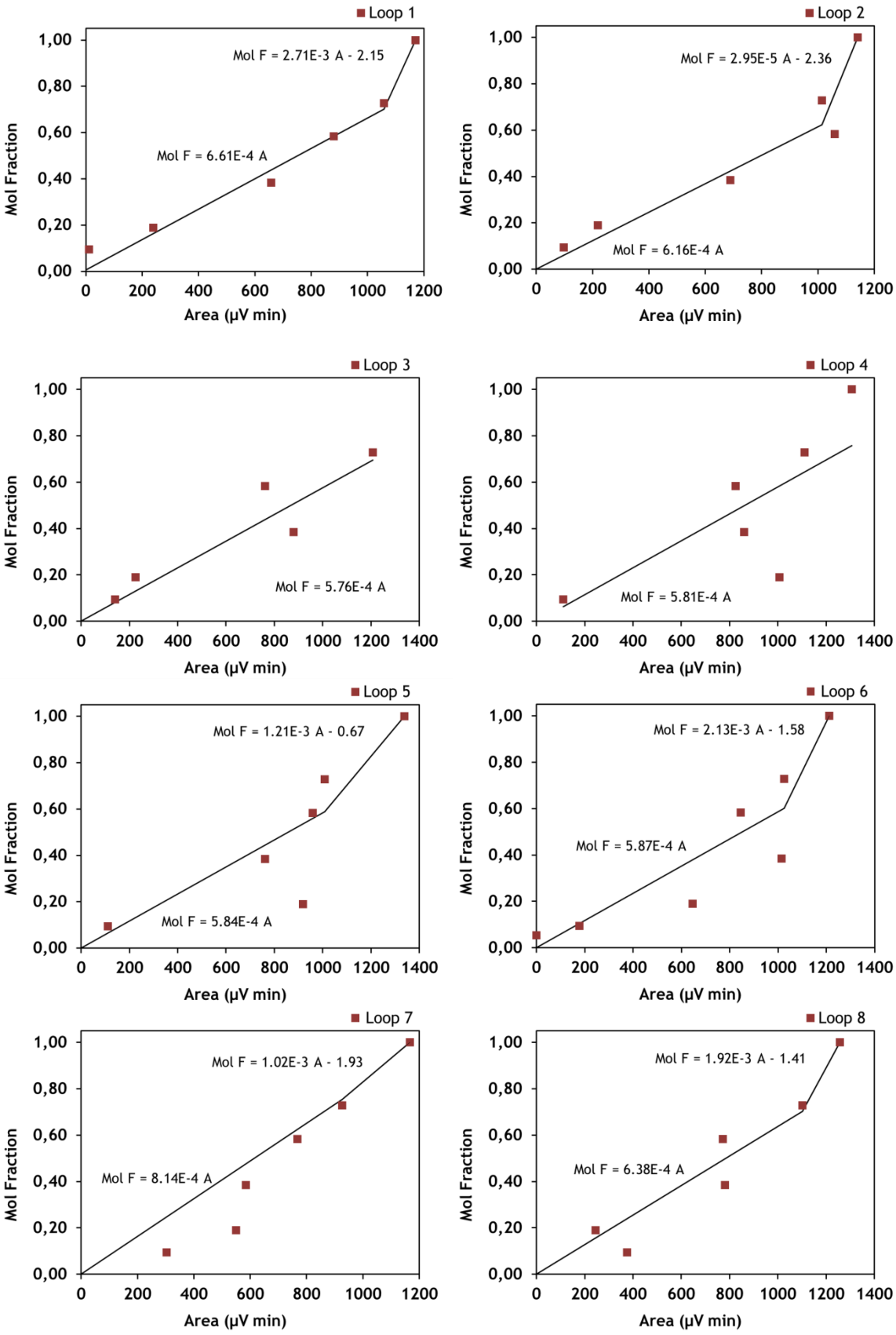
Loop 1
Mol F = 2.71E-3 A - 2.15
Mol F = 6.61E-4 A
Mol Fraction
Area (µV min)
Loop 2
Mol F = 2.95E-5 A - 2.36
Mol F = 6.16E-4 A
Mol Fraction
Area (µV min)
Loop 3
Mol F = 5.76E-4 A
Mol Fraction
Area (µV min)
Loop 4
Mol F = 5.81E-4 A
Mol Fraction
Area (µV min)
Loop 5
Mol F = 1.21E-3 A - 0.67
Mol F = 5.84E-4 A
Mol Fraction
Area (µV min)
Loop 6
Mol F = 2.13E-3 A - 1.58
Mol F = 5.87E-4 A
Mol Fraction
Area (µV min)
Loop 7
Mol F = 1.02E-3 A - 1.93
Mol F = 8.14E-4 A
Mol Fraction
Area (µV min)
Loop 8
Mol F = 1.92E-3 A - 1.41
Mol F = 6.38E-4 A
Mol Fraction
Area (µV min)

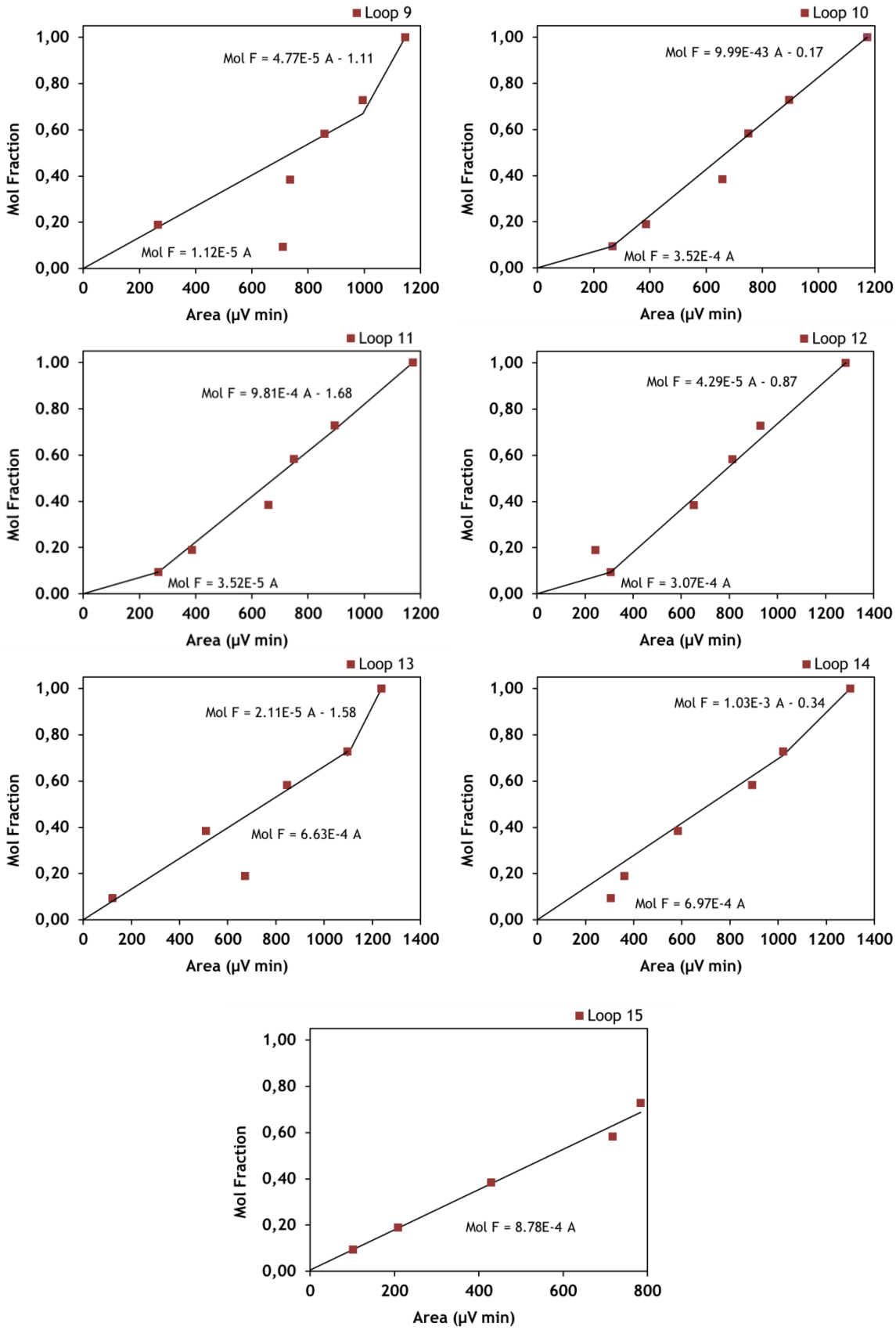

Figure A3.9 - Loops calibration (Loop 1 to 15) for hydrogen. Points correspond to experimental data and line to adjusted curve.

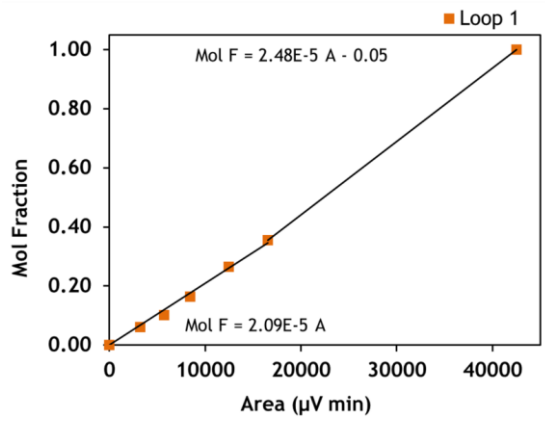
Loop 1
Mol F = 2.48E-5 A - 0.05
Mol F = 2.09E-5 A
Mol Fraction
Area (µV min)
0.00
0.20
0.40
0.60
0.80
1.00
0
10000
20000
30000
40000

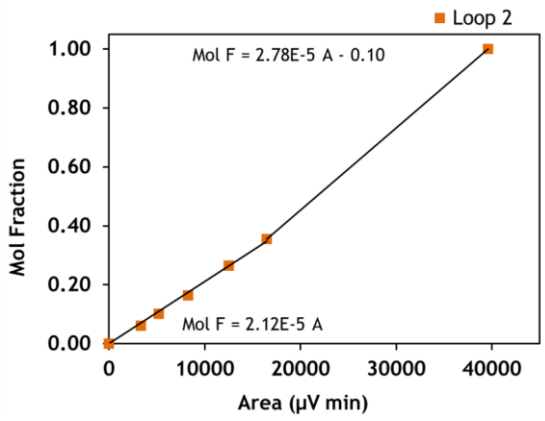
Loop 2
Mol F = 2.78E-5 A - 0.10
Mol F = 2.12E-5 A
Mol Fraction
Area (µV min)
0.00
0.20
0.40
0.60
0.80
1.00
0
10000
20000
30000
40000

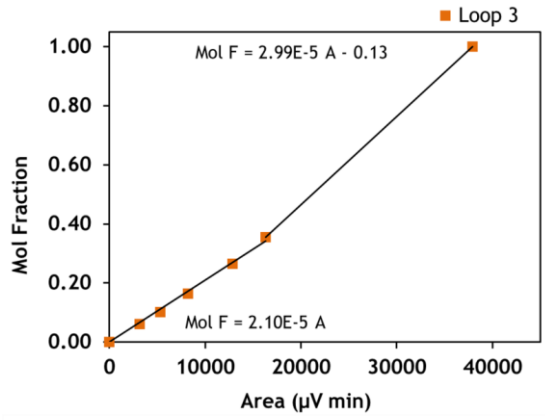
Loop 3
Mol F = 2.99E-5 A - 0.13
Mol F = 2.10E-5 A
Mol Fraction
Area (µV min)
0.00
0.20
0.40
0.60
0.80
1.00
0
10000
20000
30000
40000

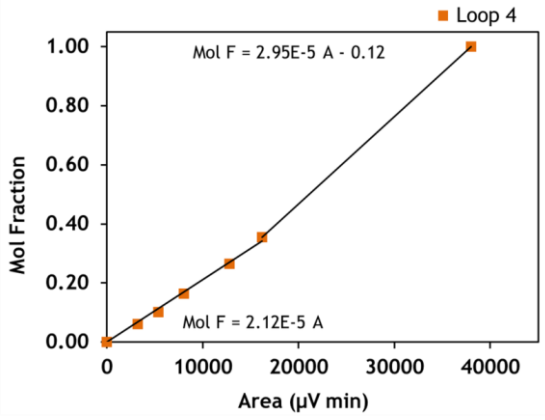
Loop 4
Mol F = 2.95E-5 A - 0.12
Mol F = 2.12E-5 A
Mol Fraction
Area (µV min)
0.00
0.20
0.40
0.60
0.80
1.00
0
10000
20000
30000
40000

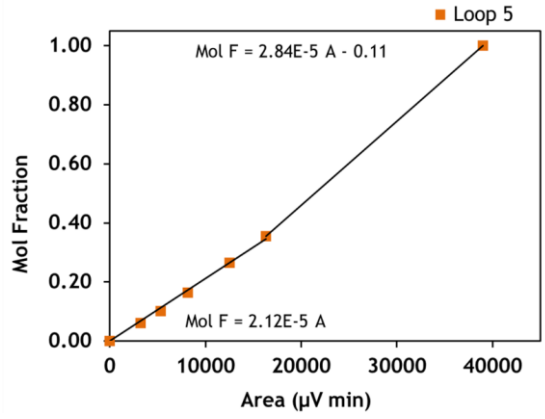
Loop 5
Mol F = 2.84E-5 A - 0.11
Mol F = 2.12E-5 A
Mol Fraction
Area (µV min)
0.00
0.20
0.40
0.60
0.80
1.00
0
10000
20000
30000
40000

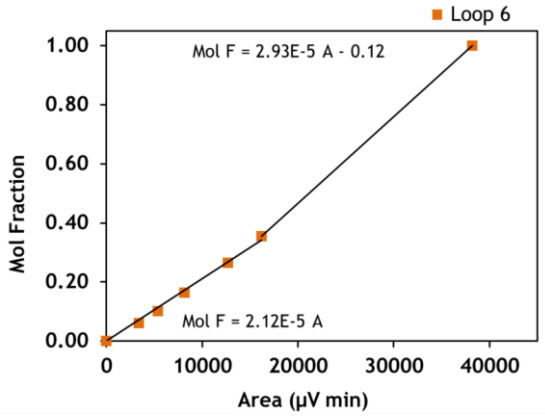
Loop 6
Mol F = 2.93E-5 A - 0.12
Mol F = 2.12E-5 A
Mol Fraction
Area (µV min)
0.00
0.20
0.40
0.60
0.80
1.00
0
10000
20000
30000
40000

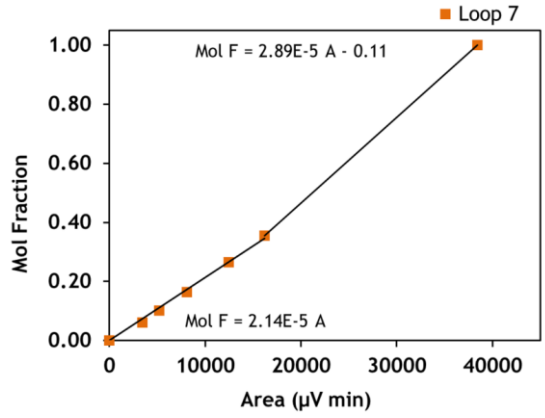
Loop 7
Mol F = 2.89E-5 A - 0.11
Mol F = 2.14E-5 A
Mol Fraction
Area (µV min)
0.00
0.20
0.40
0.60
0.80
1.00
0
10000
20000
30000
40000

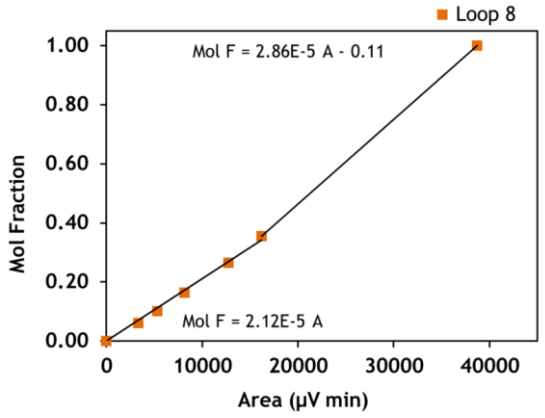
Loop 8
Mol F = 2.86E-5 A - 0.11
Mol F = 2.12E-5 A
Mol Fraction
Area (µV min)
0.00
0.20
0.40
0.60
0.80
1.00
0
10000
20000
30000
40000

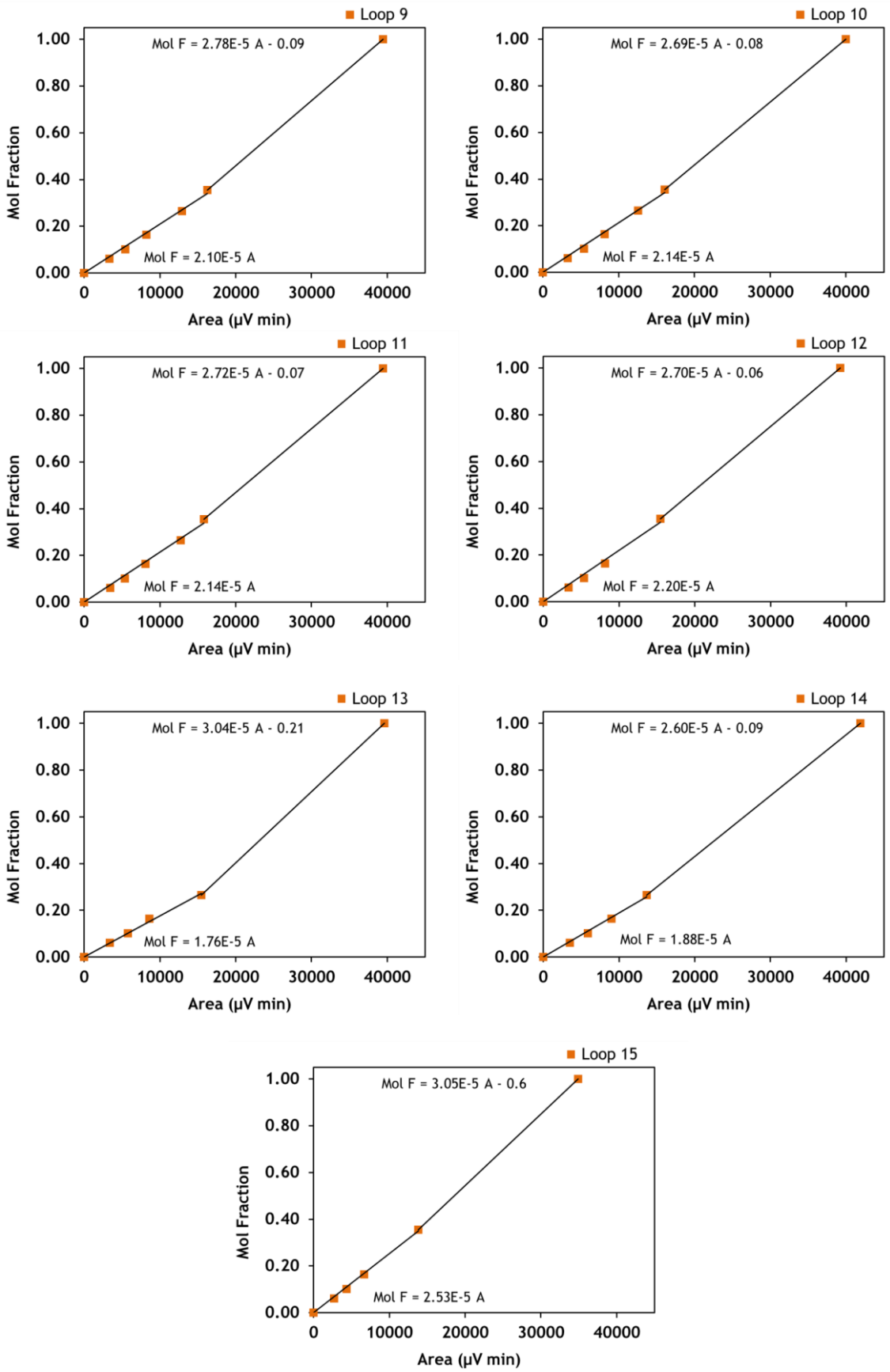

Figure A3.10 - Loops calibration (Loop 1 to 15) for carbon monoxide. Points correspond to experimental data and line to adjusted curve.

Appendix 4 - Breakthrough curves (Exp. 8 to 20)

As mentioned in section 4.3, some breakthrough curves had already been performed before the start of this thesis (Table 8). These experimental results were simulated in this work and are shown in Figure A4.1 to Figure A4.13.

Exp.8 - CO_2/He

T = 50 °C P = 4.5 bar y_{CO2} = 0.417 F_{feed} = 0.353 mmol s^{-1}

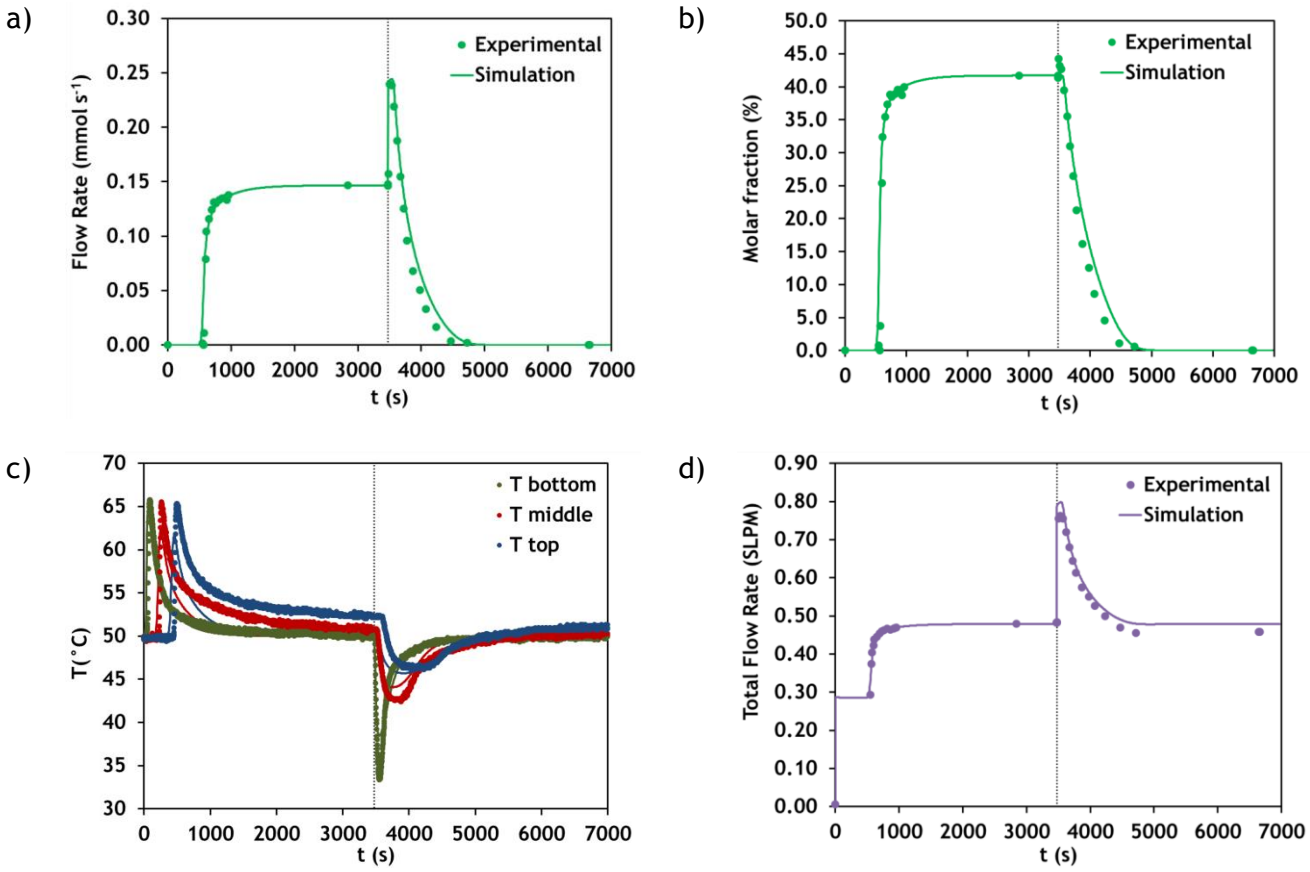

Figure A4.1 - Breakthrough results of experiment 8 (CO_2/He): molar flow rate at the column outlet (a), molar fraction at the column outlet (b), temperatures histories at 8.1 cm (bottom), 19.1 cm (middle) and 30 cm (top) (c) and total flow rate at the column outlet (d). Points correspond to experimental data and lines to simulation results. Vertical line corresponds to the beginning of desorption.

Exp.9 - CO_2/He

T = 50 ºC P = 4.5 bar y_{CO2} = 0.842 F_{feed} = 0.380 mmol s^{-1}

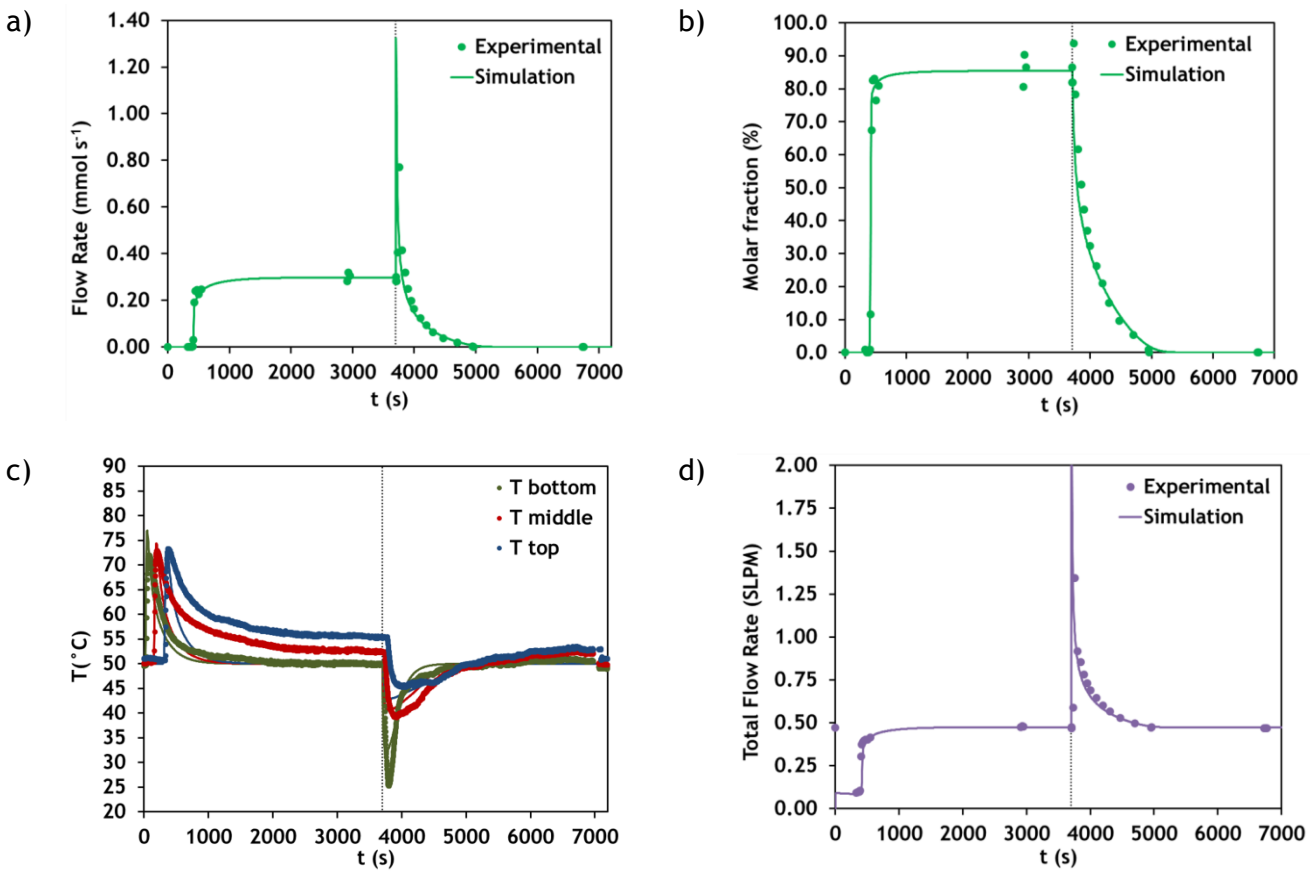

Figure A4.2 - Breakthrough results of experiment 2 (CO_2/He): molar flow rate at the column outlet (a), molar fraction at the column outlet (b), temperatures histories at 8.1 cm (bottom), 19.1 cm (middle) and 30 cm (top) (c) and total flow rate at the column outlet (d). Points correspond to experimental data and lines to simulation results. Vertical line corresponds to the beginning of desorption.

Exp.10 - CO/He

T = 50 ºC P = 4.5 bar y_{CO} = 0.080 F_{feed} = 0.274 mmol s^{-1}

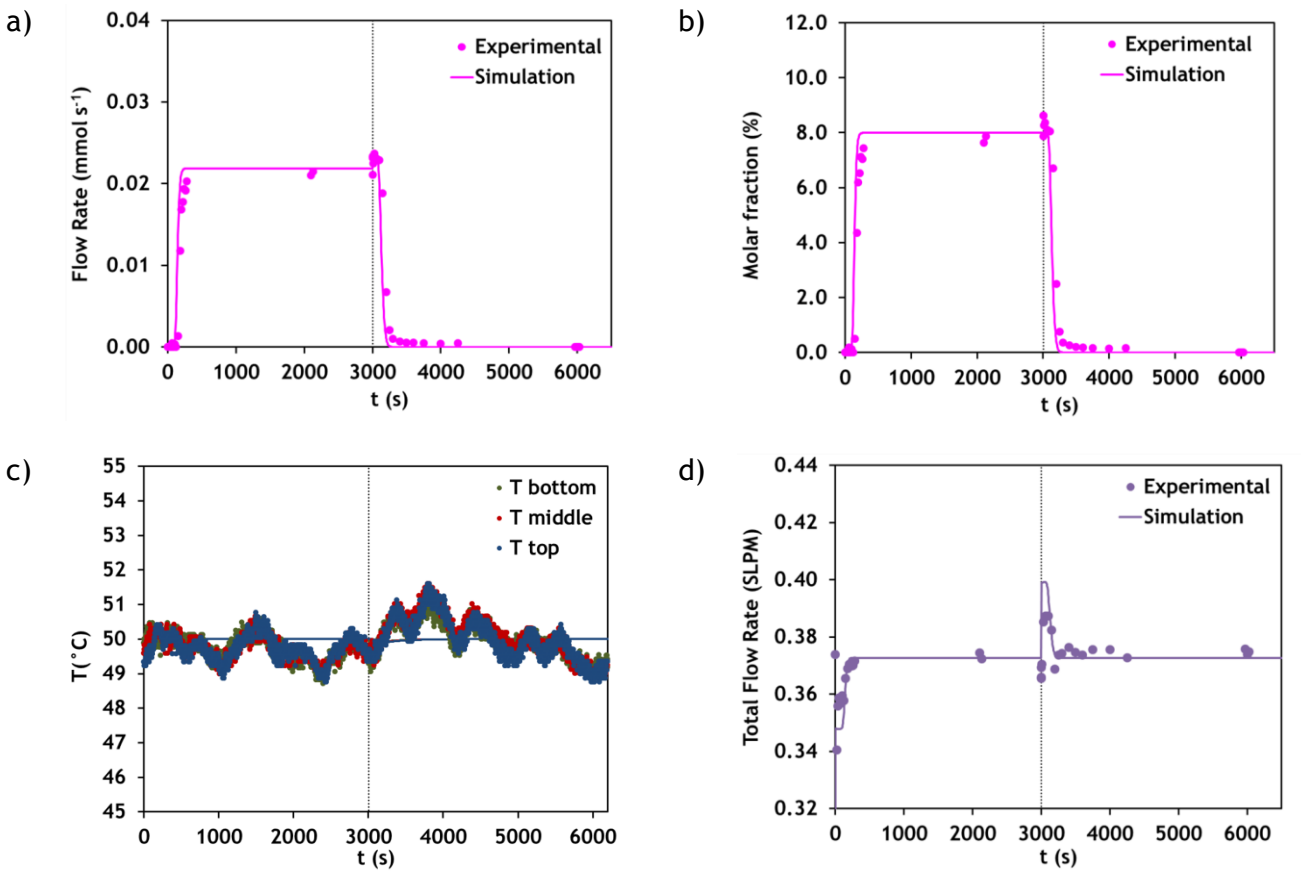

Figure A4.3 - Breakthrough results of experiment 10 (CO/He): molar flow rate at the column outlet (a), molar fraction at the column outlet (b), temperatures histories at 8.1 cm (bottom), 19.1 cm (middle) and 30 cm (top) (c) and total flow rate at the column outlet (d). Points correspond to experimental data and lines to simulation results. Vertical line corresponds to the beginning of desorption.

Exp.11 - CO/He

T = 50 ºC P = 4.5 bar y_{CO} = 0.215 F_{feed} = 0.290 mmol s^{-1}

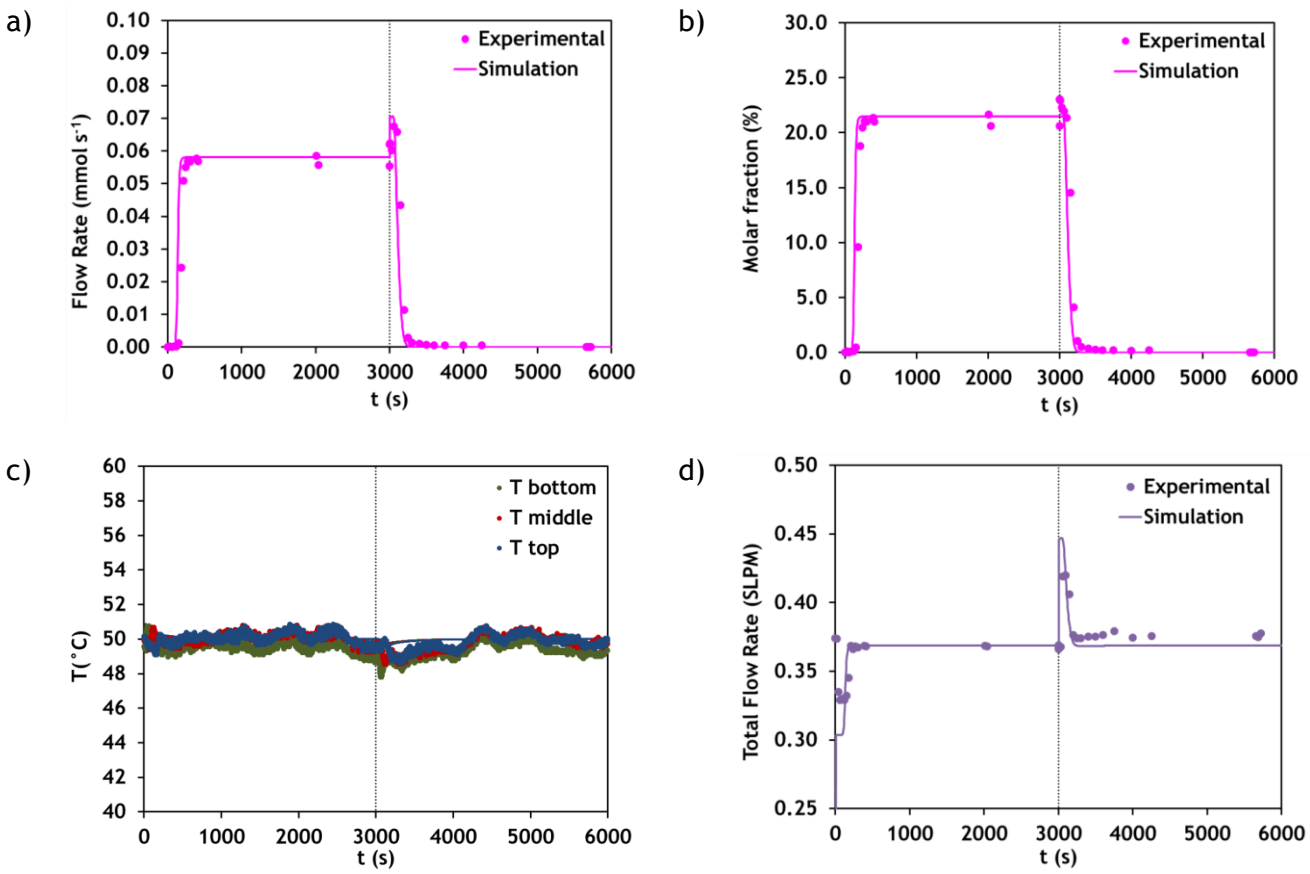

Figure A4.4 - Breakthrough results of experiment 11 (CO/He): molar flow rate at the column outlet (a), molar fraction at the column outlet (b), temperatures histories at 8.1 cm (bottom), 19.1 cm (middle) and 30 cm (top) (c) and total flow rate at the column outlet (d). Points correspond to experimental data and lines to simulation results. Vertical line corresponds to the beginning of desorption.

Exp.12 - N_2/He

T = 50 ºC P = 4.5 bar y_{N2} = 0.178 F_{feed} = 0.346 mmol s^{-1}

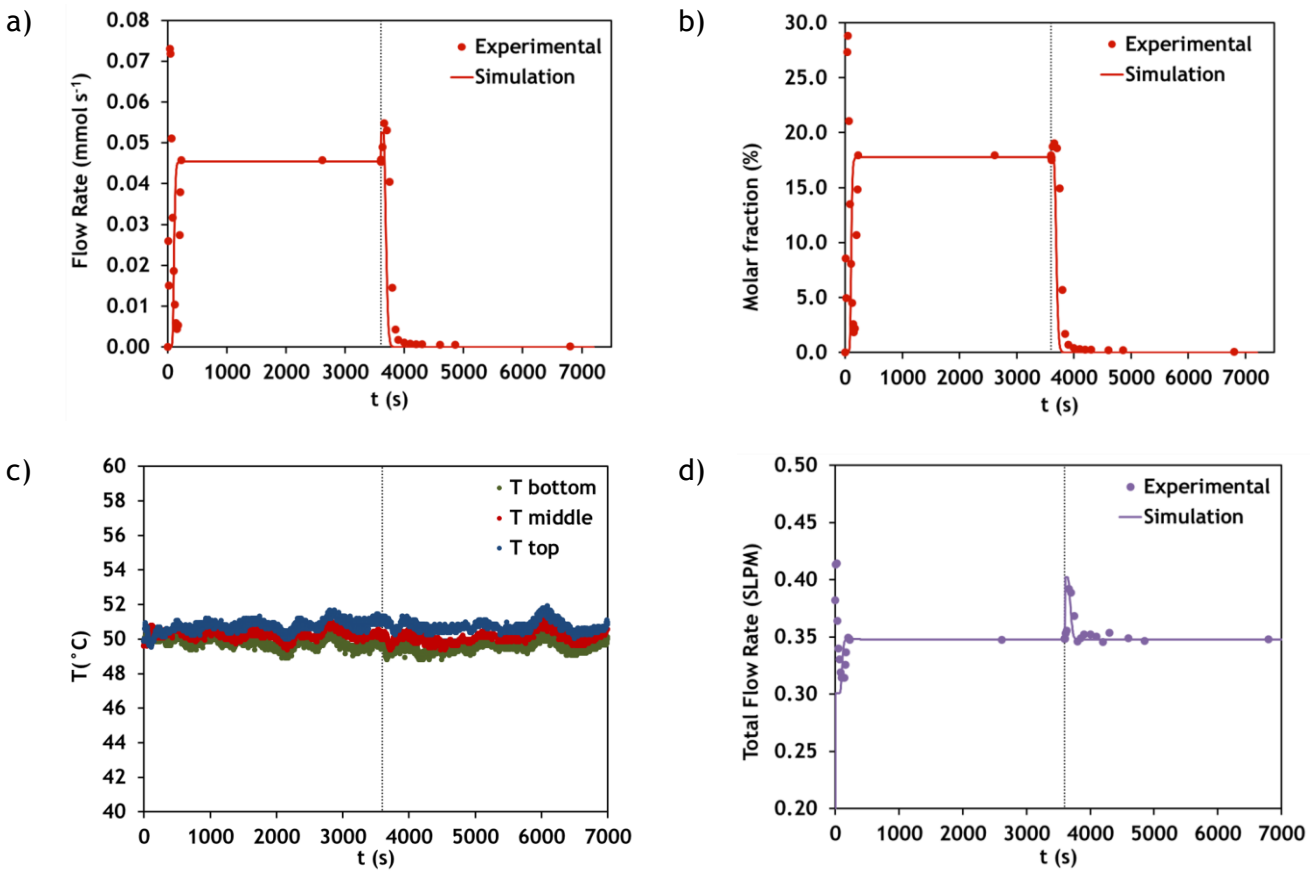

Figure A4.5 - Breakthrough results of experiment 12 (N_2/He): molar flow rate at the column outlet (a), molar fraction at the column outlet (b), temperatures histories at 8.1 cm (bottom), 19.1 cm (middle) and 30 cm (top) (c) and total flow rate at the column outlet (d). Points correspond to experimental data and lines to simulation results. Vertical line corresponds to the beginning of desorption.

Exp.13 - N_2/He

T = 50 ºC P = 4.5 bar y_{N2} = 0.829 F_{feed} = 0.445 mmol s^{-1}

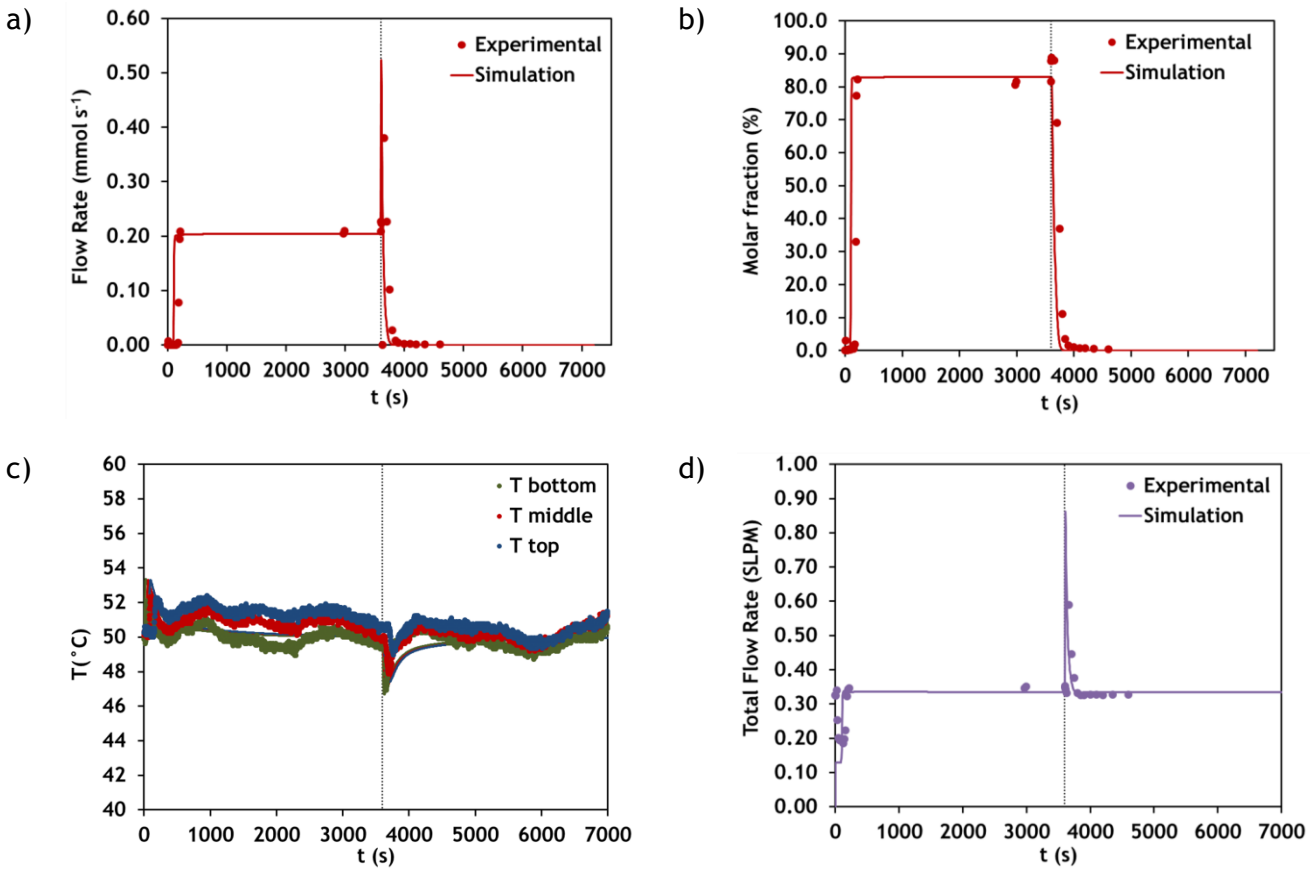

Figure A4.6 - Breakthrough results of experiment 13 (N_2/He): molar flow rate at the column outlet (a), molar fraction at the column outlet (b), temperatures histories at 8.1 cm (bottom), 19.1 cm (middle) and 30 cm (top) (c) and total flow rate at the column outlet (d). Points correspond to experimental data and lines to simulation results. Vertical line corresponds to the beginning of desorption.

Exp.14 - H_2/He

T = 50 ºC P = 4.5 bar Y_{H2} = 0.570 F_{feed} = 0.139 mmol s^{-1}

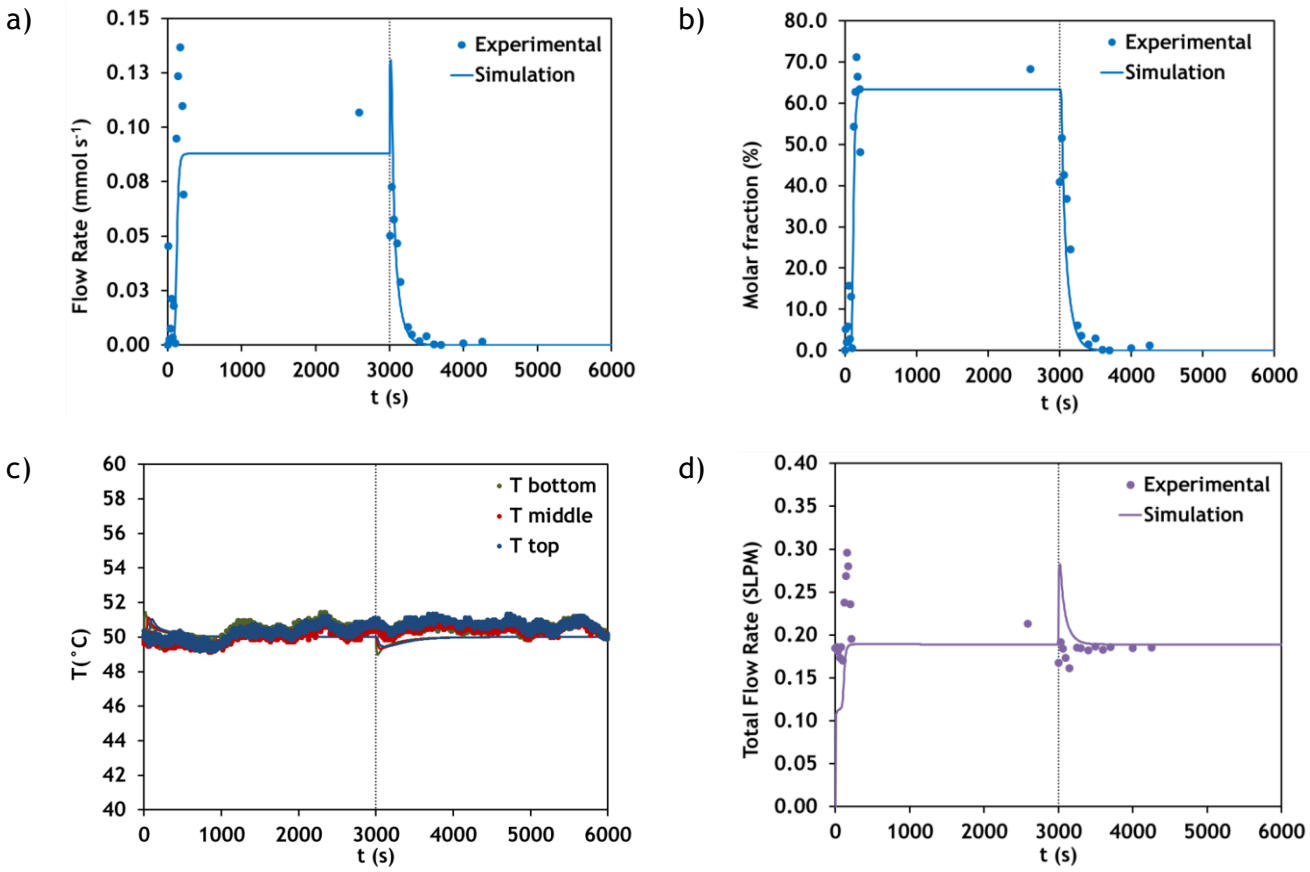

Figure A4.7 - Breakthrough results of experiment 14 (H_2/He): molar flow rate at the column outlet (a), molar fraction at the column outlet (b), temperatures histories at 8.1 cm (bottom), 19.1 cm (middle) and 30 cm (top) (c) and total flow rate at the column outlet (d). Points correspond to experimental data and lines to simulation results. Vertical line corresponds to the beginning of desorption.

Exp.15 - CH_4/He

T = 50 ºC P = 4.5 bar y_{CH4} = 0.199 F_{feed} = 0.242 mmol s^{-1}

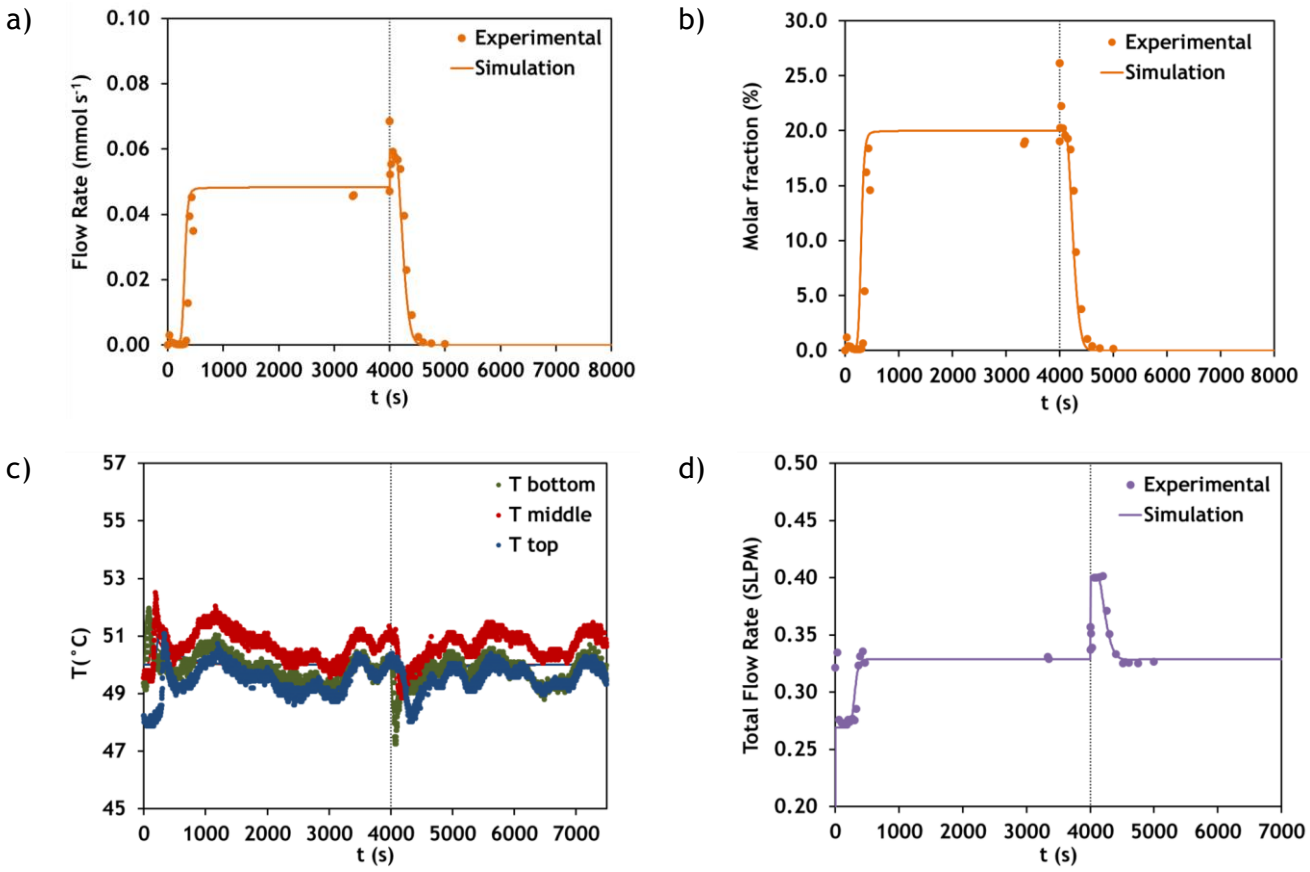

Figure A4.8 - Breakthrough results of experiment 15 (CH_4/He): molar flow rate at the column outlet (a), molar fraction at the column outlet (b), temperatures histories at 8.1 cm (bottom), 19.1 cm (middle) and 30 cm (top) (c) and total flow rate at the column outlet (d). Points correspond to experimental data and lines to simulation results. Vertical line corresponds to the beginning of desorption.

Exp.16 - CH_4/He

T = 50 ºC P = 4.5 bar y_{CH4} = 0.789 F_{feed} = 0.245 mmol s^{-1}

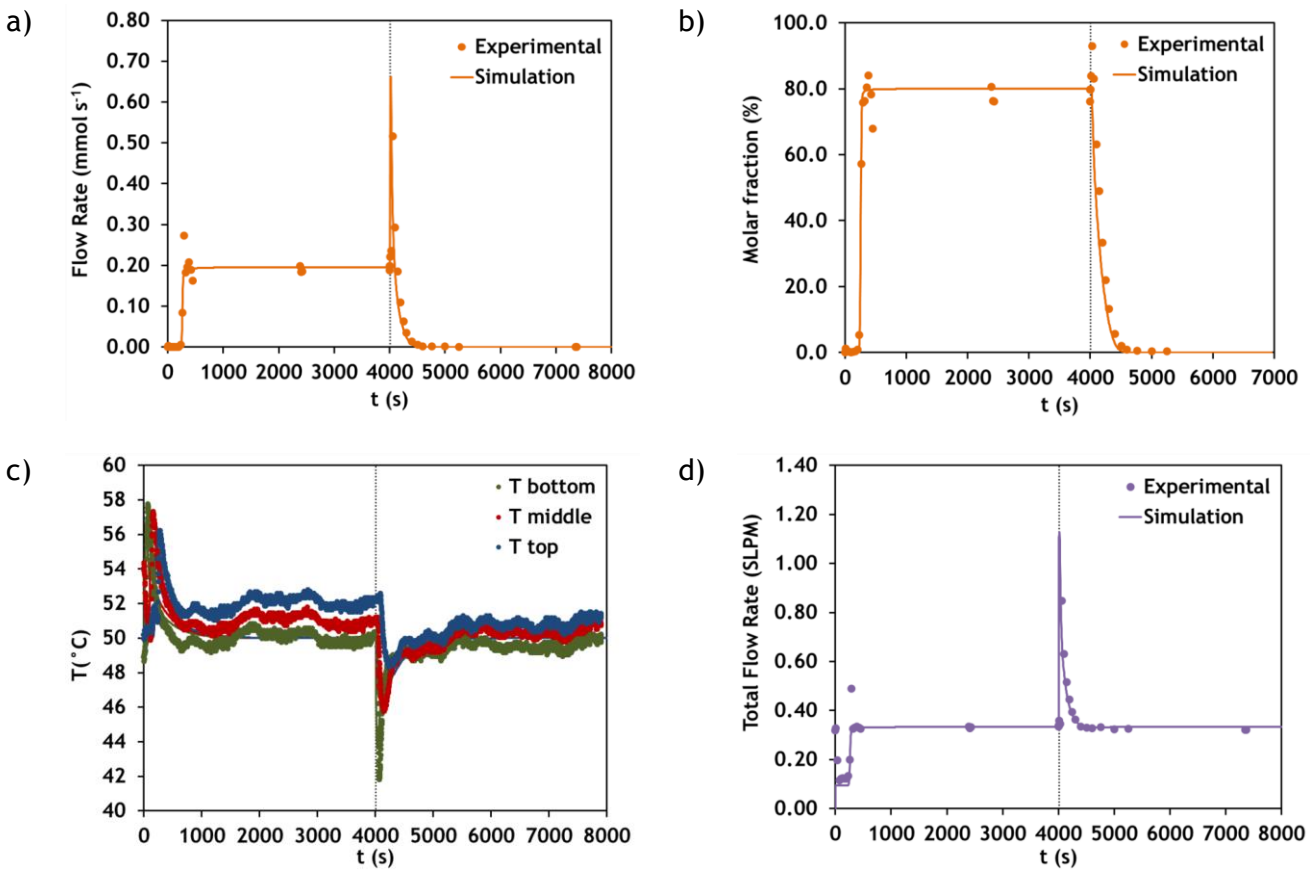

Figure A4.9 - Breakthrough results of experiment 16 (CH_4/He): molar flow rate at the column outlet (a), molar fraction at the column outlet (b), temperatures histories at 8.1 cm (bottom), 19.1 cm (middle) and 30 cm (top) (c) and total flow rate at the column outlet (d). Points correspond to experimental data and lines to simulation results. Vertical line corresponds to the beginning of desorption.

Exp.17 - CO_2/N_2/He

T = 50 ºC P = 4.5 bar y_{CO2} = 0.425 F_{feed} = 0.385 mmol s^{-1}

y_{N2} = 0.080

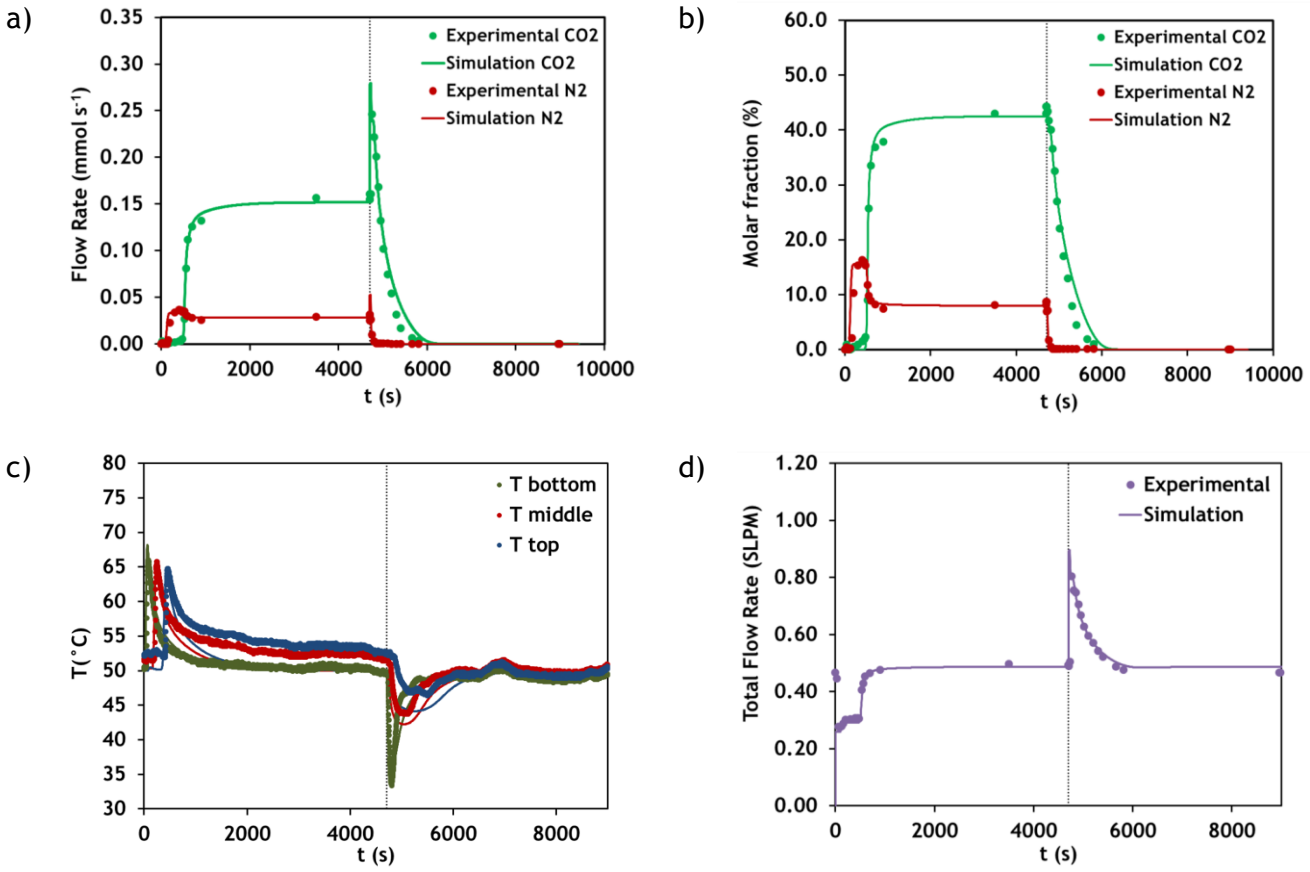

Figure A4.10 - Breakthrough results of experiment 17 (CO_2/N_2/He): molar flow rate at the column outlet (a), molar fraction at the column outlet (b), temperatures histories at 8.1 cm (bottom), 19.1 cm (middle) and 30 cm (top) (c) and total flow rate at the column outlet (d). Points correspond to experimental data and lines to simulation results. Vertical line corresponds to the beginning of desorption.

Exp.18 - CO_2/N_2/He

T = 50 ºC P = 4.5 bar y_{CO2} = 0.687 F_{feed} = 0.439 mmol s^{-1}

y_{N2} = 0.113

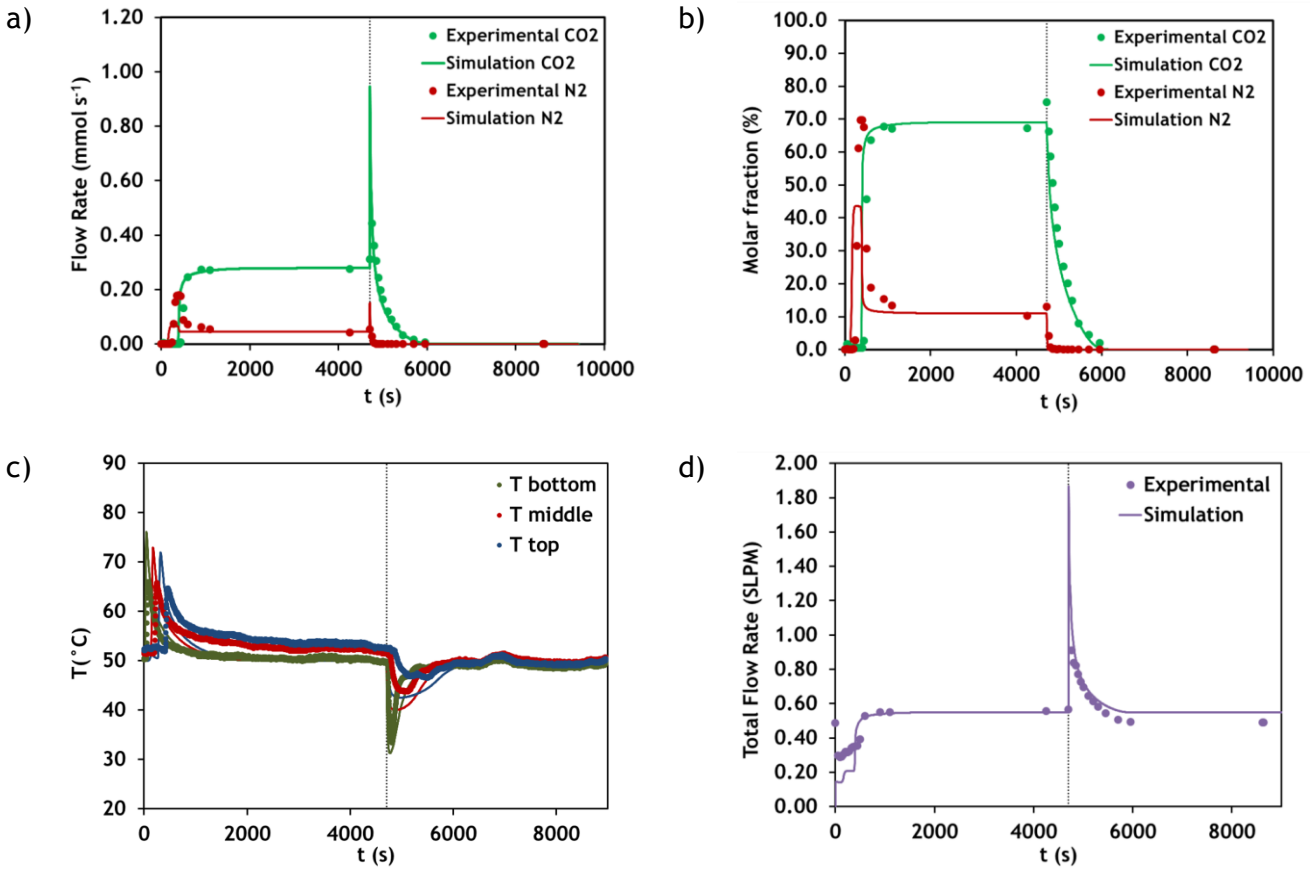

Figure A4.11 - Breakthrough results of experiment 18 (CO_2/N_2/He): molar flow rate at the column outlet (a), molar fraction at the column outlet (b), temperatures histories at 8.1 cm (bottom), 19.1 cm (middle) and 30 cm (top) (c) and total flow rate at the column outlet (d). Points correspond to experimental data and lines to simulation results. Vertical line corresponds to the beginning of desorption.

Exp.19 - CO_2/CO/He

T = 50 ºC P = 4.5 bar y_{CO2} = 0.390 y_{CO} = 0.069 F_{feed} = 0.286 mmol s^{-1}

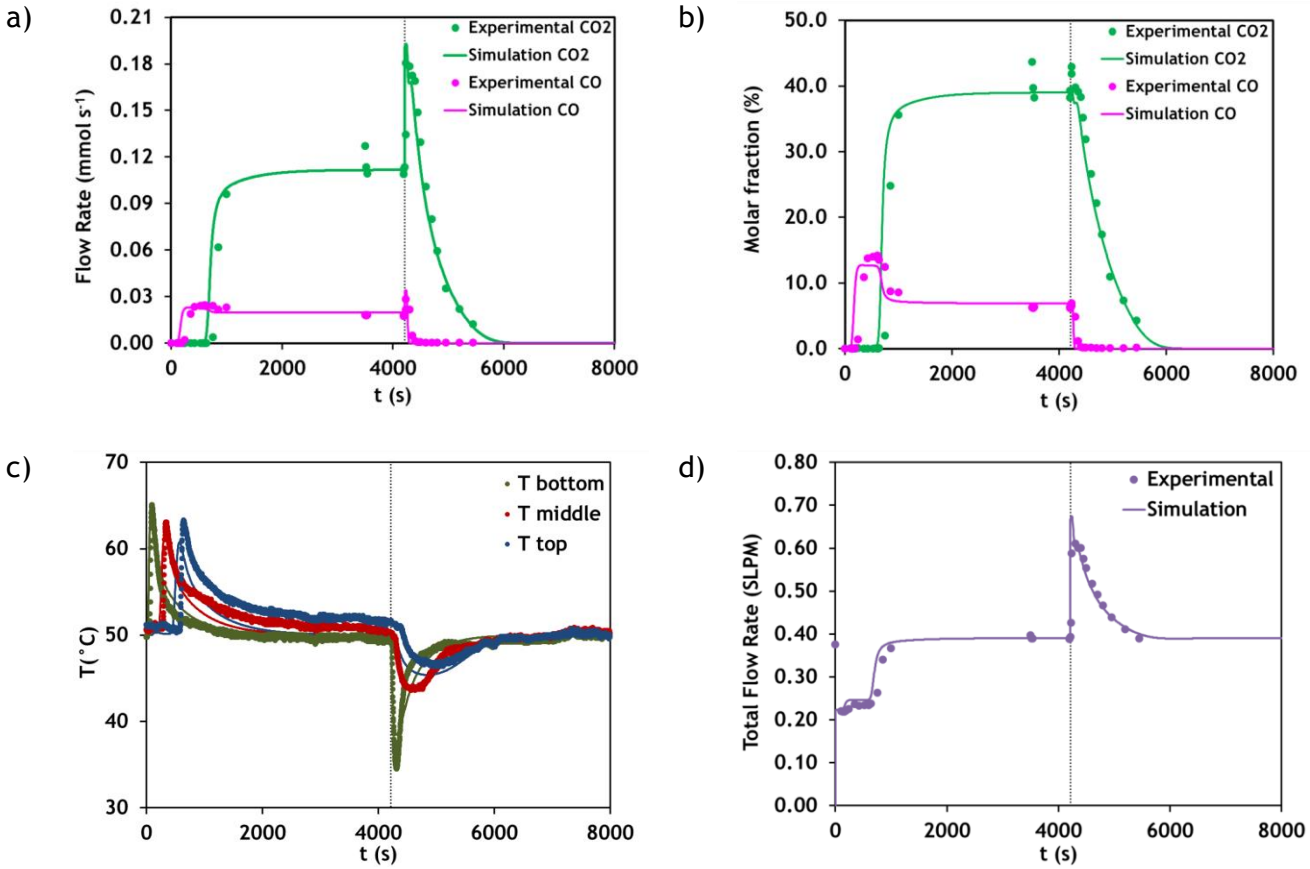

Figure A4.12 - Breakthrough results of experiment 19 (CO_2/CO/He): molar flow rate at the column outlet (a), molar fraction at the column outlet (b), temperatures histories at 8.1 cm (bottom), 19.1 cm (middle) and 30 cm (top) (c) and total flow rate at the column outlet (d). Points correspond to experimental data and lines to simulation results. Vertical line corresponds to the beginning of desorption.

Exp.20 – CO_2/CO/He

T = 50 ºC P = 4.5 bar y_{CO2} = 0.708 F_{feed} = 0.272 mmol s^{-1}

y_{CO} = 0.174

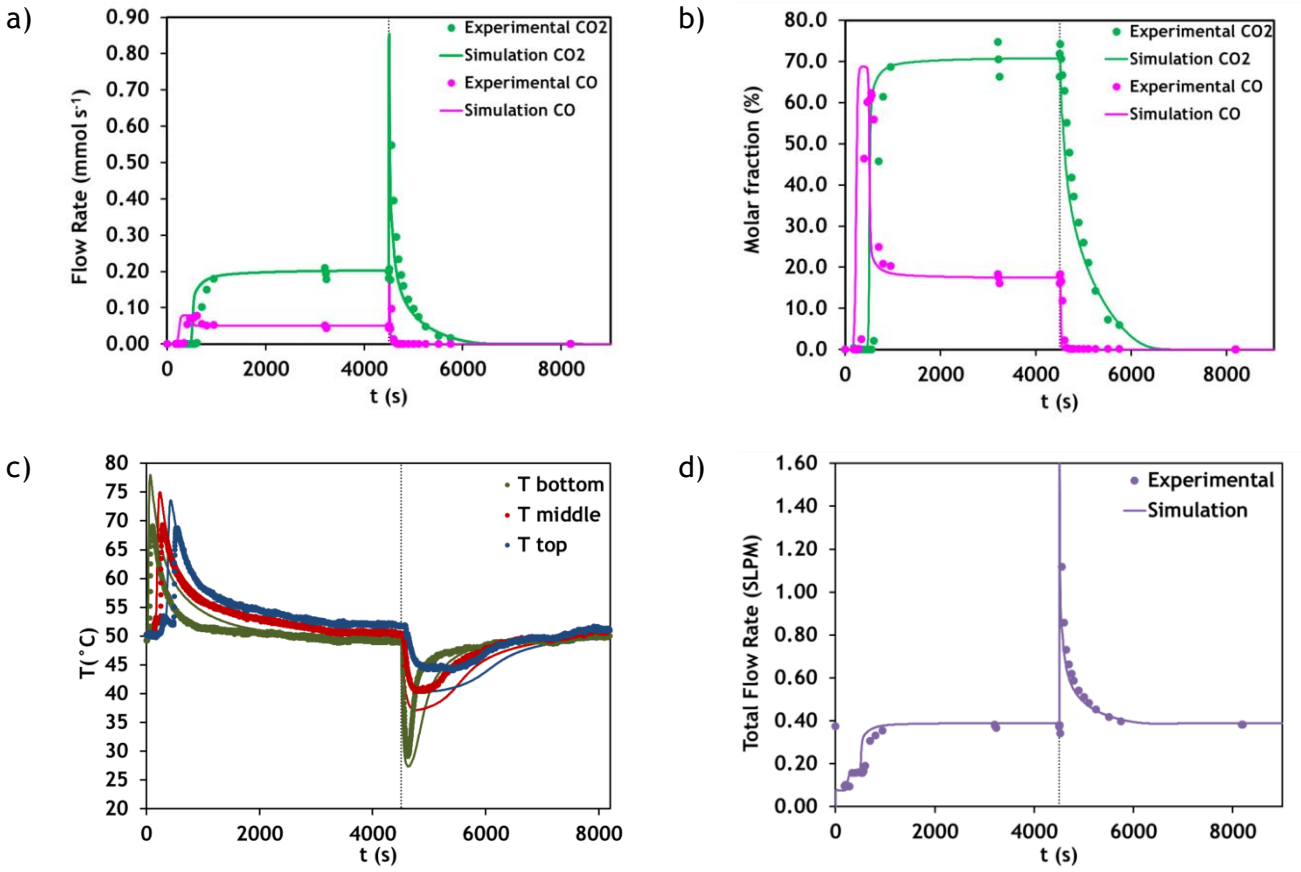

Figure A4.13 - Breakthrough results of experiment 20 (CO_2/CO/He): molar flow rate at the column outlet (a), molar fraction at the column outlet (b), temperatures histories at 8.1 cm (bottom), 19.1 cm (middle) and 30 cm (top) (c) and total flow rate at the column outlet (d). Points correspond to experimental data and lines to simulation results. Vertical line corresponds to the beginning of desorption.